NASA/TM-2003-211962

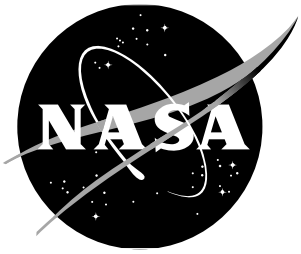

X-33 Rev-F Turbulent Aeroheating Results From Test 6817 in NASA Langley 20-Inch Mach 6 Air Tunnel and Comparisons With Computations

Brian R. Hollis, Thomas J. Horvath, and Scott A. Berry
Langley Research Center, Hampton, Virginia

June 2003

The NASA STI Program Office . . . in Profile

Since its founding, NASA has been dedicated to the advancement of aeronautics and space science. The NASA Scientific and Technical Information (STI) Program Office plays a key part in helping NASA maintain this important role.

The NASA STI Program Office is operated by Langley Research Center, the lead center for NASA's scientific and technical information. The NASA STI Program Office provides access to the NASA STI Database, the largest collection of aeronautical and space science STI in the world. The Program Office is also NASA's institutional mechanism for disseminating the results of its research and development activities. These results are published by NASA in the NASA STI Report Series, which includes the following report types:

- TECHNICAL PUBLICATION. Reports of completed research or a major significant phase of research that present the results of NASA programs and include extensive data or theoretical analysis. Includes compilations of significant scientific and technical data and information deemed to be of continuing reference value. NASA counterpart of peer-reviewed formal professional papers, but having less stringent limitations on manuscript length and extent of graphic presentations.

- TECHNICAL MEMORANDUM. Scientific and technical findings that are preliminary or of specialized interest, e.g., quick release reports, working papers, and bibliographies that contain minimal annotation. Does not contain extensive analysis.

- CONTRACTOR REPORT. Scientific and technical findings by NASA-sponsored contractors and grantees.

- CONFERENCE PUBLICATION. Collected papers from scientific and technical conferences, symposia, seminars, or other meetings sponsored or co-sponsored by NASA.

- SPECIAL PUBLICATION. Scientific, technical, or historical information from NASA programs, projects, and missions, often concerned with subjects having substantial public interest.

- TECHNICAL TRANSLATION. English-language translations of foreign scientific and technical material pertinent to NASA's mission.

Specialized services that complement the STI Program Office's diverse offerings include creating custom thesauri, building customized databases, organizing and publishing research results . . . even providing videos.

For more information about the NASA STI Program Office, see the following:

- Access the NASA STI Program Home Page at ***http://www.sti.nasa.gov***

- Email your question via the Internet to help@sti.nasa.gov

- Fax your question to the NASA STI Help Desk at (301) 621-0134

- Telephone the NASA STI Help Desk at (301) 621-0390

- Write to:
  NASA STI Help Desk
  NASA Center for AeroSpace Information
  7121 Standard Drive
  Hanover, MD 21076-1320

NASA/TM-2003-211962

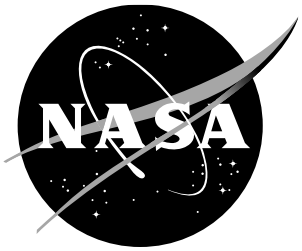

X-33 Rev-F Turbulent Aeroheating Results From Test 6817 in NASA Langley 20-Inch Mach 6 Air Tunnel and Comparisons With Computations

Brian R. Hollis, Thomas J. Horvath, and Scott A. Berry
Langley Research Center, Hampton, Virginia

National Aeronautics and
Space Administration

Langley Research Center
Hampton, Virginia 23681-2199

June 2003

Available from:

NASA Center for AeroSpace Information (CASI)
7121 Standard Drive
Hanover, MD 21076-1320
(301) 621-0390

National Technical Information Service (NTIS)
5285 Port Royal Road
Springfield, VA 22161-2171
(703) 605-6000

Contents

List of Tables

List of Figures

Abstract

Measurements and predictions of the X-33 turbulent aeroheating environment have been performed at Mach 6, perfect-gas air conditions. The purpose of this investigation was to compare measured turbulent aeroheating levels on smooth models, models with discrete trips, and models with arrays of bowed panels (which simulate bowed thermal protections system tiles) with each other and with predictions from two Navier-Stokes codes, LAURA and GASP. The wind tunnel testing was conducted at free stream Reynolds numbers based on length of 1.8 x 10^6 to 6.1 x 10^6 on 0.0132 scale X-33 models at α = 40-deg. Turbulent flow was produced by the discrete trips and by the bowed panels at all but the lowest Reynolds number, but turbulent flow on the smooth model was produced only at the highest Reynolds number. Turbulent aeroheating levels on each of the three model types were measured using global phosphor thermography and were found to agree to within the estimated uncertainty (±15%) of the experiment. Computations were performed at the wind tunnel free stream conditions using both codes. Turbulent aeroheating levels predicted using the LAURA code were generally 5%-10% lower than those from GASP, although both sets of predictions fell within the experimental accuracy of the wind tunnel data.

Introduction

The Access to Space Study conducted by NASA recommended the development of a fully Reusable Launch Vehicle (RLV)[1-4] to provide a next-generation launch capability at greatly reduced cost. This recommendation led to the RLV/X–33 technology program, an industry-led effort in which NASA was a main partner. The X–33 was to serve as a sub-scale technology demonstrator for a full-scale Single-Stage-to-Orbit (SSTO) RLV. Following a Phase I industry competition between several aerospace companies, the Lockheed-Martin lifting-body concept was selected by NASA for award of the Phase II contract to design, develop and construct an X–33 flight vehicle. The Lockheed-Martin X–33 design[5], shown in Fig. 1, is a half-scale version of a proposed RLV. The X–33 was intended to prove the feasibility of the SSTO-RLV concept through demonstration of key design and operational aspects of the vehicle; however technical and cost concerns led to the termination of the project in 2001.

As part of the X–33 industry/government partnership, NASA LaRC was tasked to provide aerodynamic performance data, surface aeroheating distributions, and boundary-layer transition correlations to Lockheed-Martin to support Phase II aerodynamic and aerothermodynamic design and development. In order to provide these data, a synergistic experimental/computational research program was conducted at NASA LaRC. Early results from the LaRC X–33 research program were presented in Refs. 6-7. In those works, data from early Phase II aeroheating wind tunnel tests were presented and compared with laminar and turbulent predictions generated using both a Navier-Stokes solver and a boundary-layer engineering code. These early results were used to formulate and support the use of an Re_θ / M_e criteria for predicting transition onset on the X–33 in flight. Subsequently, additional wind tunnel tests and computations were performed to supplement the original data base with more detailed results and to accommodate design changes to the original X–33 configuration. Key results of these studies have been presented in Refs. 8-15.

The focus of the present work was on turbulent aeroheating levels on the X-33 vehicle. Although the X-33 program has been cancelled, a considerable investment has been made in the construction of wind tunnel models, the development of computational grids and computational techniques, and the generation of an aeroheating database. Thus, the X-33 configuration, while likely no longer a candidate for development of a flight test vehicle, is still well suited for use as an object of ground-based research studies. The present study of the X-33 had three goals:

1) To extend the Reynolds number range of the ground-test database on turbulent aeroheating resulting from both natural and forced transition. Although an extensive wind tunnel database has been generated on transition criteria[8,9], relatively little quantitative experimental data on aeroheating levels have been obtained for fully-turbulent conditions. In the current work, turbulent boundary layer aeroheating data are presented for length-Reynolds numbers of 1.8×10^6 to 6.1×10^6, whereas data presented previously have been limited to 3.5×10^6 or below.

2) To investigate differences reported in previous works[8,10] in heating levels resulting from forced tripping of the boundary layer by either discrete or distributed surface roughness elements.

3) To assess the accuracy of Navier-Stokes Computational Fluid Dynamics (CFD) heating predictions by comparisons with measured turbulent aeroheating data from wind tunnel tests.

Symbols

B_{ref}	reference span (m)
H_{AW}	adiabatic enthalpy (J/kg)
H_w	wall enthalpy (J/kg)
H_0	total enthalpy (J/kg)
h	heat transfer coefficient (kg/m^2-sec), $h = q/(H_{AW} - H_w)$
h_{FR}	Fay-Riddell heating coefficient (kg/m^2-sec)
L	distance from nose to end of fuselage, exclusive of engine module
L_{ref}	reference length (m)
M	Mach number
p_∞	free stream pressure (N/m^2)
q	heat transfer rate (W/m^2)
q_{FR}	Fay-Riddell heat transfer rate (W/m^2)
R_n	nose radius (m)
Re	Reynolds number
S_{ref}	reference surface area (m^2)
T_∞	free stream temperature (K)
U_∞	free stream velocity (m/sec)
X,Y,Z	coordinate system (m)
α	angle-of-attack (deg)
ρ_∞	freestream density (kg/m^3)

Abbreviations

CCD	charge coupled device
CFD	computational fluid dynamics
GASP	General Aerodynamic Simulation Program
IHEAT	Imaging for Hypersonic Experimental Aeroheating Testing
LAURA	Langley Aerothermodynamic Upwind Relaxation Algorithm
ref	reference
RLV	reusable launch vehicle
SLA	stereo-lithographic apparatus
SSTO	single-stage to orbit
UV	ultraviolet
VGM	Volume Grid Manipulation

Vehicle Geometry

The X-33 design has a lifting-body delta planform, twin vertical tails, canted fins and body flaps, and two linear aerospike engines (Fig. 2). Configuration evolution from the Phase I design to the most recent Phase II design is discussed in Ref. 13. Computational results presented in this paper are based on the F-Loft, Rev-F configuration (Lockheed designation 604B002F), which has a length of 19.3 m (63.2 ft.) and a maximum span across the canted fins of 23.2 m (76.1 ft.). The sweep of the delta planform is 70-deg, and the cant of the fins is 20-deg with a -8.58-deg incidence angle. Reference dimensions for the vehicle are listed in Table 1.

Experimental Methods

Test Facility Description

Aeroheating tests were conducted in the NASA Langley 20-Inch Mach 6 Air Tunnel (Fig. 3). This facility is a blow-down tunnel in which heated, dried, and filtered air is used as the test gas. The tunnel has a two dimensional, contoured nozzle which opens into a 20.5-in. by 20.0-in. test section. The tunnel is equipped with a bottom-mounted injection system which can transfer a model from the sheltered model box to the tunnel centerline in less than 0.5 sec. Run times of up to 15 minutes are possible in this facility, although for the aeroheating tests models are typically exposed to the flow for only a few seconds. The nominal reservoir conditions of this facility are stagnation pressures of 206.8 to 3447.4 kPa (30 to 500 psia) with stagnation temperatures of 422.2 to 555.5 K (760 ˚R to 1000 ˚R), which produce perfect-gas free stream flows with Mach numbers between 5.8 and 6.1 and Reynolds numbers of 1.64 $\times$ 10^6 to 23.3 $\times$ 10^6 m^{-1} (0.5 $\times$ 10^6 to 7.1 $\times$ 10^6 ft^{-1}). More detailed descriptions of this facility are presented in Refs. 16-17. Representative flow conditions for each of the standard 20-Inch Mach 6 Air Tunnel operating points have been computed using the GASPROPS[18] code and are listed in Table 2.

Test Matrix and Wind Tunnel Conditions

In this wind tunnel study. LaRC 20-Inch Mach 6 Air Tunnel Test 6817, data were obtained on 0.0132-scale X-33 models at α = 40-deg (with the exception of single runs at α = 20-deg and 30-deg) for Reynolds number of 1.8 $\times$ 10^6 to 6.1 $\times$10^6 based on model length. The run matrix for Test 6817 is listed in Table 3; it includes angle-of-attack, free stream Reynolds number and Mach number, and information on trip or panel size and placement for each run. Note that by standard operating procedure for the facility, the tunnel operating conditions are referred to by the free stream Reynolds number *per foot*, and this convention will be followed throughout. Additionally, a cross-index of trip size and placement vs. run number is presented in Table 4.

Thermographic Phosphor Global Heating Technique

Global surface heating distributions were obtained through the digital optical measurement method of two color, relative-intensity, phosphor thermography[19-22]. In this method (Fig. 4), ceramic wind tunnel models are coated with a phosphor compound which fluoresces in two separate regions (green and red) of the visible light spectrum. During a wind tunnel run, the phosphor-coated model is illuminated by ultraviolet (UV) light sources, and the resulting fluorescent intensity of the model is recorded and digitized through a color CCD (charge coupled device) camera. The fluorescent intensity is dependent on both the intensity of incident UV light and the local model surface temperature. The intensity dependence on the incident UV lighting is removed by taking the ratio of the green to red intensity images. Surface temperature distributions can be determined from this ratio through prior calibrations. Images are acquired before the wind tunnel run and after injection of the model to the tunnel centerline during a run. Global heat transfer distributions can then be determined from the temperature changes between the two images using one-dimensional, constant heat-transfer coefficient conduction theory.

Data Reduction and Experimental Uncertainty

One-dimensional, semi-infinite-solid heat conduction theory was used to compute surface heating distributions from the global surface temperature data acquired through phosphor thermography. A constant heat transfer coefficient is assumed in this theory, and empirical corrections are made to account for changes in model substrate thermal properties with temperature. Phosphor images were acquired shortly after injection of the model to the tunnel centerline, which requires less than one second. Results are presented in terms of a heat transfer coefficient ratio, h/h_{FR}, where h_{FR} is the theoretical heating computed using the Fay-Riddell[23] method for a reference hemisphere of 1.21 m radius full-scale (0.01597 m or 0.629-in. model scale) with a surface temperature of 300 K.

Heating data were extracted from the global images along the centerlines of the models using the IHEAT (Imaging for Hypersonic Experimental Aeroheating Testing) code[22], which is part of the thermographic phosphor system. Image pixel data were mapped to (x,y) locations through interpolation/extrapolation from reference fiducial markings placed on the model at specified points and from identifiable features such as the nose and the end of the model. Physical locations on the model are expressed in terms of X/L and/or Y/L, where L is the distance from the nose of the model to the end of the fuselage, exclusive of the engine module.

An uncertainty analysis for heating measurements using the thermographic phosphor technique has been presented in Ref. 22. In that analysis, only uncertainties due to the calibration of the system and the data reduction method were considered. Based on that analysis, the uncertainties due to the phosphor system alone are on the order of ±10% for the operating conditions of the 20-Inch Mach 6 Air Tunnel. Additional uncertainties are introduced by the performance of the wind tunnel and quality of the test models. Based on calibration data and experience in the operation of the facility, run-to-run repeatability of tunnel conditions and flow quality are assumed to produce uncertainties on the order of ±5%. Quality assurance analysis of ceramic model aerolines suggests that model fidelity can introduce uncertainties of up to ±5% in heating data.

In certain regions of a model, additional uncertainties are produced due to its geometry. Three-dimensional conduction effects occur in regions of high curvature such as wing leading edges and introduce errors into the one-dimensional data reduction process. Photo-optical distortion causes difficulty in the translation of image pixel data to a physical location on a model (image registration). This type of error is produced by high surface curvature or by features with a large depth relative to the focal length of the camera, such as a fin which is canted out of the camera image plane. Three-dimensional conduction effects can be limited somewhat by taking data as soon as possible after model injection in order to minimize surface temperature gradients built-up in the model by heating. Optical effects can be reduced through the use of fiducial markings on the model at verified geometric positions. While the magnitude of the errors introduced by these phenomena is difficult to assess and is highly dependent on the individual model geometry, a worst-case conservative uncertainty estimate of ±15% could be applied for each of them based on previous experience. Taken together with the error sources previously noted, and computing the square-root of the sum of the squares, a worst-case uncertainty of up to ±25% could be estimated for a feature such as the leading edge of a wing or fin canted out of the image plane. However, in the present study, only data on the windward fuselage are considered, and on that part of the vehicle three-dimensional conduction effects are minimal and the translation of pixel data to physical location is more accurate due to the relatively flat surface. Therefore, the

image registration error and three-dimensional conduction errors are set to smaller values of ±7.5% and ±2.5%, respectively. Taken together with the uncertainties due to the phosphor system (±10%), wind tunnel conditions (±5%) and model fidelity (±5%), the square-root of the sum of the squares of these uncertainties gives an overall uncertainty estimate of ±15%.

Wind Tunnel Model Description

Cast ceramic models (Fig. 5) are used for aeroheating testing with the thermographic phosphor system. The fabrication process for a ceramic model begins with the production of a rapid-prototype, resin model. The resin model is built in a stereolithographic apparatus (SLA) from a CAD data file. A multiple-piece injection mold (from which the resin model can easily be removed) is then built around the resin model. The resin model is then removed and wax is injected into the mold to form a wax pattern. Next, a new two-piece shell mold is built around the wax pattern, and then the wax is burned out of the shell mold. A silica ceramic model is then slip-cast in the shell mold. Then, the ceramic model is removed from the shell mold, dried and sintered. The finished ceramic model is then back-filled with a hydraulically setting magnesia ceramic for strength and support. Finally, the ceramic model is coated with a mixture of phosphors which luminesce under ultraviolet lighting.

The model scale for the aeroheating tests was 0.0132, which produced a 0.254 m (10.0-in.) model length measured from the model nose to the end of the engine module. Models were produced with both a smooth fuselage and with a pattern of raised elements (Fig. 6) which simulated TPS tiles that have been raised or bowed due to aerodynamic heating of the vehicle during flight. For the current test, only bowed-panel models with a panel height of 0.006-in. (0.152 mm) were fabricated, although models with panel heights of 0.002-in. (0.0508 mm) to 0.008-in. (0.2032 mm) were built and tested in previous studies. Models tested during this study included both newly-fabricated models and models which had been tested in previous studies. These original models had suffered some wear (broken fins, pitted surfaces from particle impacts, etc) from previous testing which may have affected the location of boundary layer transition.

The pattern of bowed panels covered approximately the first one-third of the model, and constituted *distributed* roughness sources. In contrast, *discrete* roughness sources were created by applying individual squares of polyimde tape to different locations on the body (Fig. 7). The heights of these discrete trips were varied from 0.0025-in. (0.0635 mm) to 0.0065-in. (0.1651 mm), and from 1 to 9 of these trips were placed across the body at a given X/L location. In the current study, discrete trips were placed only at X/L locations of $0.10, 0.20$ or 0.33, while in other studies[9] a wider ranges of placement locations were studied.

Computational Methods

Numerical Algorithms

Two Navier-Stokes codes, GASP (General Aerodynamic Simulation Program) and LAURA (Langley Aerothermodynamic Upwind Relaxation Algorithm), were employed in this work to predict the aeroheating characteristics of the X-33 vehicle. Perfect-gas laminar and turbulent computations were performed at wind-tunnel test conditions using both codes. The turbulent computations were performed using the algebraic Baldwin-Lomax turbulence model.

The GASP[24] code is a three-dimensional, finite-volume Navier-Stokes solver which incorporates numerous flux formulations, thermochemical models, turbulence models, and time-integration methods. The Jacobi scheme was used for time-integration. As detailed in Ref. 12, a third-order, upwind biased, min-mod limited scheme, which consisted of a Roe[25] flux formulation in the body-normal direction and a Van Leer[26] formulation in the other two directions, was employed to represent the inviscid fluxes. Full viscous terms were retained for all three directions and modeled with second-order central differences.

The LAURA[27,28] code is a three-dimensional solver with inviscid, thin-layer, and full Navier Stokes formulations. The code includes perfect-gas, equilibrium, and non-equilibrium thermodynamic models. Time integration is a carried out through a point-relaxation scheme. Roe averaging with Hartens' entropy fix[29] and Yee's Symmetric Total Variation Diminishing limiter[30] is used for inviscid fluxes and a second-order scheme is employed for viscous fluxes. In this work, the thin-layer formulation with the perfect-gas air model was used. The thin-layer mode has been shown (e.g. Ref. 31) to produced accurate results for attached flows with a considerable savings in computational requirements.

Free Stream and Boundary Conditions

Free stream conditions for the computations were set to the operating conditions of the NASA LaRC

20-Inch Mach 6 Air Tunnel. These conditions are listed in Table 2. Note that Reynolds numbers are listed in English units in addition to metric as these units are commonly used to refer to the operating points of the tunnels. A uniform, ambient 300 K wall temperature boundary condition was imposed for all computations. The use of a constant wall temperature was valid because the experimental data were acquired before the surface temperature rise on the model had a significant effect on the heating distribution, and the heating data were compared in terms of the non-dimensional variable h/h_{FR}.

Turbulence Modeling

Turbulent aeroheating computations were performed using a Baldwin-Lomax turbulence model[32] modified for compressible flow. This turbulence model is a standard part of the LAURA code, but modifications had to made to the GASP code to convert its subsonic, incompressible formulation to the compressible formulation.

The Baldwin-Lomax model is an algebraic formulation which consists of a two-layer representation of the eddy viscosity. The inner-layer viscosity is given by:

$$\mu_{t,i} = \rho l_{mix}^2 |\omega| \tag{1}$$

The thin-shear layer approximation for vorticity is used:

$$|\omega| = \sqrt{\left(\frac{dw}{dn}\right)^2 + \left(\frac{du}{dn}\right)^2} \tag{2}$$

and the mixing length l_{mix} is given by:

$$l_{mix} = K_v n D \tag{3}$$

where $K_v = 0.4$ is the von Karman constant. The damping factor D is given by:

$$D = 1 - \exp\left(\frac{n^+}{A^+}\right) \tag{4}$$

A^+ has a constant value of 26, and the normal coordinate parameter, n^+, is given by:

$$n^+ = \frac{n\sqrt{\rho_w \tau_w}}{\mu_w} \tag{5}$$

where

$$\tau_w = \mu_w |\omega_w| \tag{6}$$

The outer layer viscosity is given by:

$$\mu_{t,0} = 0.0168 \rho C_{cp} F_{max} n_{max} F_{KLEB} \tag{7}$$

where $C_{cp} = 1.6$, n_{max} is the location of the maximum value F_{max} of the vorticity function F:

$$F = n|\omega|D \tag{8}$$

and F_{KLEB} is Klebanoff's intermittency factor:

$$F_{KLEB} = \left[1 + 5.5\left(\frac{C_{KLEB} n}{n_{max}}\right)^6\right]^{-1} \tag{9}$$

with the constant $C_{KLEB} = 0.3$

As detailed in Ref. 33 the Baldwin-Lomax model can be modified for compressible, hypersonic flows through the use of local, instead of wall values in Eq. 5, to give:

$$(n^+)_{comp} = \frac{n\sqrt{\rho \tau_w}}{\mu} \tag{10}$$

and the constant A^+ in Eq. 4 is replaced with the expression:

$$(A^+)_{comp} = 26\left(\left|\frac{\tau_w}{\tau}\right|\right)^{0.5} \tag{11}$$

with the local shear stress given by:

$$\tau = (\mu + \mu_t)|\omega| \tag{12}$$

After implementing these modifications to the GASP code, they were checked by performing turbulent computations for one of the test cases used in Ref. 33, a 9-deg cone blunt cone at hypersonic speeds (Ref. 34). The aeroheating predictions were in very close agreement with the experimental data, as shown in Fig. 8. LAURA computations with the compressible Baldwin-Lomax model have also been shown to compare well to similar experimental data in Ref. 33. However, both the GASP and LAURA comparisons with experimental data are for relatively simple, axi-symmetric geometries. As stated in the Introduction, one of the goals of this study was to compare GASP and LAURA predictions with the current heating data set, which was produced by the more complex three-dimensional flow around the X-33 vehicle. These comparisons will be presented in a later section.

Grid Generation, Resolution, and Adaptation

A single-block grid which excluded the engines and wake was generated[35] for the X-33 computations. Grid-scale was 0.0132, which matched that of the wind tunnel models. The resolution of the grid was 127 streamwise points × 181 circumferential points × 33, 65, or 129 body-normal points. During a computation, the grid was adapted to align the outer boundary of the grid with the bow shock and to cluster points in the wall boundary layer. Typically, the outer boundary was adjusted so that the shock was at approximately 80% of the normal distance from the wall to the outer grid boundary and the wall cell Reynolds numbers were in the range of 1 to 10

Grid adaptation was performed using the scheme detailed in Ref. 28. This scheme is internal to the LAURA code, but a separate external code had to be developed to post-process GASP solution files for grid adaptation using this method. Solution files were output from GASP at regular intervals, adapted, and then read back into GASP, and iteration toward a final solution was continued. Because of the time required to export, post-process, and re-import solution data, the number of grid adaptations in a GASP solution was usually less than for a LAURA solution. As a result, grids in LAURA solutions were generally smoother, and thus solution convergence was more rapid. When the more limited number of grid adaptations in the GASP solutions did not produce a suitably smooth grid, the VGM (Volume Grid Manipulation) code (Ref. 36) was used to provide additional smoothing.

Because of the different grid adaptation procedures followed with GASP and LAURA, grid adaptation must be considered as one of the variables in the comparison of results between the two codes. Although code-to-code comparisons often are performed on a one-to-one basis (i.e. identical grids), it was decided that since grid adaption is internal to the LAURA code, and thus an intrinsic contributor to the final solution, a more realistic comparison would be obtained using the different grids which were produced by the two codes.

In the previous study (Ref. 10) a 127 × 181 × 65-point grid was used to perform laminar, perfect-gas computations with the GASP code. A grid-convergence study demonstrated that for this resolution, the grid-convergence error was approximately 2-3% over most the vehicle for laminar computations. LAURA results would be expected to be the same or better, given the better grid adaption capability in that code.

For the current turbulent aeroheating study, the normal grid resolution was varied from 33 to 129 points. Results for GASP computations were performed for the $Re_\infty = 7.3 \times 10^7$/ft case with 33, 65, and 129 normal points are shown in Fig. 9. Centerline heating levels dropped by approximately 10% from the 33-point grid to the 65-point grid, and dropped by approximately 5% from the 65-point grid to the 129-point grid. Based on these results, all further GASP computations were performed on 129-point grids, and the grid convergence error for the GASP computations was estimated as 5%. A smaller grid convergence error would have been desirable, but further grid resolution increases were impractical from the standpoint of computational resources. Results for LAURA computations at the same condition are shown in Fig. 10. LAURA heating levels dropped by only 2% (except near the nose) between the 33-point and 65-point grids; therefore further grid resolution increases were not deemed necessary and all LAURA computations were performed on 65-point grids.

The difference in grid resolution requirements for GASP and LAURA solutions was attributed to two possible factors: grid quality and algorithm accuracy. As mentioned earlier in this section, LAURA solutions were computed with a greater number of grid adaptations than GASP solutions, and this fact probably contributed to the final quality of the converged solution. In regard to the accuracy of the algorithm, it was shown (after these GASP computations had been completed) in Ref. 37 that the "minmod" limiter in the version of GASP employed in this study (v 3.2.3) contains a factor that increases the stability of the computation at the cost of increased numerical dissipation and for laminar computations can produce higher heating levels than would normally be expected. While for turbulent computations the effects of this increased dissipation are small relative to the turbulent viscosity, a slight increase in computed heating levels might still be expected.

Analysis of Experimental Data

Thermographic Phosphor Heating Images

Windward surface aeroheating images were obtained during each run using the thermographic phosphor system. For reference, the images are presented in the Appendix (Figs. A.1 - A.52) in the order listed in the run matrix (Table 3). However, analysis and discussion in this report will focus mainly on the quantitative data extracted from the images, i.e. the centerline distributions. It should be noted that the ceramic fins proved to

be very delicate and several were broken during the course of this test, as can be seen in these images.

Comparison of Original and New Smooth Model Data

As stated previously, both new models and models fabricated for use in previous tests were used in this study. A comparison of laminar heating data obtained with the new and original smooth models in the current test is made with data from the original models obtained during a previous test, Test 6763 (Ref. 13) is presented in Fig. 11. As can be seen, the centerline heating data compared to well within the experimental uncertainty of ±15% over most of the vehicle.

A comparison of turbulent heating levels measured on the original model with a 0.0025-in. centerline trip in both the current test and in a previous test, Test 6763, is presented in Fig. 12. These two data sets differed by approximately 13%-16%, which is at the limit of the estimated experimental uncertainty. In Fig. 13, heating levels due to a 0.0050-in. trip measured on the new smooth model in the current test and on the original smooth model in Test 6763 are shown. For this case, the differences between the two data sets increased to approximately 30%, which was clearly not an acceptable comparison.

At this point, the differences in the heating levels between the current Test 6817 data and the older Test 6763 data shown in Figs. 12 and 13 prompted a review of the test methodology, model fabrication process, data reduction, etc. It was determined that at approximately one-third of the way through Test 6763 (after Run 086), a hardware component in the thermographic phosphor system was replaced due to failure, but the calibration data input for the new hardware were incorrect. This calibration error affected all subsequent tests in which discrete-trip heating measurements were made, while smooth and bowed-panel heating tests were conducted either before this error or in later tests after which the correct calibration data were input. The effects of this calibration error increased with temperature; thus, turbulent heating levels due to discrete trips were significantly under-estimated, but the error in the lower, laminar heating levels was small.

Re-reduction of the Test 6763 data with the correct calibration data led to a much closer comparison with the new data. As shown in Fig. 14, the re-reduced data on the original smooth model with 0.005-in. trips were within approximately ±5% of the new smooth model data over most of the model. The data without trips shown in Fig. 11 were obtained prior to the hardware change, and thus did not need to be re-reduced.

The calibration error made during Test 6763 affected several additional X-33 tests. These tests were numbered 6769, 6770 and 6777. Data from these tests have been reported in Refs. 8, 10, and 13. In Ref. 8, the data were used to formulate boundary layer transition criteria. These correlations are still valid, as they did not rely on the quantitative heating levels. In Ref. 10, comparisons were made with turbulent Navier-Stokes computations, and it was noted that the discrete roughness data (from Test 6763) did not compare well to either the computations or distributed roughness data (which will be discussed subsequently). It was theorized that the discrete roughness elements did not produce fully-developed turbulent flow, a theory that would appear to be invalid in light of the calibration error found in the reduction of those data. However, as will be shown in subsequent sections, there may still be some small differences in turbulent heating levels resulting from trips or panels or different heights. Finally, quantitative heating levels were also presented in Ref. 13. Based on the current analysis, these reported heating levels were approximately 10% to 20% lower than they should have been on the models with discrete trips

In regard to the calibration error discovered in the older data sets, it is important to note that the main purpose of the prior X-33 experimental aeroheating research was to determine boundary layer transition criteria, while measurement of heating levels was a secondary goal. Although this calibration error led to incorrect measurements of heating levels, it did not affect the character of the data - i.e. the measured location of transition onset or the growth of the area covered by the turbulent wedge downstream of transition. The transition criteria reported in Ref. 8 thus remain valid

Reynolds Number Effects on Heating Levels on Smooth Models

The effect of the free stream Reynolds number on the measured smooth-model heating distributions was investigated by testing across the range of tunnel Reynolds numbers (Re_∞ = 2.2 × 10^6/ft to 7.3 × 10^6/ft). The phosphor images and centerline distributions extracted from the images for each run are presented in Fig. 15. From the plotted data and images, it appears that transition began on and around the centerline at the aft end of the model for Re_∞ = 3.0 × 10^6/ft, and progressed both forward and outward from the centerline with increasing Reynolds number. However, the distributions did not reach a maxima and then begin decreasing along the centerline, which (by analogy with turbulent flat plate flow) would be indicative of fully-developed turbulent flow, except at the Re_∞ = 7.3 ×

10^6/ft condition. Transitional/turbulent flow was also noted on the fins and on the chines and body flaps at higher numbers, although the transition on the chines appeared to emanate from surface imperfections, at least at the lower Reynolds numbers.

Reynolds Number Effects on Heating Levels on Smooth Model with Trips

In Fig. 16, images and centerline distributions are shown for the smooth model with a single 0.0025-in. trip on the centerline of the model at X/L = 0.20. The trip had no effect at $Re_\infty = 2.2 \times 10^6$/ft. At $Re_\infty = 3.0 \times 10^6$/ft, the trip produced a long boundary layer transition which began downstream of the trip and continued to the end of the body. For $Re_\infty > 3.0 \times 10^6$/ft, boundary layer transition occurred immediately behind the trip and heating levels rose rapidly over the next 0.1 to 0.2 X/L. However, this rapid rise was not assumed to be equated with the completion of transition to fully turbulent flow, as the heating levels continued to gradually increase along the rest of the body.

In Fig. 17, images and centerline distributions are shown for the smooth model with an array of nine 0.0065-in. trips across the fuselage at $X/L = 0.20$. This array of trips produced a transition front across the entire fuselage. Transition occurred downstream of the trips for the lowest Reynolds number of 2.2×10^6/ft and occurred immediately after the trips at all higher Reynolds numbers. For all Reynolds numbers, the heating levels reached a maximum somewhere downstream of transition and then began to decrease, which was taken as evidence of fully-developed turbulent flow.

By comparing data in Figs. 16 and 17 for a given Reynolds number, it can be seen that the heating levels produced downstream of the 0.0065-in. trips were substantially higher than those downstream of the 0.0025-in. trips. Although these data were obtained on different models, the laminar data (both at low Reynolds numbers and upstream of the trips) compared well between the two models, so the differences did not appear to be due to a defect in either of the models or to any errors in the test procedure. Rather, it was concluded that the 0.0025-in. trip did not create a sufficient disturbance to cause the boundary layer to reach a fully turbulent state.

Additional data on the effects of trip height on the state of the boundary layer are presented in Fig. 18, In this figure, heating data at $Re_\infty = 4.2 \times 10^6$/ft for trip heights of 0.0025-in. to 0.0065-in. on the new model and for a 0.0025-in. trip on the original model are plotted, and data from a 0.006-in. bowed panel height model are also plotted for comparison. The 0.0065-in, 0.0050-in, and 0.0035-in trips were found to produce transition at the $X/L = 0.20$ trip location followed by a rapid rise in heating levels to a maximum at around X/L=0.40 and then a slow decrease in heating, which was assumed to correspond to fully-developed turbulent flow. Heating levels for all three of these cases agreed to well within the experimental uncertainty. In contrast, on both the original and new models with 0.0025-in. trips, transition did not occur until approximately $X/L = 0.30$ and the heating levels downstream of transition were significantly lower than for the other trip heights; furthermore heating levels did not reach a maximum on the body. It thus appeared that for these conditions, the trip height required to produce fully turbulent flow was between 0.0025-in and 0.0035-in.

Reynolds Number Effects on Heating Levels on Bowed Panel Models

Phosphor images and plotted centerline distributions obtained from the bowed panel models for the range of test Reynolds numbers are presented in Fig. 19 for the original bowed panel model and in Fig. 20 for the new bowed panel model. On both models, transition was first noted downstream of the panels at $Re_\infty = 3.0 \times 10^6$/ft, and fully developed turbulent flow was noted at $Re_\infty = 4.2 \times 10^6$/ft. As with the discrete trip models, fully turbulent flow was assumed to have been produced when the heating levels reached a maximum on the body after the transition location and then began to decline further downstream. Although there were some differences in the location where transition began on the two models (probably due to differences in model surface quality) the heating levels downstream of transition in the fully-developed turbulent flow region generally compared to within the experimental uncertainty. A comparison of data from the current test on both new and original models to data from a previous test (test number 6786) at $Re_\infty = 4.2 \times 10^6$/ft is presented in Fig. 21. Test 6786 was not affected by the hardware calibration error discussed in the previous section, and all three data sets were found to compare to within the experimental uncertainty.

The bowed panel models were also tested with single 0.0035-in. and 0.0065-in trips at $X/L = 0.20$. Results are shown in Figs. 22 and 23, respectively. For cases in which the bowed panels alone had already been shown to produce turbulent flow ($Re_\infty > 3 \times 10^6$/ft), the trips caused transition to occur earlier, but did not appear to affect the heating levels in the turbulent region after transition. The 0.0035-in trip did not have any

effect at lower Reynolds numbers, but the 0.0065-in trip produced transitional/turbulent flow for all Reynolds numbers.

Comparison of Turbulent Heating Levels Produced by Trips and Bowed Panels

Images and centerline heating distributions from the smooth models, the smooth models with various trip sizes and locations, and the bowed panel models both with and without trips are presented for each test Reynolds number in Figs. 24-30.

At the lowest Reynolds number of $Re_\infty = 1.1 \times 10^6$/ft, data are shown for the bowed panel model and for the bowed panel model with either a 0.0035-in. or 0.0065-in. trip at $X/L = 0.20$ in Fig. 24. Neither the bowed panels alone nor the 0.0035-in. trip on the bowed panels appeared to affect the boundary layer at this Reynolds number. The 0.0065-in. trip on the bowed panels produced transition downstream from the trip at approximately X/L = 0.30 and the boundary layer appeared to approach fully-turbulent levels toward the end of the body.

$Re_\infty = 2.2 \times 10^6$/ft data are shown for smooth models, smooth models with 0.0025-in. and 0.0065-in trips at $X/L = 0.20$, bowed panels models, and bowed panels models with either a 0.0035-in. trip at $X/L = 0.20$ or a 0.0065-in. trip at X/L values of 0.10, 0.20 or 0.30 in Fig. 25. The boundary layer remained laminar for the smooth model and one of the bowed panels model with no trips, the smooth model with the 0.0025-in trip, and the bowed panel model with the 0.0035-in. trip. The reason for transition occurring on the second bowed panel model with no trips but not the first one is probably due to differences in surface quality on the two models. Transition occurred for all the remaining cases (smooth model with 0.0065-in trips, the other bowed panel model, and bowed panel model with a 0.0065-in. trip at various locations) at different locations. The smooth model with the 0.0065-in. trip did not appear to reach fully turbulent levels while the bowed panel models with the 0.0065-in. trips did. Peak fully-developed turbulent heating levels for the bowed panel models with the 0.0065-in. trip were approximately $h/h_{FR} = 0.45$.

Data at $Re_\infty = 3.0 \times 10^6$/ft from the smooth and bowed panels models with no trips, the smooth models with 0.0025-in. or 0.0065-in. trips at $X/L = 0.20$, and the bowed panels models with either a 0.0035-in. trip at $X/L = 0.20$ or a 0.0065-in. trip at X/L values of 0.10, 0.20 or 0.30 are shown in Fig. 26. The boundary layer remained laminar only for the smooth model with no trips and one of the two bowed panel models runs with no trips. For the smooth model with 0.0065-in. trips and the bowed panel models with 0.0065-in. trips at various locations, transition occurred immediately after the trip, and heating levels downstream of transition rose rapidly to a maximum of approximately $h/h_{FR} = 0.50$ followed by a gradual decline along the rest of the body, which was taken as evidence of fully-developed turbulent flow. This behavior can be contrasted to the other cases (smooth model with 0.0025-in trip, the bowed panel model with 0.0035-in. trip, and the second bowed panel run with no trip, where transition occurred downstream of the disturbance and heating levels rose slowly to approach the levels of the other cases only at the very end of the body.

Data for $Re_\infty = 4.2 \times 10^6$/ft from the smooth and bowed panel models with no trips, the smooth models with either 0.0025-in. or 0.0065-in. trips at $X/L = 0.20$, and the bowed panels models with a 0.0035-in. or 0.0065-in. trip at $X/L = 0.20$ are shown in Fig. 27. The boundary layer on the smooth model with no trips remained laminar until near the end of the vehicle and low heating levels were measured. For the bowed panel models with no trips, transition occurred at approximately $X/L = 0.35$ and was followed by a rapid rise to a maximum heating level of approximately $h/h_{FR} = 0.55$ followed by a gradual decline in heating levels. On the bowed panel models with either trip height and on the smooth model with the 0.0065-in. trip, transition occurred at the trip and heating levels quickly rose to the same maximum of $h/h_{FR} = 0.55$. In contrast, on the smooth model with a 0.0025-in. trip, a longer transition following the trip was noted, and heating levels continued to rise gradually along the length of the body.

Only a limited amount of data were obtained for $Re_\infty = 5.1 \times 10^6$/ft (Fig. 28). Natural transition occurred on the smooth model, although fully-developed turbulent flow was not attained before the end of the model. Fully-developed turbulent flow appear to occur on both the smooth model with 0.0065-in. trips and the bowed panel model. The bowed panel model heating was slightly lower than the heating on the smooth model with trips, but the differences were nearly within the experimental uncertainty.

Data for $Re_\infty = 5.8 \times 10^6$/ft are shown in Fig. 29. Natural transition occurred on the smooth model, although fully-developed turbulent flow was not attained before the end of the model. On the bowed panel models (both with and without trips), a short boundary layer transition was noted followed by peak heating levels of $h/h_{FR} = 0.65$ and then by a gradual decline in heating. On the smooth model with 0.0065-in. trips, a rapid tran-

sition to peak heating levels of approximately h/h_{FR} = 0.70 was followed by a decline in heating. In contrast, for the smaller 0.0025-in. trip on the smooth model, heating levels did not reach a maximum on the body. For this Reynolds number, it was thus concluded that fully-developed turbulent flow was produced for all cases except for the smooth model and the smooth model with the 0.0025-in. trip. Although peak fully developed turbulent heating levels were again slightly higher on the model with trips than on the bowed panel model the differences mostly remained within the experimental uncertainty.

Data for the highest Reynolds number of 7.3 × 10^6/ft are shown in Fig. 30 for the smooth and bowed panel models with no trips, the smooth models with 0.0025-in. or 0.0065-in. trips at X/L = 0.20 and the bowed panel model with a 0.0035-in. trip at X/L = 0.20. For all cases except the smooth model with a 0.0025-in. trip, boundary layer transition followed by a rise to peak heat levels of approximately h/h_{FR} = 0.70 to 0.75 followed by a gradual decline were noted and the flow was taken to be fully turbulent. This case is also the only one in which natural transition on a smooth model appeared to result in fully-developed turbulent flow. The trip heating levels were again slightly higher than the bowed panel heating levels

To summarize the data presented in this and previous sections, fully developed turbulent flow was produced either naturally or through discrete trips and/or bowed panels. A combination of trips and panels produced turbulent flow at Re_∞ = 1.1 × 10^6/ft and higher, bowed panels alone produced turbulent flow at Re_∞ = 3.0 × 10^6/ft and higher, trips alone produced turbulent flow at Re_∞ = 3.0 × 10^6/ft, and natural transition to fully developed turbulent flow occurred at Re_∞ = 7.3 × 10^6/ft. In general, the fully-turbulent heating levels produced by all three mechanisms agreed to within the experimental uncertainty. Previously noted large differences discrete trip and bowed panel heating data were shown to be due to calibration error. While there did still appear to be a trend of the trip heating levels being slightly higher than the bowed panel heating levels, especially at the larger Reynolds numbers, these differences were smaller than the experimental uncertainty and thus might be attributable to systemic factors such as the accuracy in casting the aerolines of the different ceramic models, the quality of the thermographic phosphor coating of the different models, etc.

Comparisons of Experimental Data with Computational Predictions

A laminar comparison is shown in Fig. 31 to demonstrate the baseline agreement between experiment and computations. Except near the nose stagnation point, predicted heating levels from the two codes agreed to within ±5% and the experimental data agreed with the predictions to within the ±15% experimental uncertainty.

Comparisons of measured and predicted centerline turbulent heating levels are shown for each of the four test Reynolds numbers in Figs. 32-35. As noted in each figure, the turbulent data were obtained from models with trips, panels, both trips and panels and from smooth models. Experimental data are shown only from the runs in which the boundary layer flow was concluded to be fully turbulent. The computations were all performed as fully turbulent from the nose of the vehicle. Although this choice did not exactly match the observed flow fields in the wind tunnel, where transition occurred at different stations along the body, measured fully turbulent heating levels were observed to decrease only slightly along the length of the body, and so the differences between measured and predicted heating levels due to transition location were expected to be small.

For all Reynolds numbers, both sets of predictions matched the fully-turbulent experimental data along the centerline to within the estimated experimental uncertainty of ±15%. However, GASP heating levels were 5%-10% higher than the LAURA levels (and up to 15% higher near the nose). As noted previously, the grid convergence error estimate for GASP was approximately 5% as compared to approximately 2% for LAURA, and additionally, a small over-prediction was expected due to the limiter function used for the GASP computations.

Summary

An experimental and computational study of turbulent aeroheating on the X-33 vehicle has been conducted at Mach 6, perfect-gas air wind tunnel conditions. Testing was conducted at α = 40-deg across a Reynolds number range of 1.1 × 10^6/ft to 7.3 × 10^6/ft with 0.0132-scale models. Turbulent flow was generated on smooth test models and on models with discrete trips or bowed panels, and heating levels were measured using global phosphor thermography. Turbulent aero-

heating predictions were performed using the Navier-Stokes solvers GASP and LAURA.

In the wind tunnel test, turbulent flow was produced by the trips and bowed panels at all but the lowest test Reynolds number, where both a trip and the bowed panels were required to produce turbulent flow, while turbulent flow was produced on the smooth models at only the highest Reynolds number.

Turbulent aeroheating levels measured on all three model types agreed to within the estimated experimental uncertainty of ±15%, although heating levels on models with trips were generally slightly higher than on models with bowed panels. Large differences noted in previous studies between discrete trip and bowed panel heating levels were found to be due to a data acquisition system calibration error. For discrete trips, fully-developed turbulent heating levels were shown to be independent of trip height for range of trips tested.

Computed turbulent heating levels agreed with each other to within 5%-10%, although GASP predictions were consistently higher than the LAURA predictions. Both sets of predictions matched the turbulent experimental data to within the estimated uncertainty for all test Reynolds numbers.

References

1. Bekey, I., Powell, R., and Austin, R., "NASA Studies Access to Space," Aerospace America, May 1994, pp. 38 43.

2. Cook, S. A., "X–33 Reusable Launch Vehicle Structural Technologies," AIAA Paper 97-10873, Nov. 1996.

3. Freeman Jr., D. C., Talay, T. A, and Austin, R. E., "Reusable Launch Vehicle Technology Program," AIAA Paper IAF 96-V.4.01, Oct., 1996.

4. Powell, R. W., Lockwood, M. K, and Cook, S. A., "The Road from the NASA Access-to-Space Study to a Reusable Launch Vehicle," AIAA Paper IAF-98-V.4.02, Sept. 1998.

5. Baumgartner, R. I., and Elvin, J. D., "Lifting Body - An Innovative RLV Concept," AIAA Paper 95-3531, Sept. 1995.

6. Thompson, R. A., Hamilton II, H. H., Berry, S. A., and Horvath, T. J., "Hypersonic Boundary Layer Transition for X–33 Phase II Vehicle," AIAA Paper 98-0867, Jan., 1998.

7. Hamilton II, H. H., Weilmuenster, K. J., Berry, S. A., and Horvath, T. J., "Computational/ Experimental Aeroheating Predictions for X–33 Phase II Vehicle," AIAA Paper 98-0869, Jan. 1998.

8. Berry, S. A., Horvath, T. J., Hollis, B. R., Thompson, R. A., Hamilton II, H. H., "X–33 Hypersonic Boundary Layer Transition," *Journal of Spacecraft and Rocket*s, Vol. 38, No. 5, Sept.-Oct. 2001, pp. 646-657.

9. Berry, S. A., Horvath, T. J., Kowalkowski, M. K., and Liechty, D. S., "X-33 (Rev-F) Aeroheating Results of Test 6770 in NASA Langley 20-Inch Mach 6 Air Tunnel," NASA TM-1999-209122, March 1999.

10. Hollis, B. R., Horvath, T. J., Berry, S. A., Hamilton, H. H. II, Thompson, R. A., and Alter, S. J., "X-33 Aeroheating Predictions and Comparisons with Experimental Data," *Journal of Spacecraft and Rocket*s, Vol. 38, No. 5, Sept.-Oct. 2001, pp. 658-669.

11. Hollis, B. R., Thompson, R. A., Murphy, K. J., Nowak, R. J., Riley, C. J., Wood, W. A., Alter, S. A., and Prabhu, R. K., "X-33 Aerodynamic Computations and Comparisons with Wind Tunnel Data," *Journal of Spacecraft and Rockets*, Vol. 38, No. 5, Sept.-Oct. 2001, pp. 684-691.

12. Hollis, B. R., Thompson, R. A., Berry, S. A., Horvath, T. J., Murphy, K. J., and Nowak, R. J., "X-33 Computational Aeroheating/Aerodynamic Predictions and Comparisons with Experimental Data," NASA TP-2003-212160, May, 2003.

13. Horvath, T. J, Berry, S. A., Hollis, B. R., Liechty, D. S., Hamilton II, H. H., Merski, N. R., "X–33 Experimental Aeroheating at Mach 6 Using Phosphor Thermography," *Journal of Spacecraft and Rockets*, Vol. 38, No. 5, Sept.-Oct. 2001, pp. 634-645.

14. Murphy, K. J., Nowak, R. J., Hollis, B. R., and Thompson, R. A., "X–33 Hypersonic Aerodynamic Characteristics," *Journal of Spacecraft and Rockets*, Vol. 38, No. 5, Sept.-Oct. 2001, pp. 670-683.

15. Thompson, R. A., "Review of X-33 Hypersonic Aerodynamic and Aerothermodynamic Development," 22nd International Congress of the Aeronautical Sciences, ICA-0323, Aug. 27 - Sept. 1, 2000.

16. Micol, J. R., "Aerothermodynamic Measurement and Prediction for Modified Orbiter at Mach 6 and 10," Journal of Spacecraft and Rockets, Vol. 32. No. 5, pp. 737-748, Sept.-Oct. 1995.

17. Micol, J. R. "Langley Aerothermodynamic Facilities Complex: Enhancements and Testing Capabilities," AIAA Paper 98-0147, Jan. 1998.

18. Hollis, B. R., "Real-Gas Flow Properties for NASA Langley Research Center Aerothermodynamic Facilities Complex Wind Tunnels," NASA CR 4755, Sept. 1996.

19. Buck, G. M., "Automated Thermal Mapping Techniques Using Chromatic Image Analysis," NASA TM 101554, April 1989.

20. Buck, G. M., "Surface Temperature/Heat Transfer Measurement Using a Quantitative Phosphor Thermography System," AIAA Paper 91-0064, Jan. 1991.

21. Merski, N. R., "A Relative-Intensity, Two-Color Phosphor Thermography System," NASA TM 104123, Sept. 1991.

22. Merski, N. R., "Global Aeroheating Wind-Tunnel Measurements Using Improved Two-Color Phosphor Thermography Methods, *Journal of Spacecraft and Rockets*, Vol. 36, No. 2, pp. 160-170, March-April 1999.

23. Fay, J. A., and Riddell, F. R., "Theory of Stagnation Point Heat Transfer in Dissociated Air," *Journal of Aeronautical Sciences*, Vol. 25, No. 2., pp. 73-85, Feb. 1958.

24. AeroSoft, "GASP Version 3, The General Aerodynamic Simulation Program, Computational Flow Analysis Software for the Scientist and Engineer, User's Manual," AeroSoft Inc., Blacksburg, VA, May 1996.

25. Roe, P. L., "Approximate Riemann Solvers, Parameter Vectors and Difference Schemes," Journal of Computational Physics, Vol. 43, No. 2, 1981, pp. 357-372.

26. Van Leer, B., "Flux Vector Splitting for the Euler Equations," Proceedings of the 8th International Conference on Numerical Methods in Fluid Dynamics, Springer Verlag, Berlin, 1981.

27. Gnoffo, P. A., "An Upwind-Biased, Point-Implicit Algorithm for Viscous, Compressible Perfect-Gas Flows," NASA TP 2953, Feb. 1990.

28. Cheatwood, F. M., and Gnoffo, P. A., "User's Manual for the Langley Aerothermodynamic Upwind Relaxation Algorithm (LAURA)," NASA TM 4674, April, 1996.

29. Harten, A., "High Resolution Schemes for Hyperbolic Conservation Laws," Journal of Computational Physics, Vol. 49, No. 3, 1983, pp. 357-393.

30. Yee, H. C., "On Symmetric and Upwind TVD Schemes," NASA TM 88325, 1990.

31. Cheatwood, F. M., Merski, N. M., Riley, C. J., and Mitchletree, R. A., "Aerothermodynamic Environment Definition for the Genesis Sample Return Capsule," AIAA Paper 2001-2889, June 2001.

32. Baldwin, B. S. and Lomax, H., "Thin Layer Approximation and Algebraic Model for Separated Turbulent Flow," AIAA Paper 78-257, Jan. 1978.

33. Cheatwood, F. M. and Thompson, R. A., "The Addition of Algebraic Turbulence Modeling to Program LAURA", NASA TM 107758, April 1993.

34. Widhopf, G. F., "Turbulent Heat-Transfer Measurements on a Blunt Cone at Angle of Attack," *AIAA Journal*, Vol. 9. No. 9, pp. 1574-1580, August 1971.

35. Alter, S. J., "Grid Generation Techniques Utilizing the Volume Grid Manipulator," AIAA Paper 98-3012, June 1998.

36. Alter, S. J., "The Volume Grid Manipulator (VGM): A Grid Reusability Tool," NASA CR-4772, April 1997.

37. Prabhu, D. K., Wright, M. J., Marvin, J. G., Brown, J. L., and Venkatapathy, E., "X-33 Aerothermal Design Environment Predictions: Verification and Validation," AIAA Paper 2000-2686, June 2000.

Table 1: Reference Dimensions for X-33 F-Loft, Rev-F Configuration

Dimension	Full-Scale	Model Scale (1.32%)
S_{ref}	149.4 m^2 (1608 ft^2)	2.60 cm^2
L_{ref}	19.3 m (63.2 ft)	25.4 cm
B_{ref}	11.2 m (36.6 ft)	14.8 cm
R_n	1.21 m (3.97 ft)	1.60 cm

Table 2: Free stream Conditions for 20-Inch Mach Air Tunnel

	M_∞	T_∞ (K)	ρ_∞ (kg/m^3)	U_∞ (m/s)	Re_∞ (1/m)	h_{FR} (kg/m^2-s)	q_{FR} (W/cm^2)
$Re_\infty = 1.1 \times 10^6$/ft	5.89	61.3	1.794×10^{-2}	925.2	3.775×10^6	0.2827	5.333
$Re_\infty = 2.2 \times 10^6$/ft	5.95	62.4	3.343×10^{-2}	942.0	7.033×10^6	0.3944	8.103
$Re_\infty = 3.0 \times 10^6$/ft	5.98	62.3	4.648×10^{-2}	944.1	9.845×10^6	0.4662	9.653
$Re_\infty = 4.2 \times 10^6$/ft	6.00	61.5	6.438×10^{-2}	941.7	1.376×10^7	0.5470	11.67
$Re_\infty = 5.1 \times 10^6$/ft	6.02	63.4	7.922×10^{-2}	958.7	1.669×10^7	0.6202	13.78
$Re_\infty = 5.8 \times 10^6$/ft	6.03	62.6	8.953×10^{-2}	953.3	1.901×10^7	0.6548	14.16
$Re_\infty = 7.3 \times 10^6$/ft	6.06	62.4	1.136×10^{-1}	955.6	2.426×10^7	0.7397	16.14

Table 3: Run Matrix for Test 6817

Run	Model #	α (deg)	Re_∞/ft (x10^6)	Panel Config.	Panel Height	Trip height (in)	Trip location (X/L)	Trip Config.	Notes
1	old bowed (RG10F3-A)	40	4.2	Extended Panel Array	0.006	NA	NA	NA	old model for comparaison to data from previous tests
2	old bowed (RG10F3-A)	40	2.2	Extended Panel Array	0.006	NA	NA	NA	old model for comparaison to data from previous tests
3	old bowed (RG10F3-A)	40	3.0	Extended Panel Array	0.006	NA	NA	NA	old model for comparaison to data from previous tests
4	old bowed (RG10F3-A)	40	1.1	Extended Panel Array	0.006	NA	NA	NA	old model for comparaison to data from previous tests
5	old bowed (RG10F3-A)	40	1.1	Extended Panel Array	0.006	0.0035	0.20	single	no effect
6	old bowed (RG10F3-A)	40	2.2	Extended Panel Array	0.006	0.0035	0.20	single	no effect
7	old bowed (RG10F3-A)	40	3.0	Extended Panel Array	0.006	0.0035	0.20	single	beginning to transition
8	old bowed (RG10F3-A)	40	4.2	Extended Panel Array	0.006	0.0035	0.20	single	transition near trip
9	old bowed (RG10F3-A)	40	5.8	Extended Panel Array	0.006	0.0035	0.20	single	transition near trip
10	old bowed (RG10F3-A)	40	7.3	Extended Panel Array	0.006	0.0035	0.20	single	transition near trip
11	old bowed (RG10F3-A)	40	5.8	Extended Panel Array	0.006	NA	NA	NA	turbulent

Table 3: Run Matrix for Test 6817

Run	Model #	α (deg)	Re_∞/ft (x10^6)	Panel Config.	Panel Height	Trip height (in)	Trip location (X/L)	Trip Config.	Notes
12	old bowed (RG10F3-A)	40	7.3	Extended Panel Array	0.006	NA	NA	NA	turbulent
13	old bowed (RG10F3-A)	40	3.0	Extended Panel Array	0.006	0.0065	0.20	single	
14	old bowed (RG10F3-A)	40	2.2	Extended Panel Array	0.006	0.0065	0.20	single	
16	old bowed (RG10F3-A)	40	1.1	Extended Panel Array	0.006	0.0065	0.20	single	
17	old bowed (RG10F3-A)	40	4.2	Extended Panel Array	0.006	0.0065	0.20	single	
18	old bowed (RG10F3-A)	40	3.0	Extended Panel Array	0.006	0.0065	0.33	single	
19	old bowed (RG10F3-A)	40	2.2	Extended Panel Array	0.006	0.0065	0.33	single	
20	old bowed (RG10F3-A)	40	3.0	Extended Panel Array	0.006	0.0065	0.10	single	
21	old bowed (RG10F3-A)	40	2.2	Extended Panel Array	0.006	0.0065	0.10	single	
23	old smooth (RF10A1-B)	40	2.2	Smooth	NA	0.0025	0.20	single	
24	old smooth (RF10A1-B)	40	3.0	Smooth	NA	0.0025	0.20	single	
25	old smooth (RF10A1-B)	40	4.2	Smooth	NA	0.0025	0.20	single	
27	old smooth (RF10A1-B)	40	5.8	Smooth	NA	0.0025	0.20	single	
28	old smooth (RF10A1-B)	40	7.3	Smooth	NA	0.0025	0.20	single	model destroyed

Table 3: Run Matrix for Test 6817

Run	Model #	α (deg)	Re_∞/ft (x10^6)	Panel Config.	Panel Height	Trip height (in)	Trip location (X/L)	Trip Config.	Notes
56	new smooth	40	4.20	Smooth	NA	NA	NA	NA	transition from nick on body flaps
57	new smooth	40	3.00	Smooth	NA	NA	NA	NA	
58	new smooth	40	2.00	Smooth	NA	NA	NA	NA	
59	new smooth	40	5.10	Smooth	NA	NA	NA	NA	transition from nick on body flaps
60	new smooth	40	2.00	Smooth	NA	0.0065	0.20	array of 5	transition from outboard trip missed chine/ body-flap
61	new smooth	40	3.00	Smooth	NA	0.0065	0.20	array of 9	added more trips to array
62	new smooth	40	4.20	Smooth	NA	0.0065	0.20	array of 9	
63	new smooth	40	5.10	Smooth	NA	0.0065	0.20	array of 9	
64	new smooth	40	5.80	Smooth	NA	0.0065	0.20	array of 9	
65	new smooth	40	7.30	Smooth	NA	0.0065	0.20	array of 9	lost right wing, some staining of coating
66	new smooth	40	5.10	Smooth	NA	0.0065	0.20	array of 9	repeat run 063
67	new smooth	30	4.20	Smooth	NA	0.0065	0.20	array of 9	
68	new smooth	20	4.20	Smooth	NA	0.0065	0.20	array of 9	
69	new smooth	40	4.20	Smooth	NA	0.0065	0.20	array of 9	repeats run 62
70	new smooth	40	4.20	Smooth	NA	0.0065	0.20	single	
71	new smooth	40	4.20	Smooth	NA	0.0035	0.20	single	
72	new smooth	40	4.20	Smooth	NA	0.0025	020	single	
73	new smooth	40	4.20	Smooth	NA	0.0035	0.20	single	repeats run 071
74	new smooth	40	4.20	Smooth	NA	0.0050	0.20	single	

Table 3: Run Matrix for Test 6817

Run	Model #	α (deg)	Re_∞/ft (x10^6)	Panel Config.	Panel Height	Trip height (in)	Trip location (X/L)	Trip Config.	Notes
75	new smooth	40	5.80	Smooth	NA	NA	NA	NA	
76	new smooth	40	7.30	Smooth	NA	NA	NA	NA	model showing bad staining after run
77	new bowed	40	4.20	Extended Panel Array	0.006	NA	NA	NA	
78	new bowed	40	3.00	Extended Panel Array	0.006	NA	NA	NA	
79	new bowed	40	2.00	Extended Panel Array	0.006	NA	NA	NA	
80	new bowed	40	5.10	Extended Panel Array	0.006	NA	NA	NA	
81	new bowed	40	5.80	Extended Panel Array	0.006	NA	NA	NA	
82	new bowed	40	7.30	Extended Panel Array	0.006	NA	NA	NA	

Table 4: Cross-Index of Run Number with Given Re_∞ and Panel/Trip Configuration

	1.1×10^6/ft	2.2×10^6/ft	3.0×10^6/ft	4.2×10^6/ft	5.1×10^6/ft	5.8×10^6/ft	7.3×10^6/ft
Smooth		58	57	56	59	75	76
Smooth + 0.0025-in. trip @ X/L=0.20		23	24	25, 72		27	28
Smooth + 0.0035-in. trip @ X/L=0.20				71, 73			
Smooth + 0.0050-in. trip @ X/L=0.20				74			
Smooth + 0.0065-in. trip @ X/L=0.20				70			
Smooth + 0.0065-in. trip array @ X/L=0.20		60	61	62, 69	63, 66	64	65
Bowed Panels	4	3, 79	2, 78	1, 77	80	11, 81	12, 82
Bowed Panel +0.0035-in. trip @ X/L=0.20	5	6	7	8		9	10
Bowed Panel +0.0065-in. trip @ X/L=0.10		21	20				
Bowed Panel +0.0065 -in. trip @ X/L=0.20		19	18				
Bowed Panel +0.0065-in. trip @ X/L=0.32	16	14	13	17			

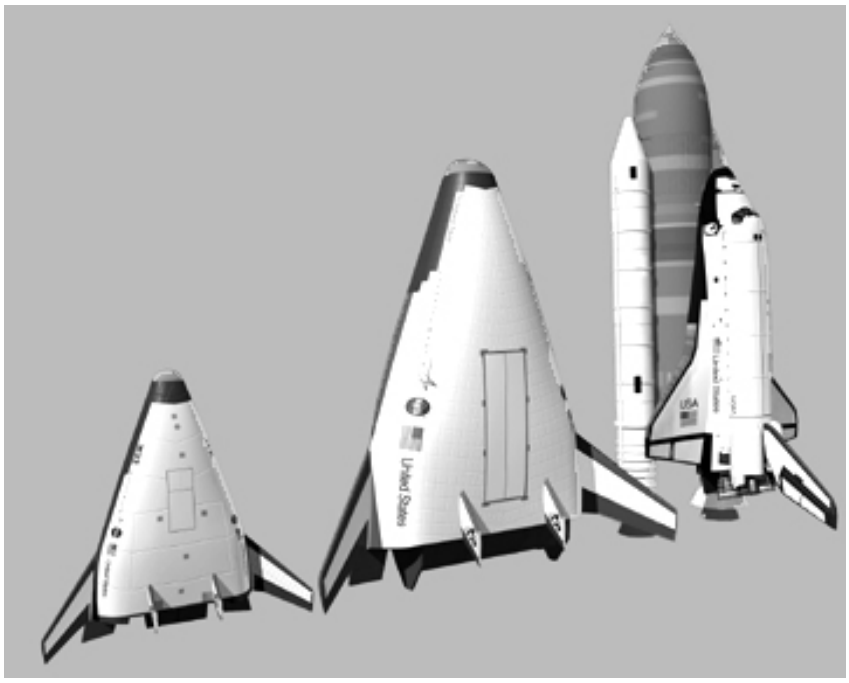

Figure 1: Comparison (from left to right) of X-33 Vehicle to RLV Concept and Space Shuttle

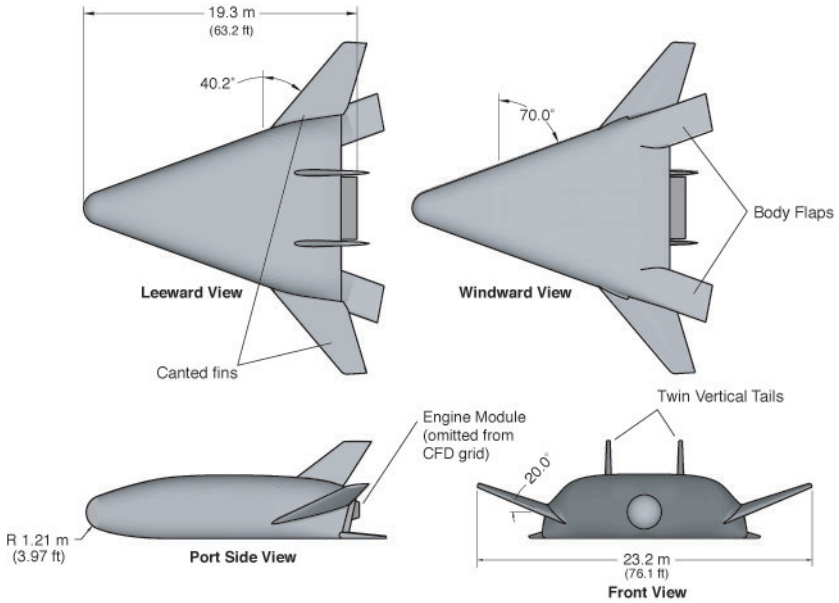

Figure 2: Sketch Showing Dimensions of X-33 F-Loft, Rev-F Configuration

Figure 3: NASA LaRC 20-Inch Mach 6 Air Tunnel

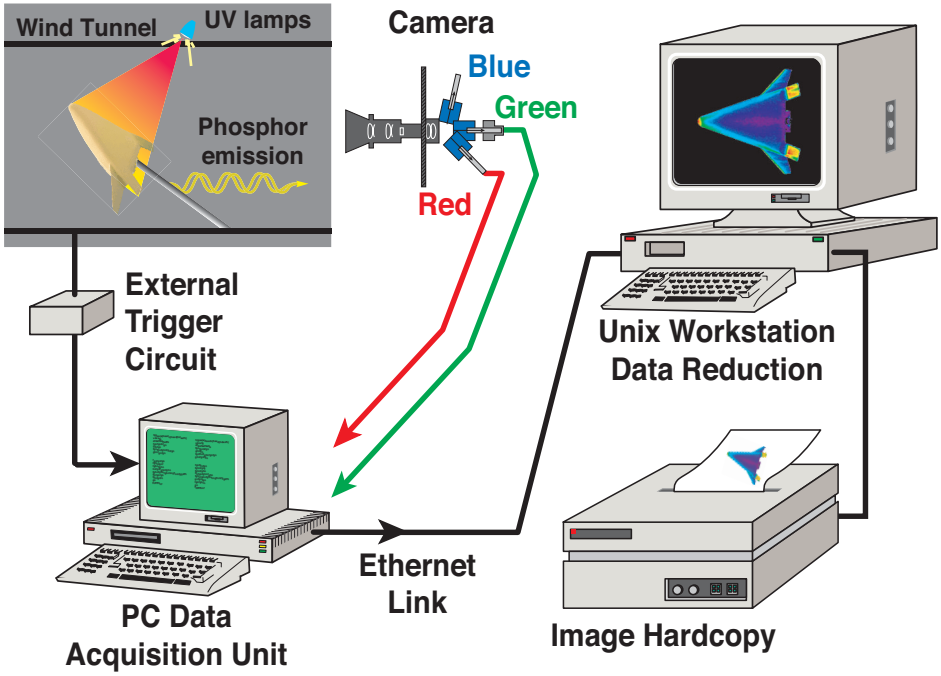

Figure 4: Schematic of Langley Two-Color Thermographic Phosphor System

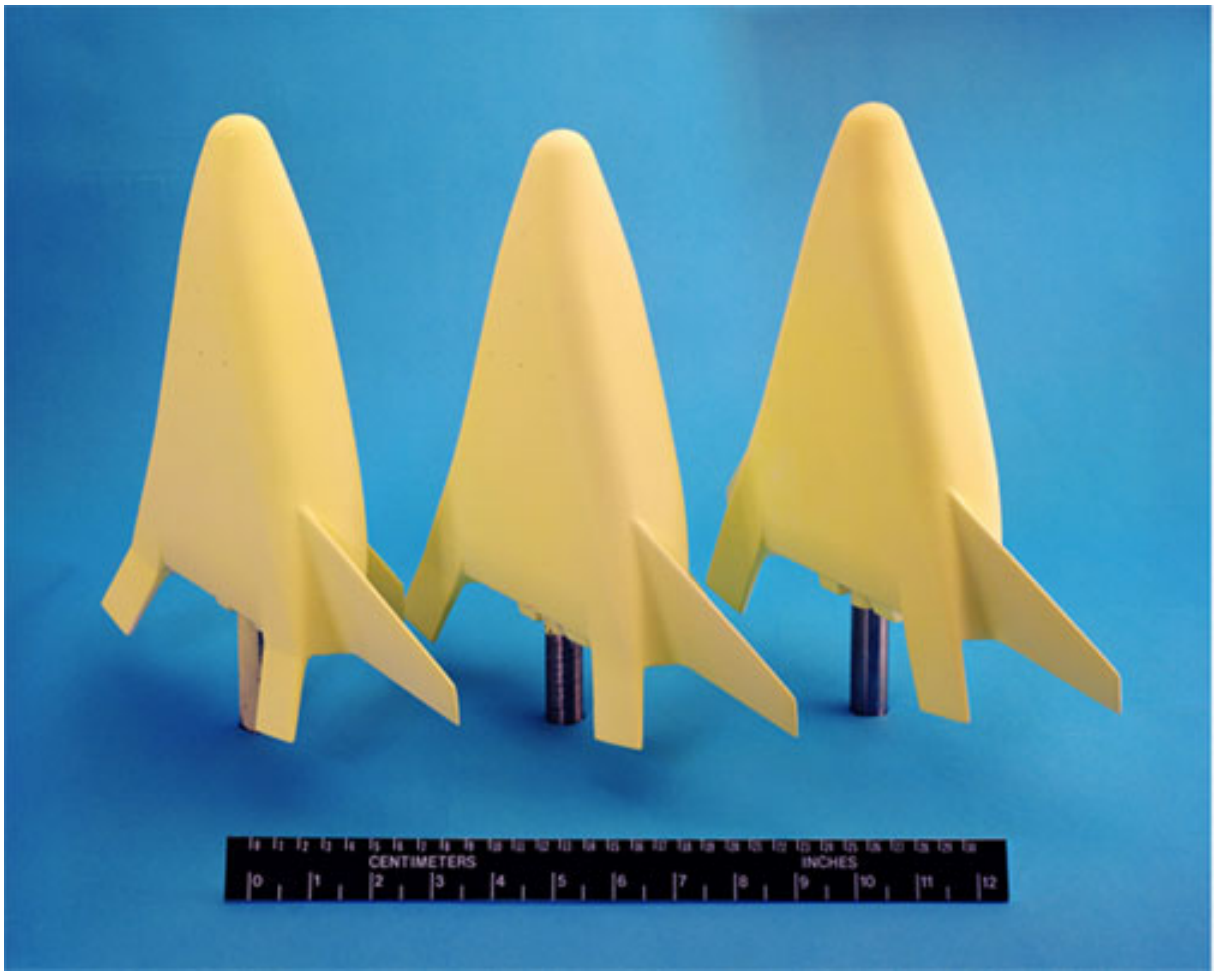

Figure 5: Phosphor-Coated Ceramic X-33 Models

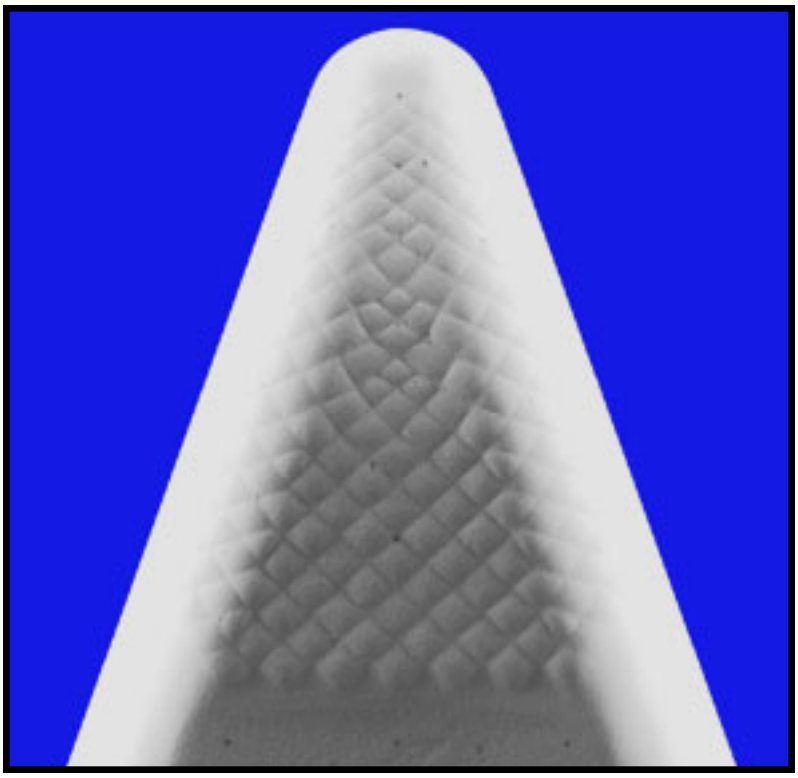

Figure 6: Close-up of X-33 Ceramic Model with Bowed Panels

Figure 7: Close-Up of Model Nose Showing 0.0065-in. Trip Array at X/L=0.20

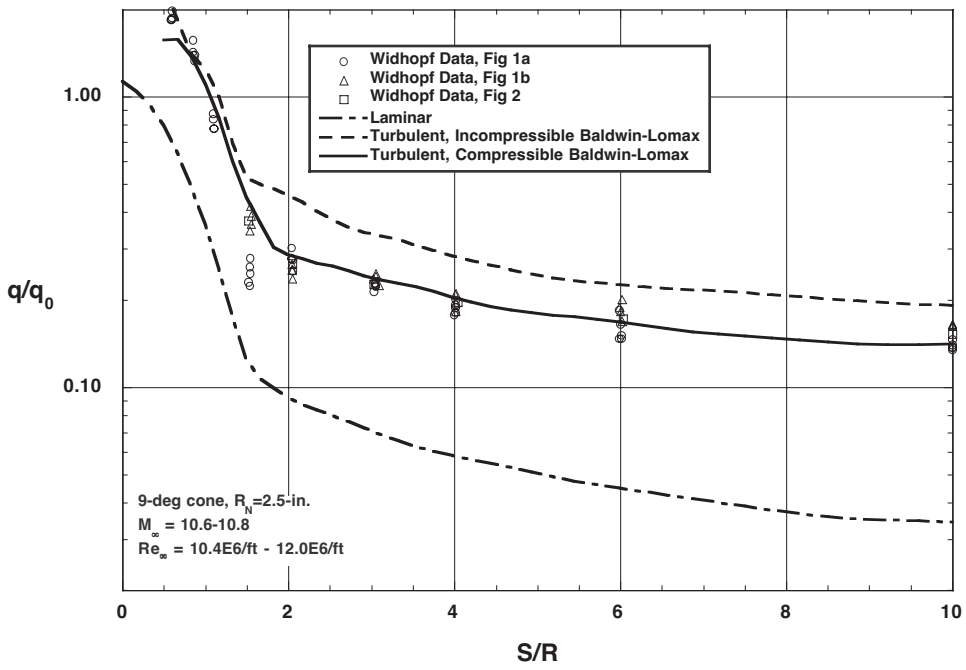

Figure 8: Comparison of GASP Computation Using Compressible Baldwin-Lomax Model with Experimental Data from Ref. 34

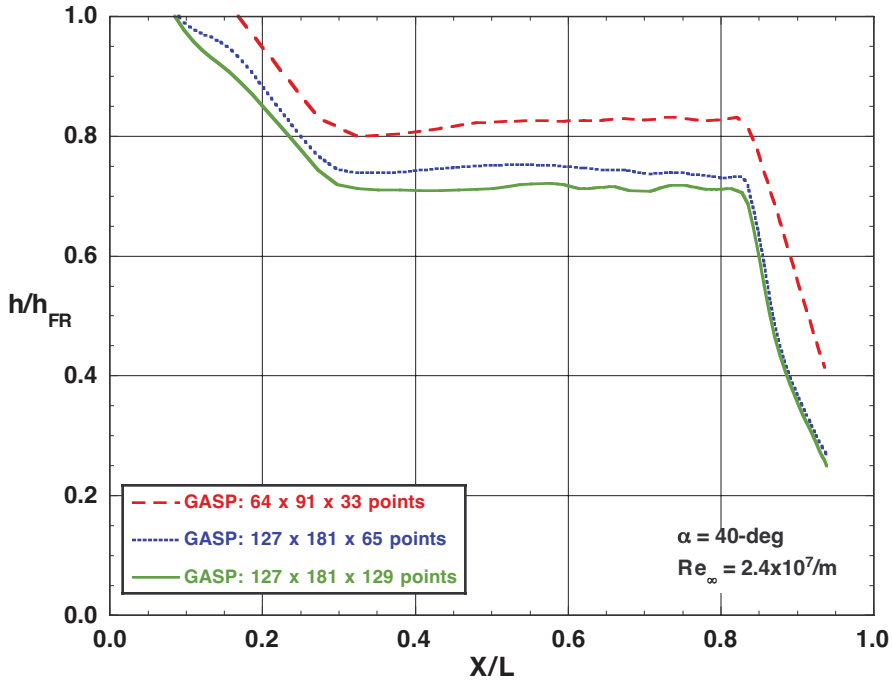

Figure 9: Turbulent Centerline Heating Levels Computed with GASP for Different Grid Resolution

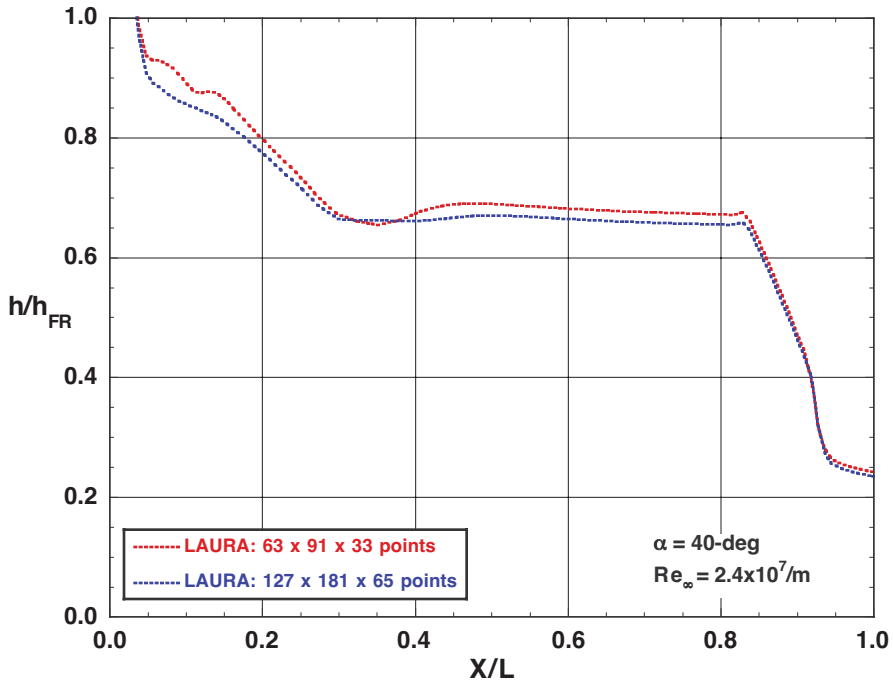

Figure 10: Turbulent Centerline Heating Levels Computed with LAURA for Different Grid Resolution

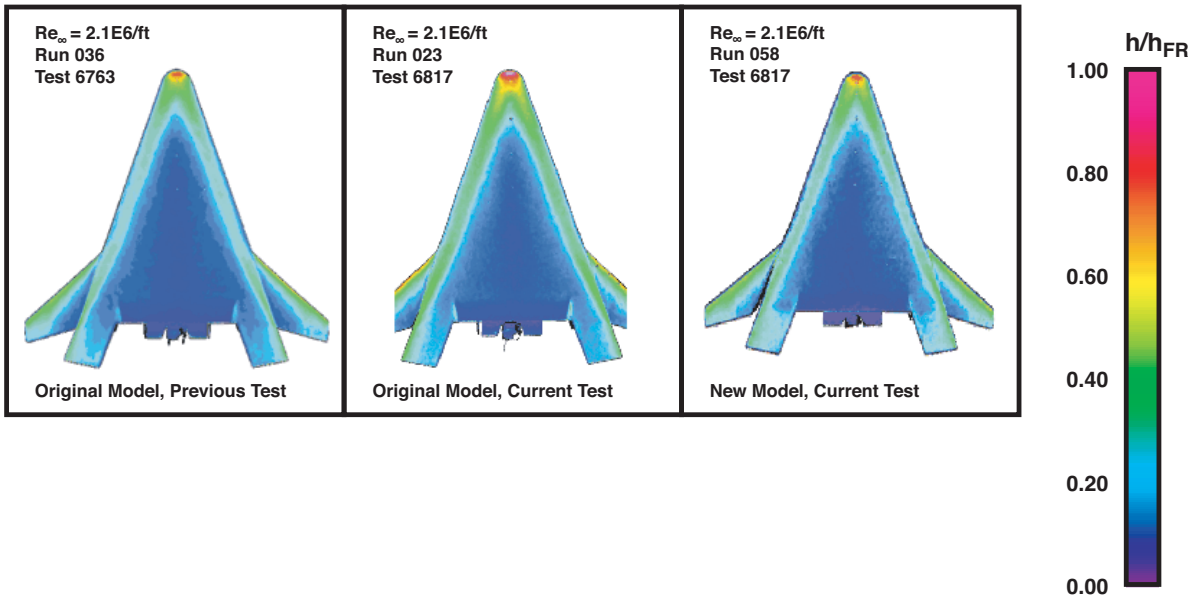

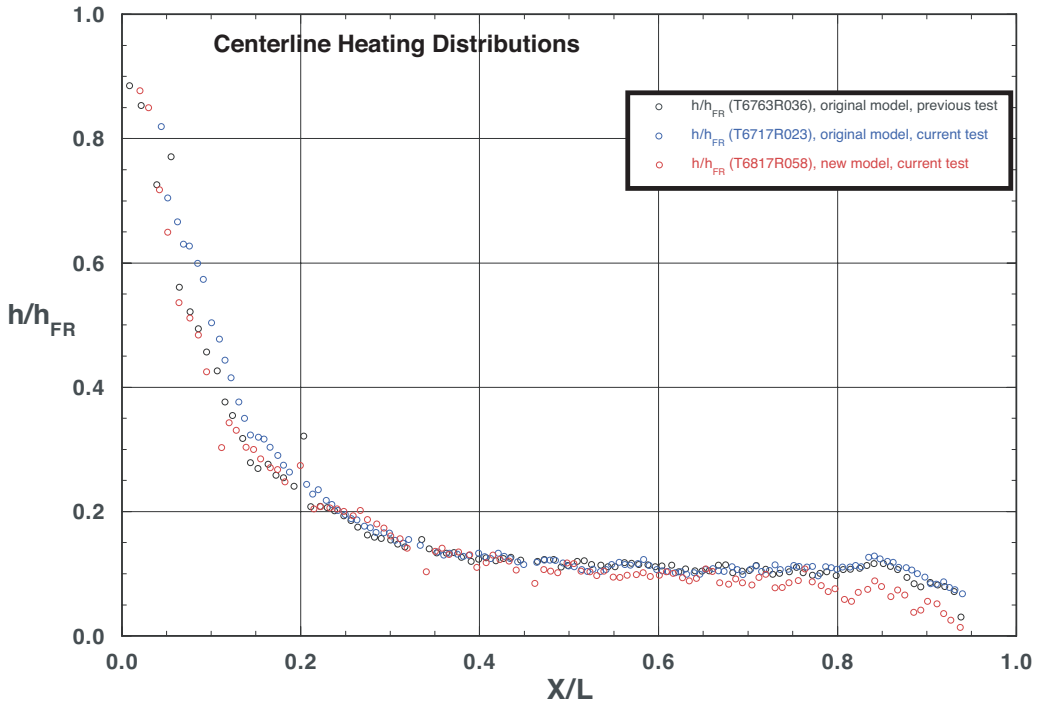

Figure 11: Comparison of Laminar Heating Data on Original and New Smooth Models at $Re_\infty = 2.1 \times 10^6$/ft, α = 40-deg

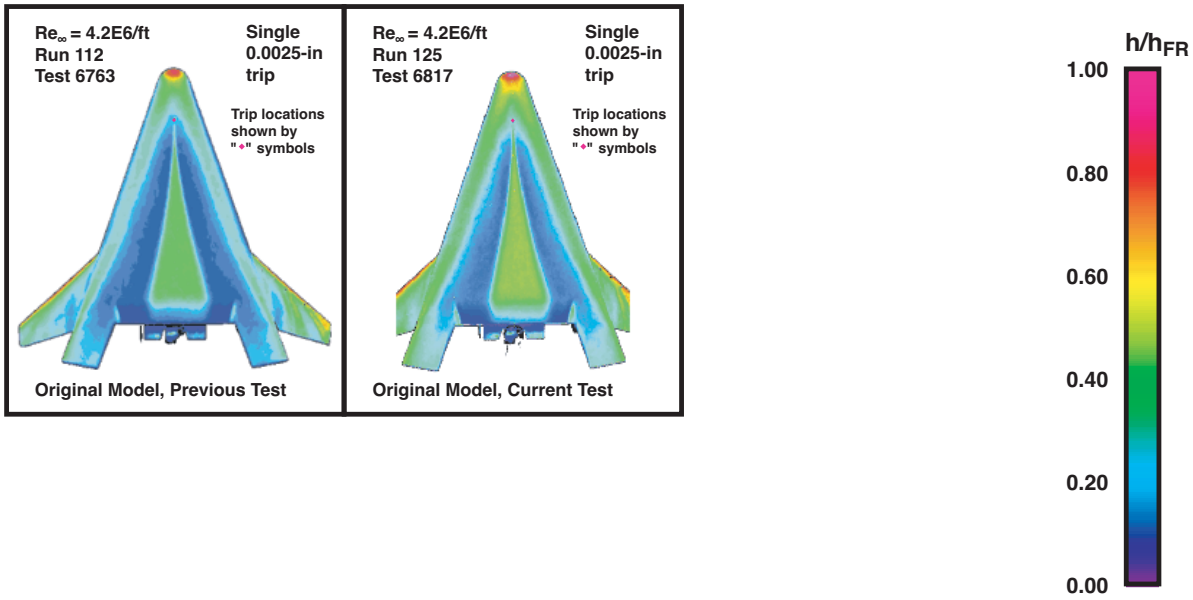

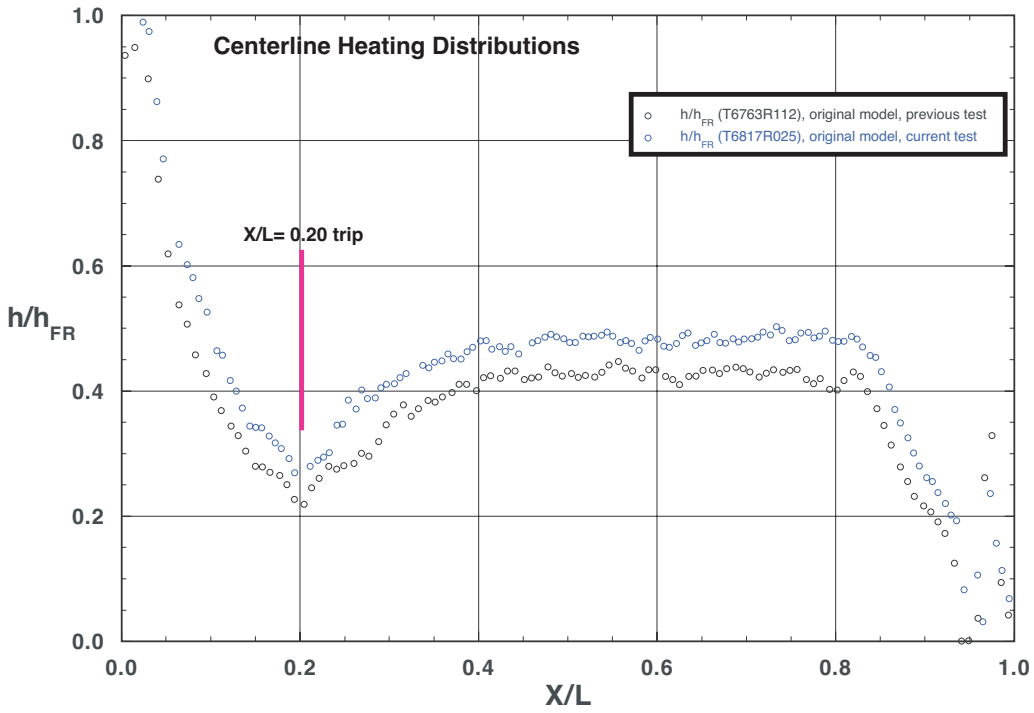

Figure 12: Comparison of 0.0025-in. Trip Heating Data on Original Model with Data from Previous Test at $Re_\infty = 4.2 \times 10^6$/ft, α = 40-deg

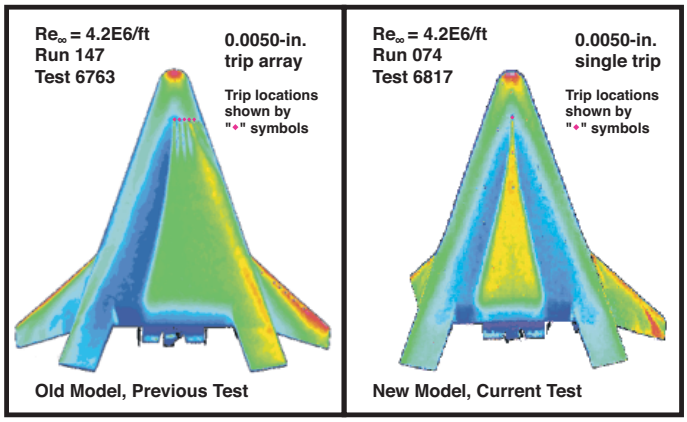

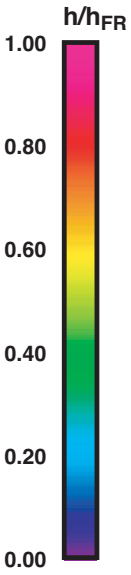

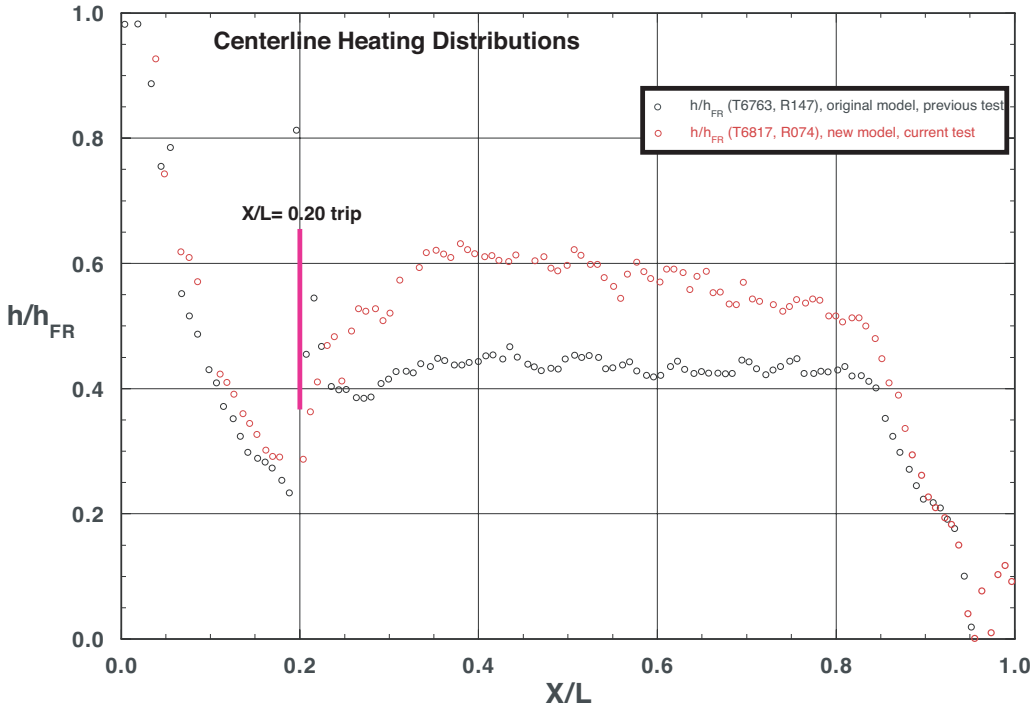

Figure 13: Comparison of 0.0050-in. Trip Heating Data on New Model with Original Model Data from Previous Test at $Re_\infty = 4.2 \times 10^6$/ft, α = 40-deg

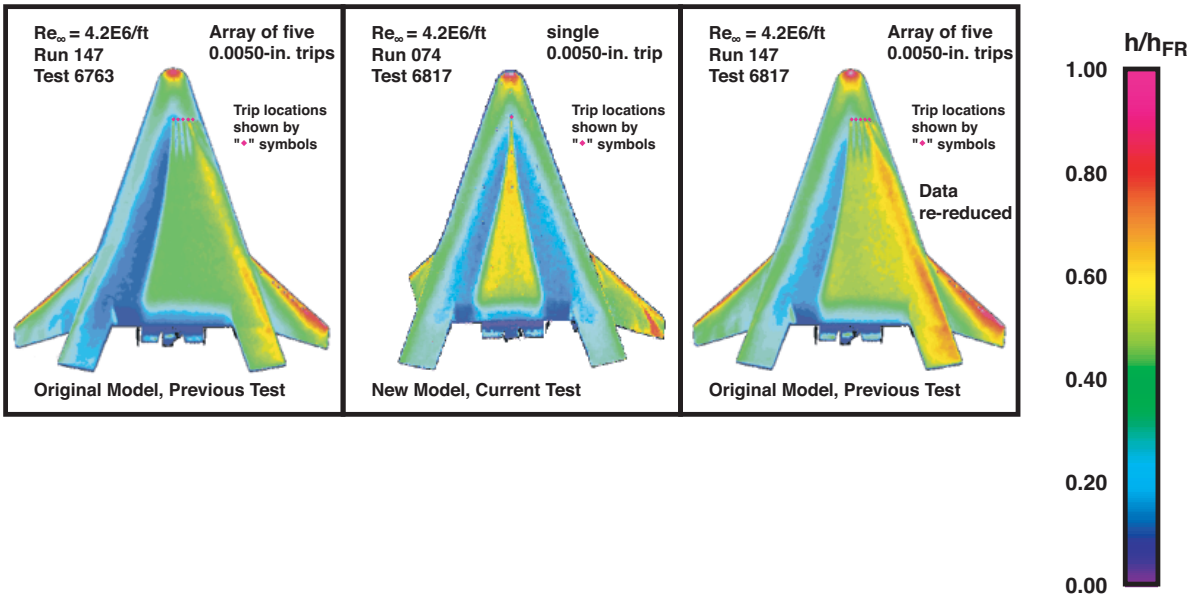

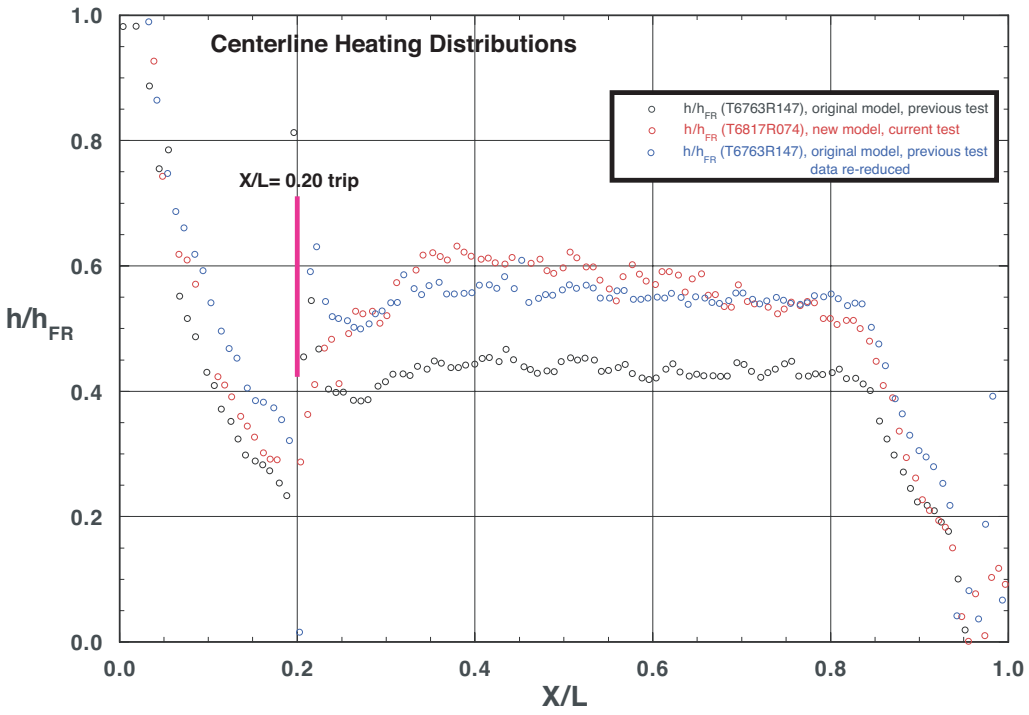

Figure 14: Comparison of 0.0050-in. Trip Heating Data on Original and New Models from Current Test with Re-Reduced Data from Previous Test at $Re_\infty = 4.2 \times 10^6$/ft, α = 40-deg

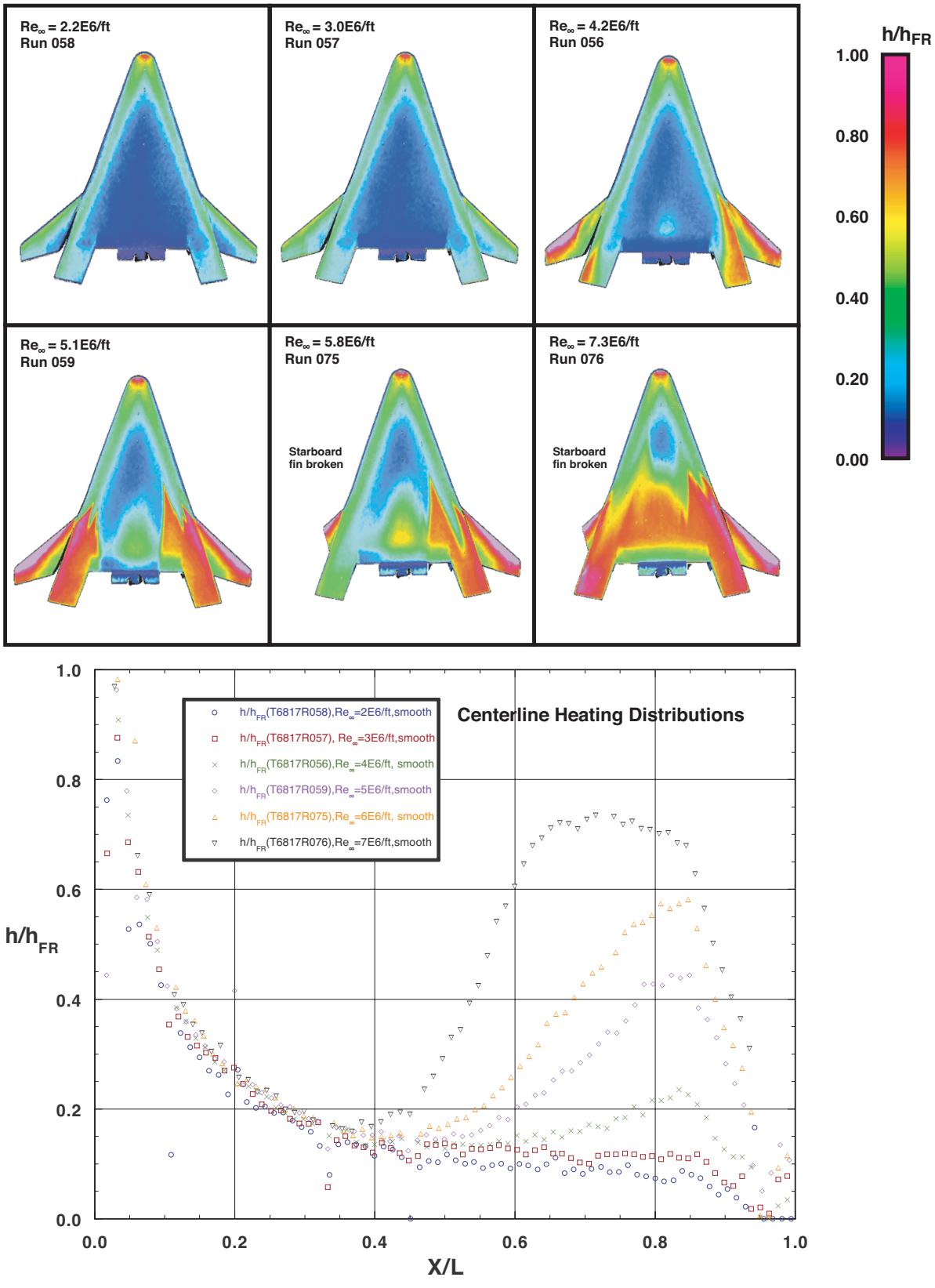

Figure 15: Effect of Reynolds Number on (new) Smooth Model at α = 40-deg

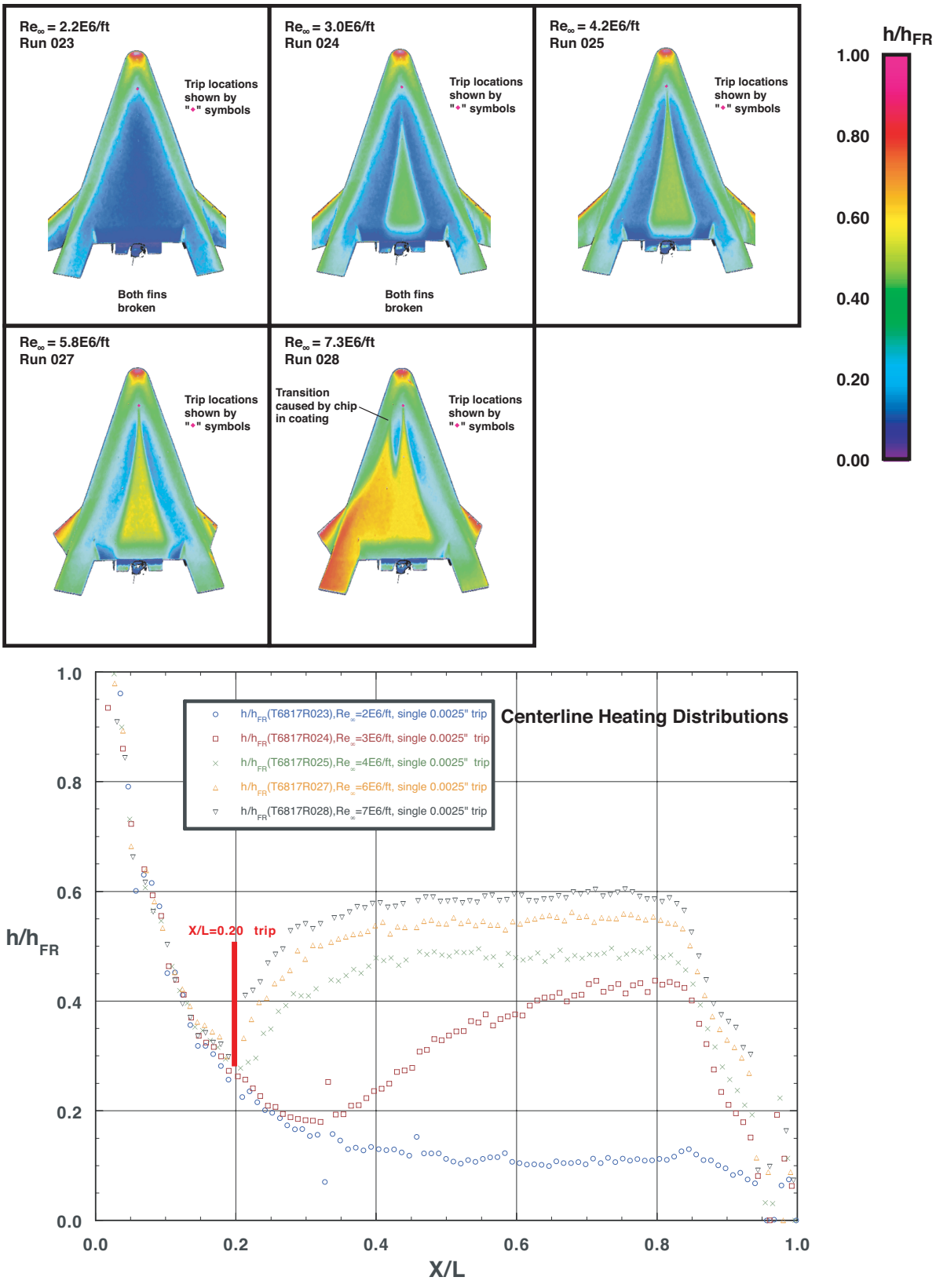

Figure 16: Effect of Reynolds Number on (original) Smooth Model with 0.0025-in. Trip at X/L=0.20 at α = 40-deg

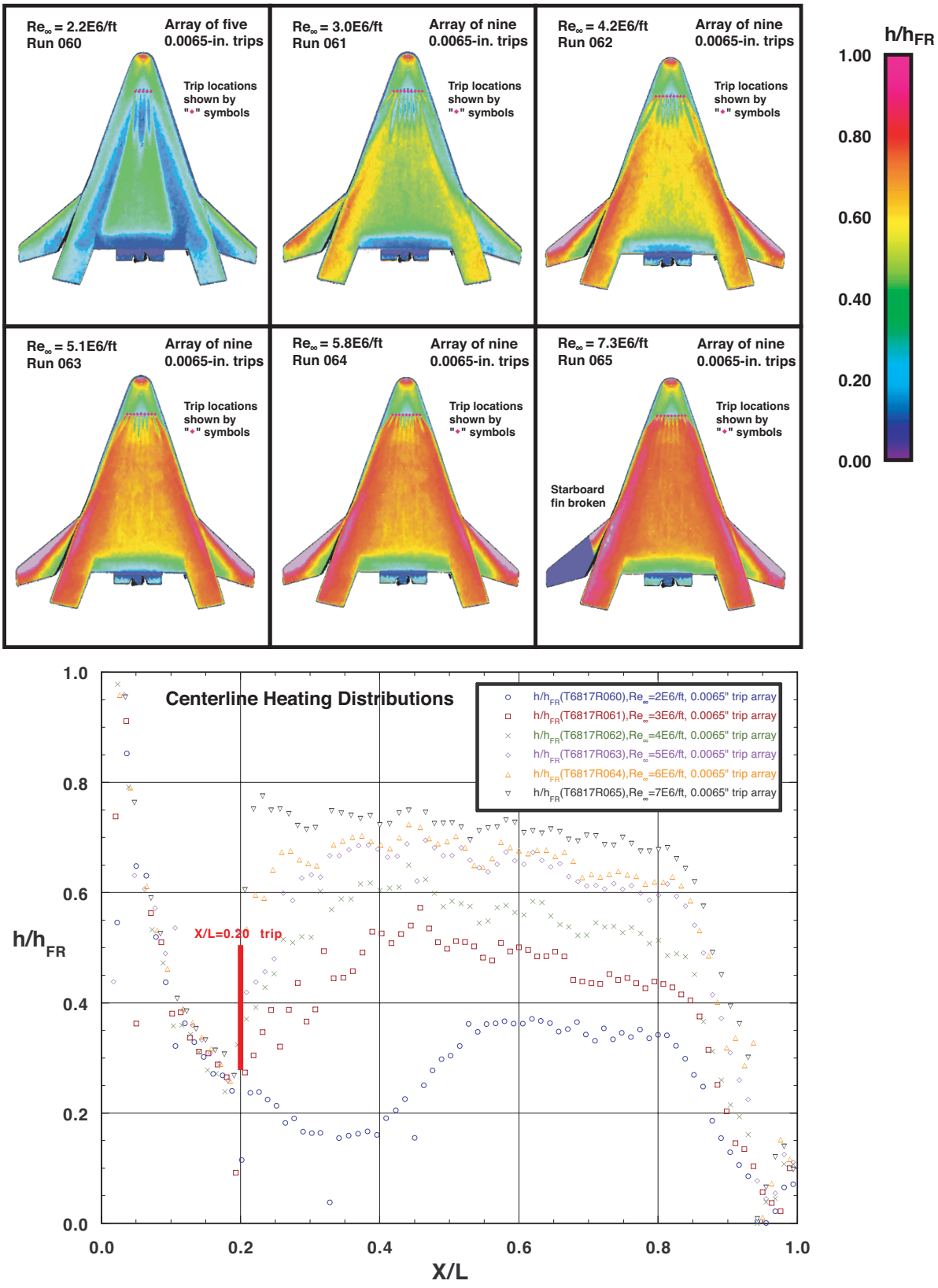

Figure 17: Effect of Reynolds Number on (new) Smooth Model with 0.0065-in. Trip Array at X/L=0.20 at α = 40-deg

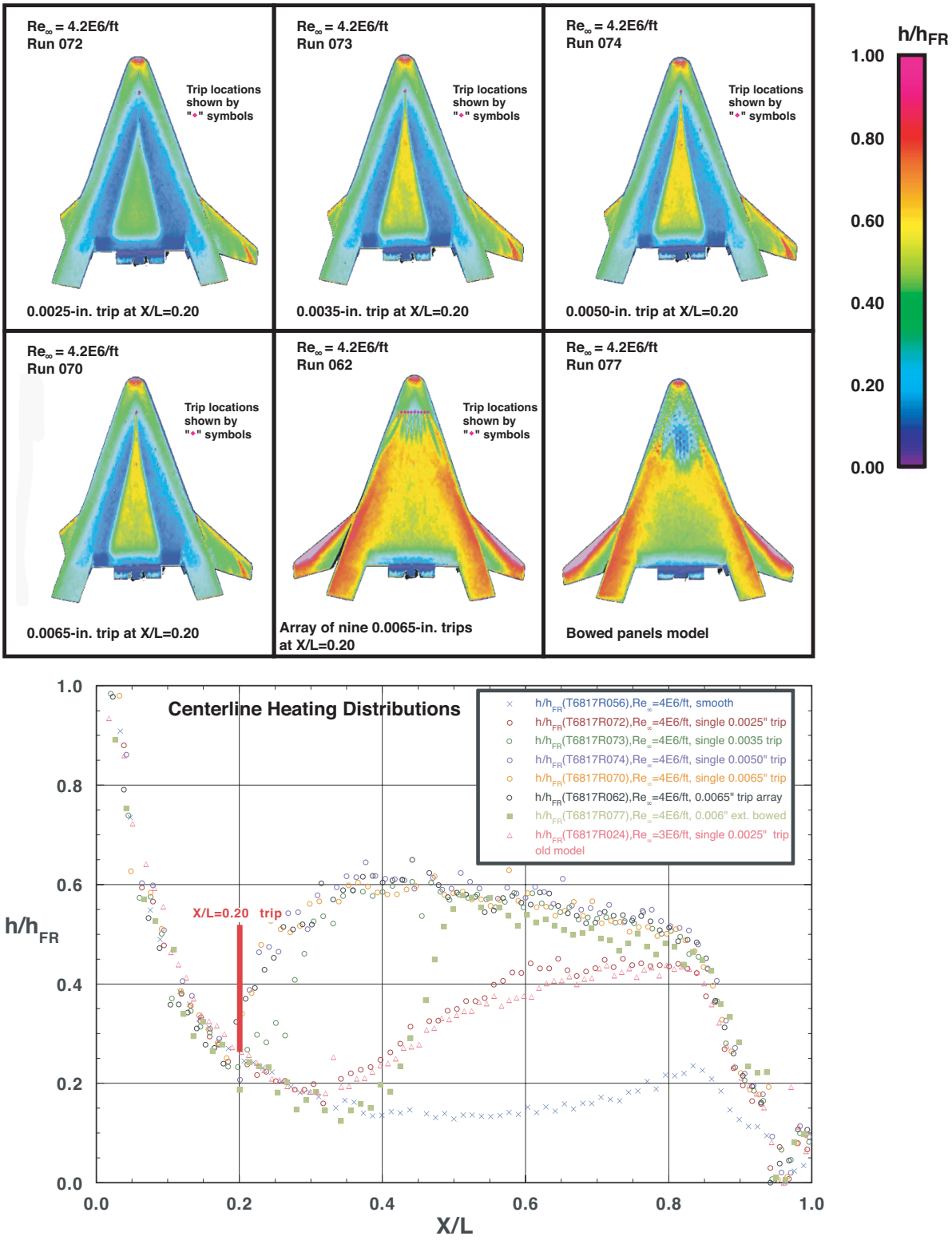

Figure 18: Effect of Trip Height on Smooth Model Heating at $Re_\infty = 4.2 \times 10^6$/ft, α = 40-deg

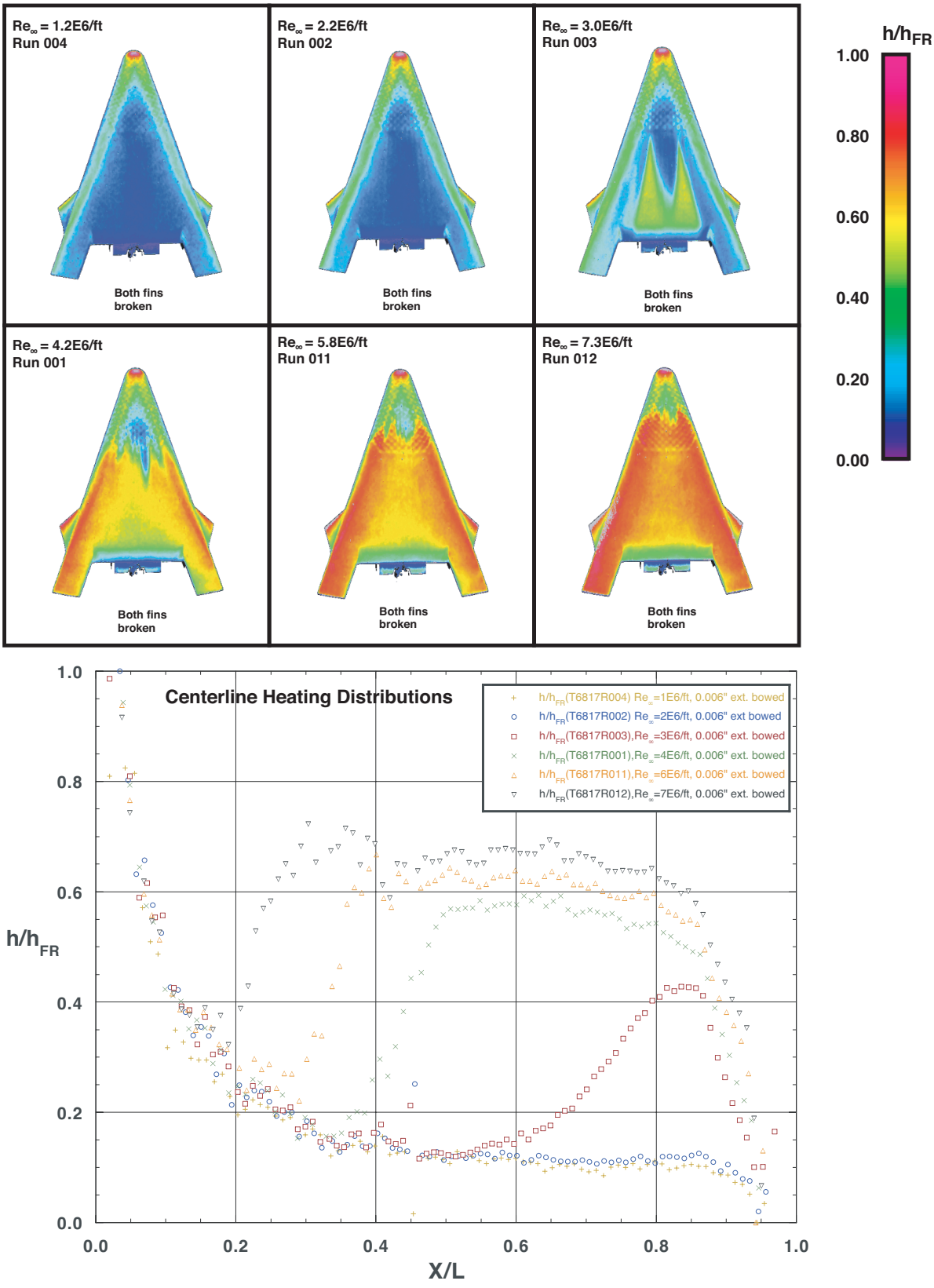

Figure 19: Effect of Reynolds Number on (orignal) Extended Bowed Panel Model at α = 40-deg

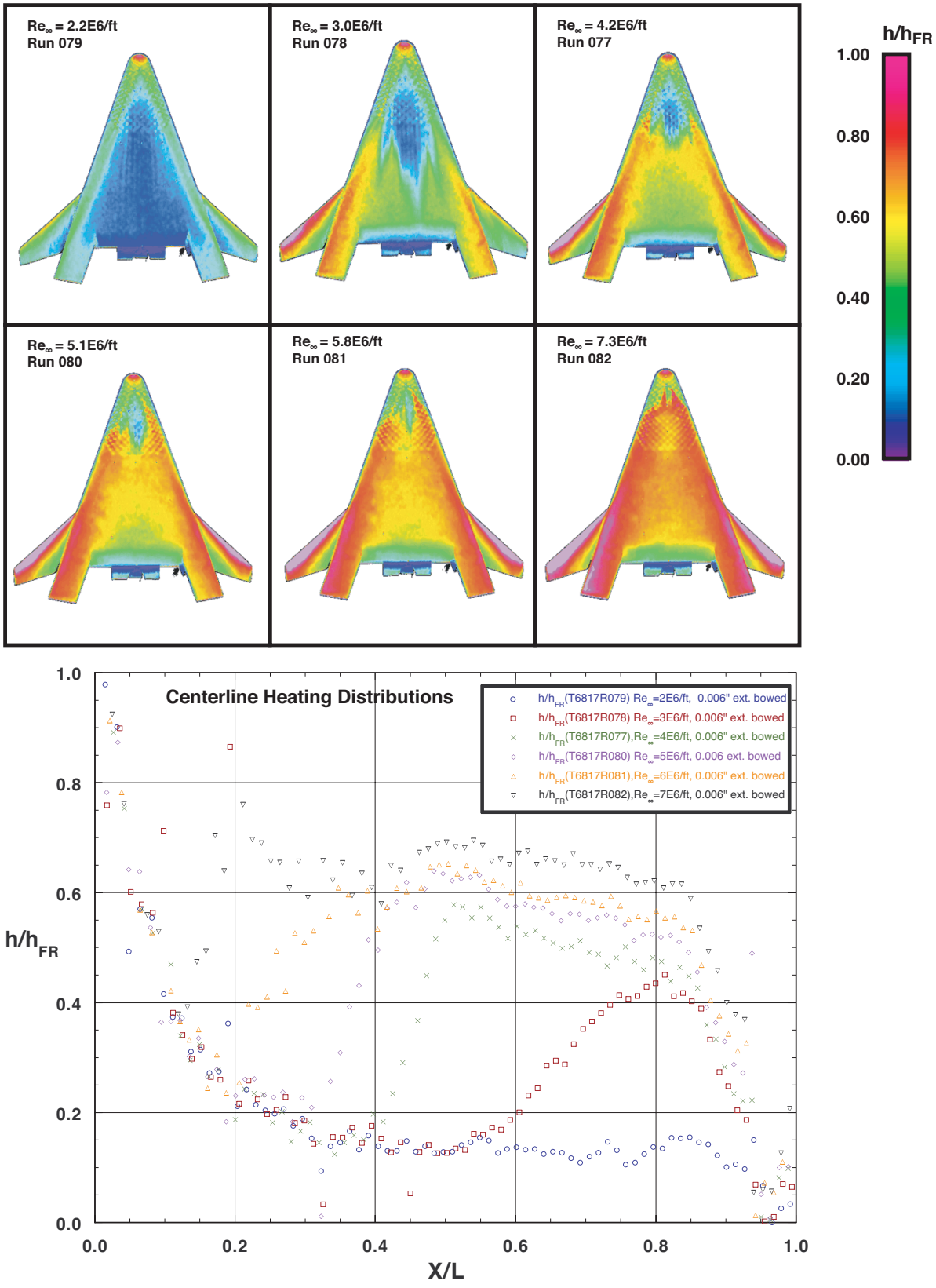

Figure 20: Effect of Reynolds Number on (new) Extended Bowed Panel Model at α = 40-deg

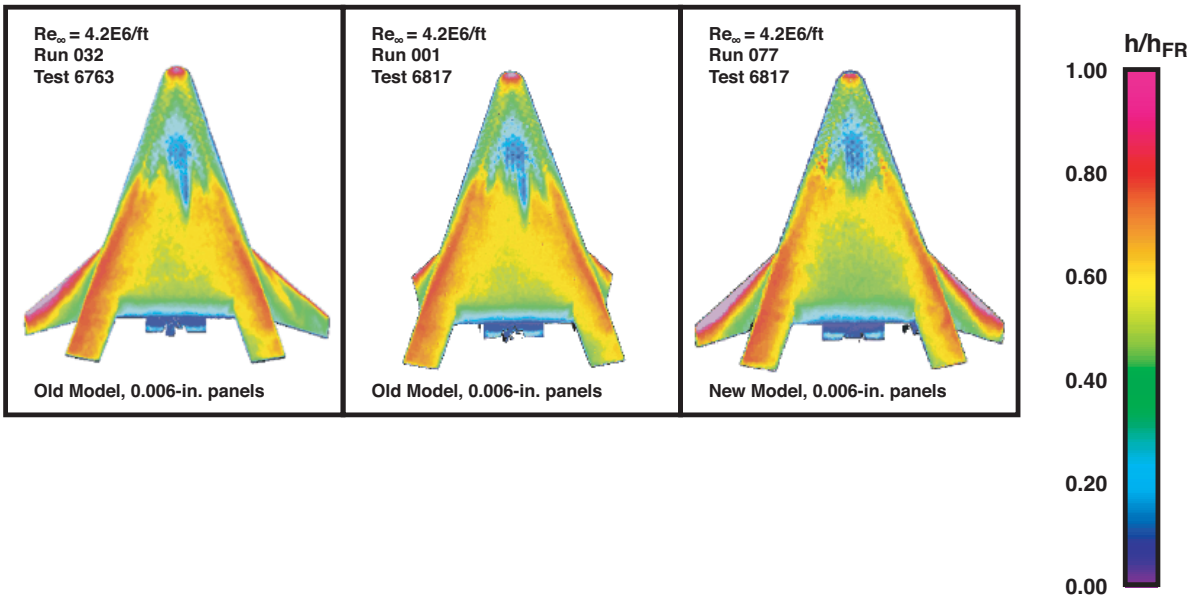

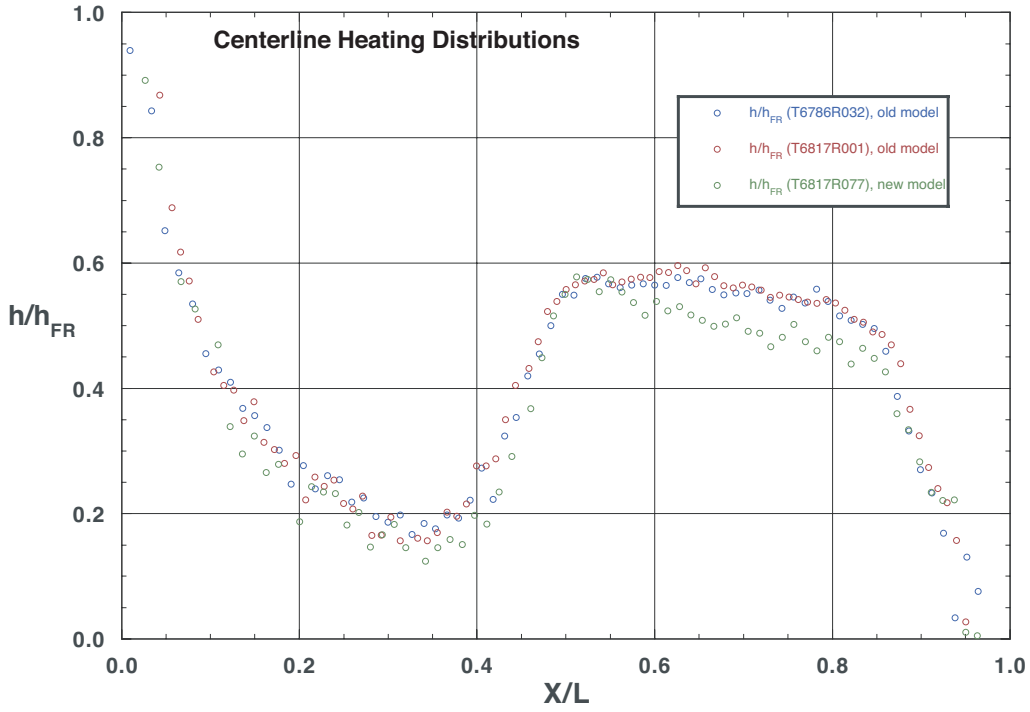

Figure 21: Comparison of Heating Data on Original and New Bowed Panels Models, $Re_\infty = 4.2 \times 10^6$/ft, α = 40-deg

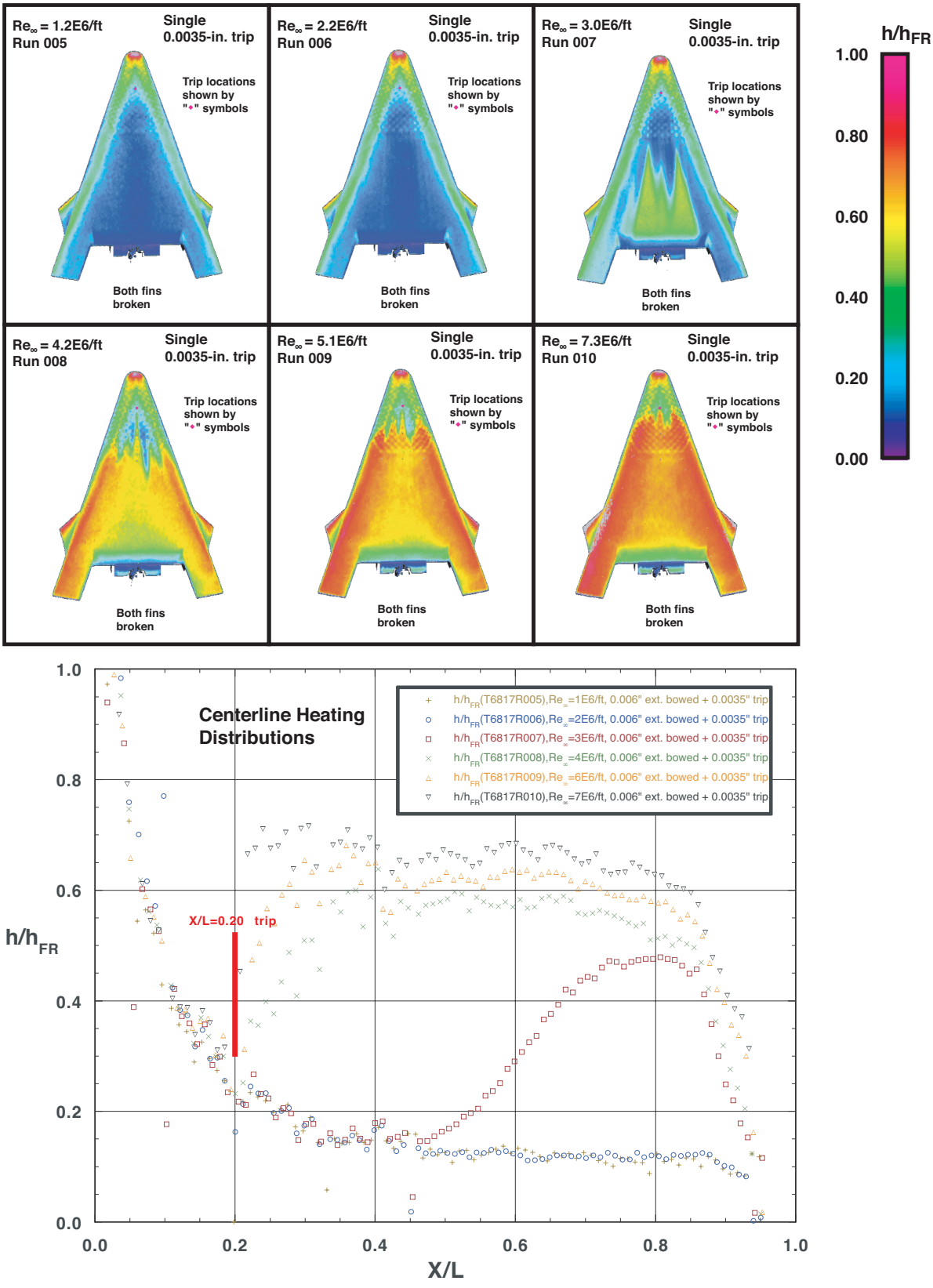

Figure 22: Effect of Reynolds Number on (original) Extended Bowed Panel Model with 0.0035-in. Trip at X/L=0.20 at α = 40-deg

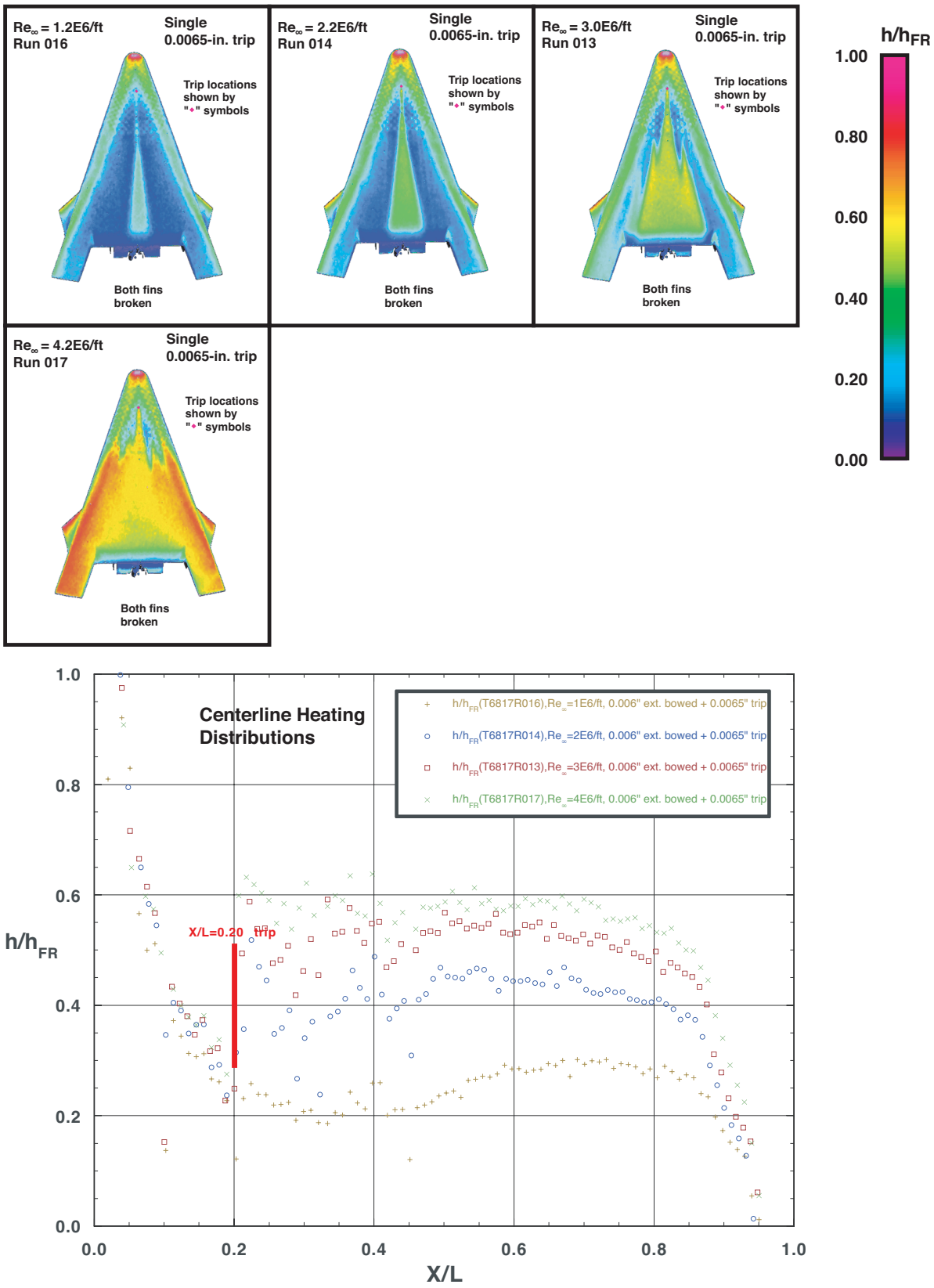

Figure 23: Effect of Reynolds Number on (original) Extended Bowed Panel Model with 0.0065-in. Trip at X/L=0.20 at α = 40-deg

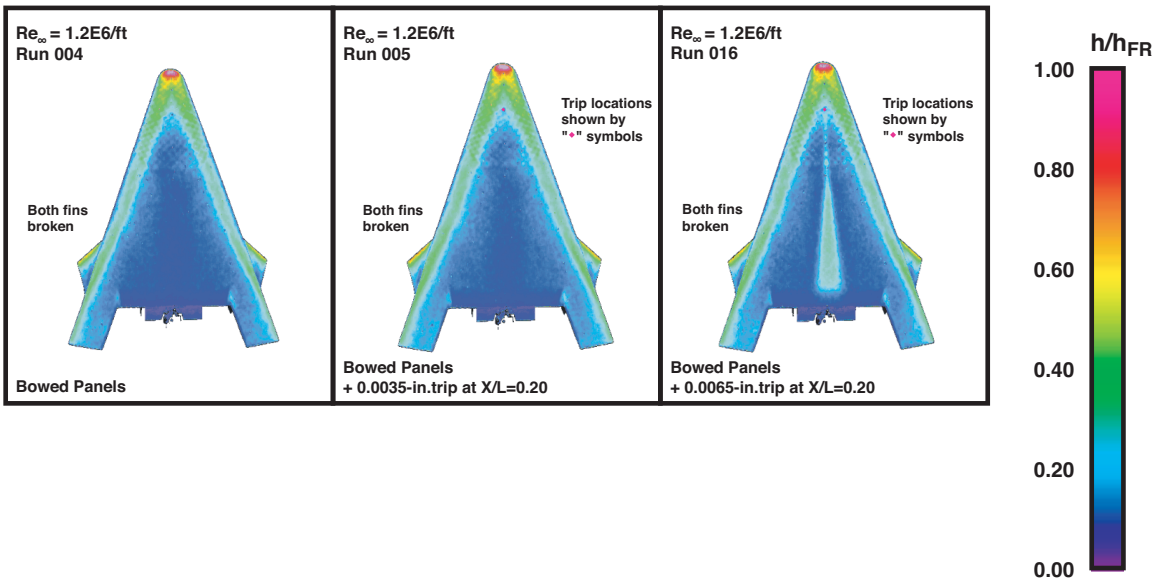

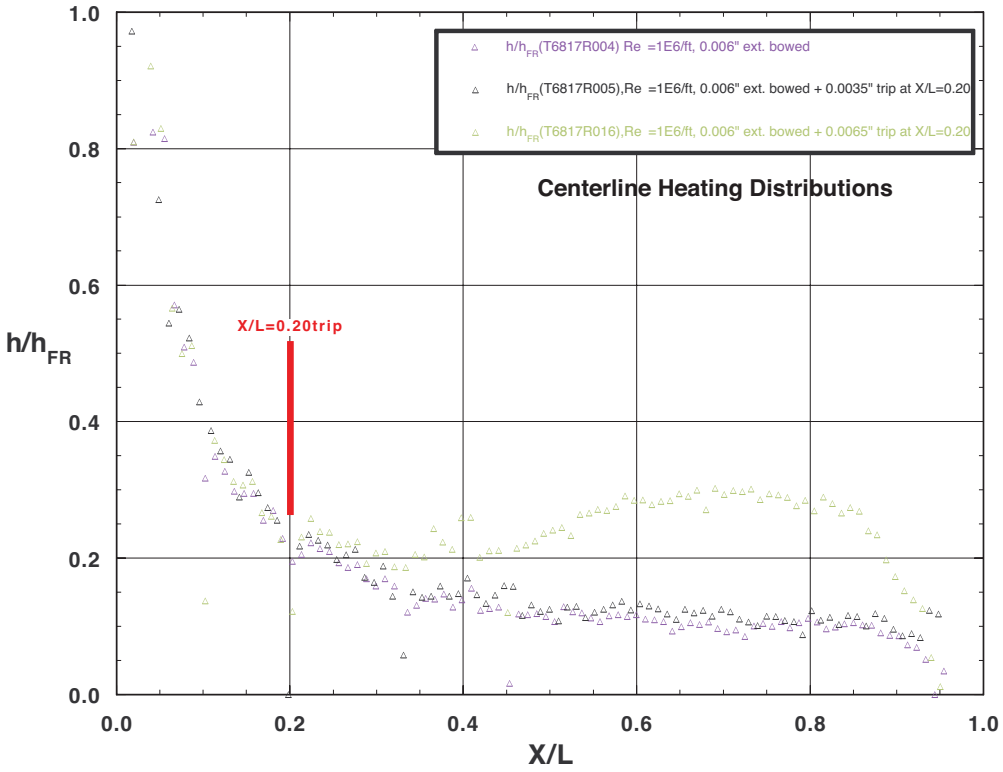

Figure 24: Effects of Trips and/or Panels on Heating at $Re_\infty = 1.1 \times 10^6$/ft, α = 40-deg

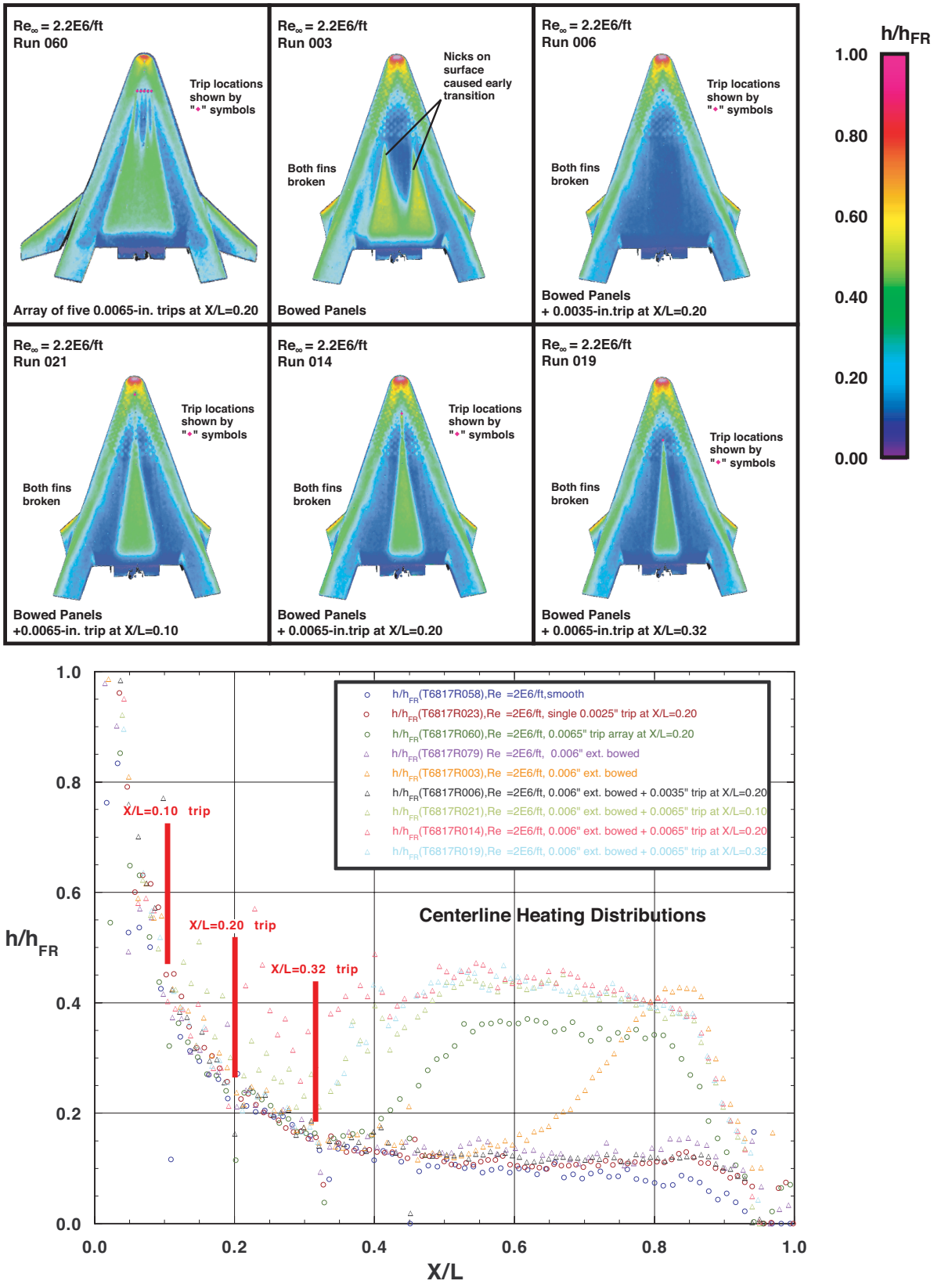

Figure 25: Effects of Trips and/or Panels on Heating at $Re_\infty = 2.2 \times 10^6$/ft, $\alpha = 40$-deg

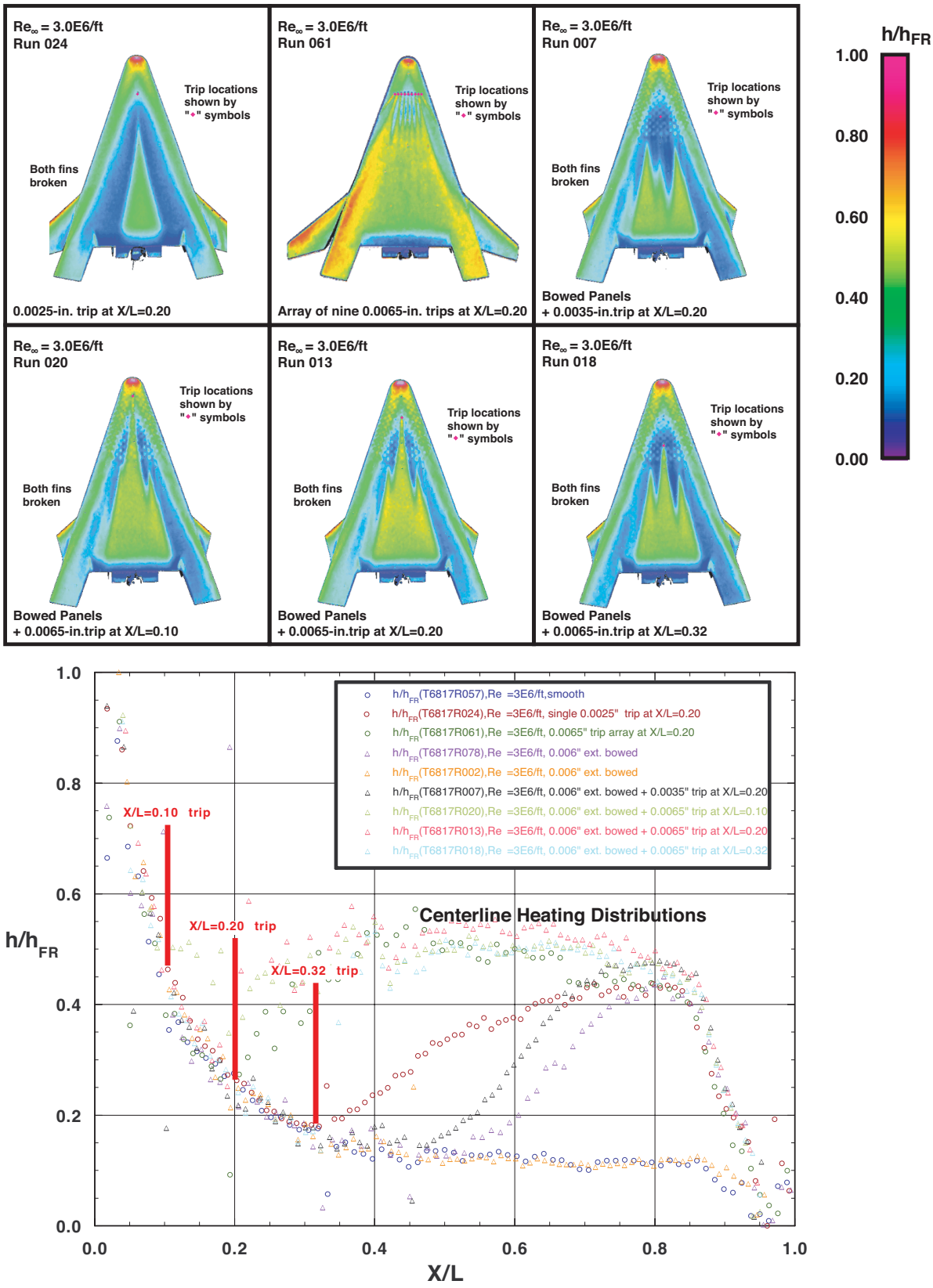

Figure 26: Effects of Trips and/or Panels on Heating at $Re_\infty = 3.0 \times 10^6$/ft, α = 40-deg

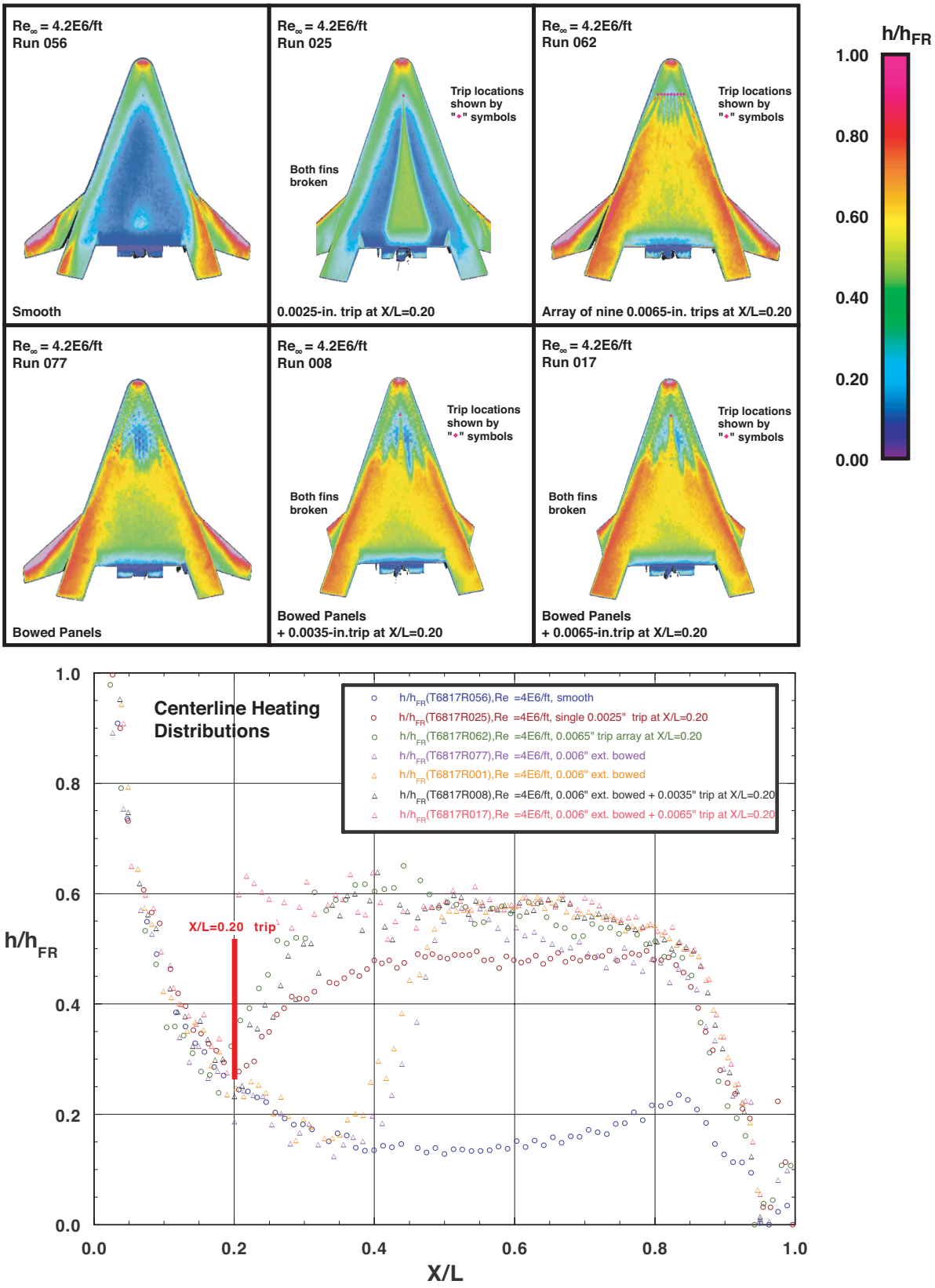

Figure 27: Effects of Trips and/or Panels on Heating at $Re_\infty = 4.2 \times 10^6$/ft, α = 40-deg

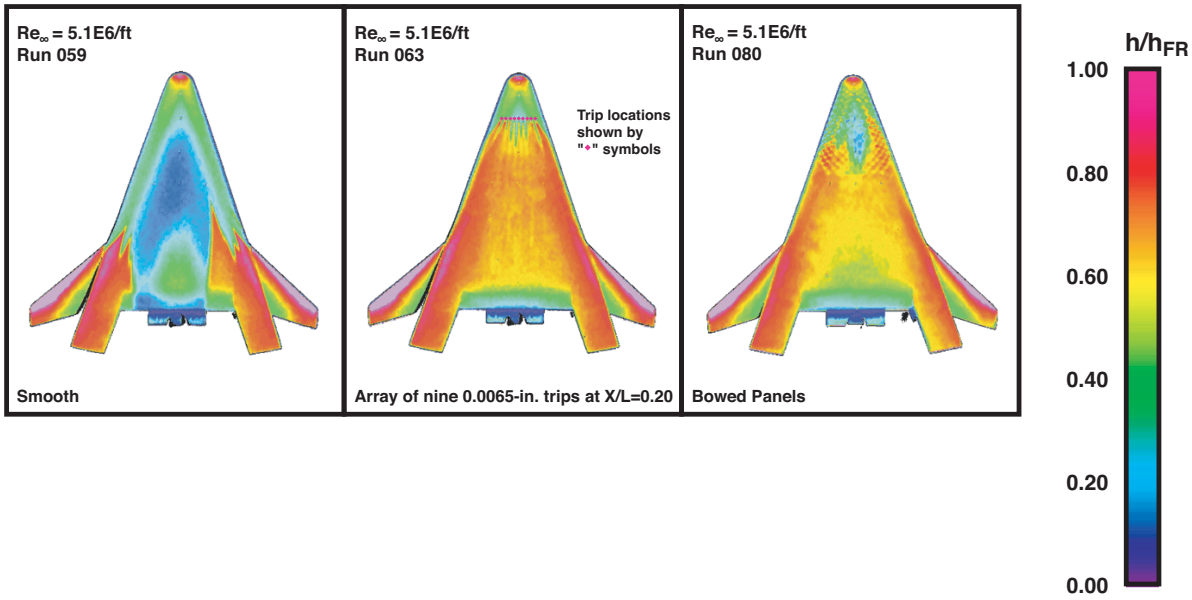

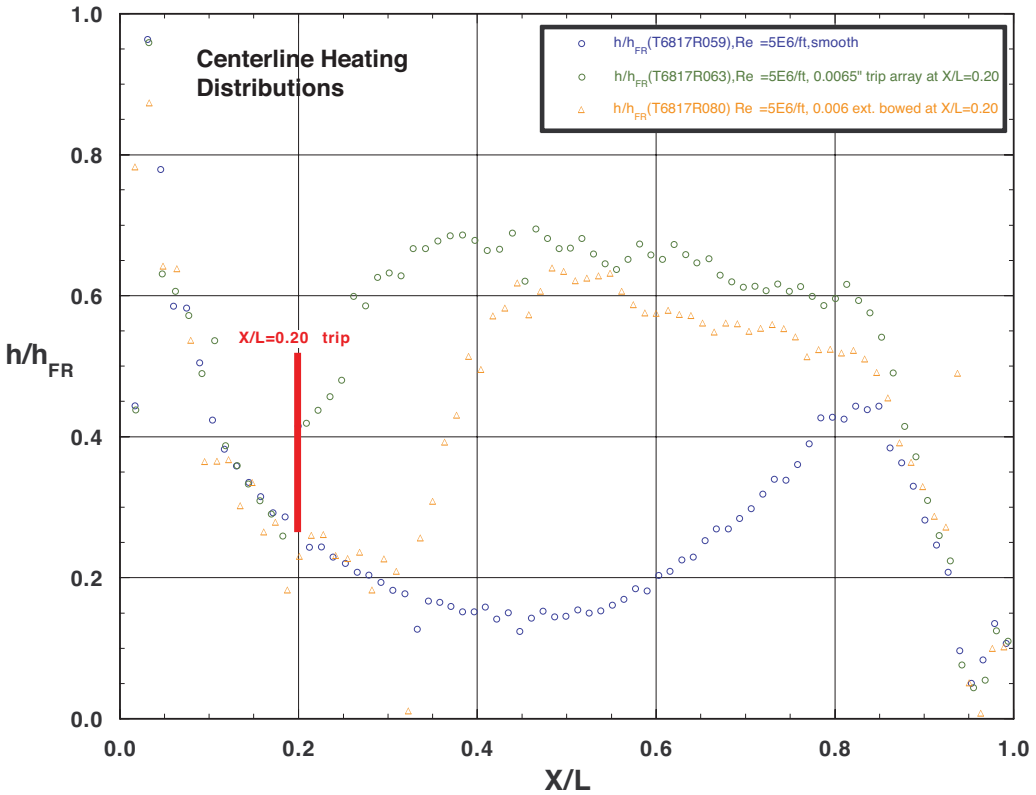

Figure 28: Effects of Trips and/or Panels on Heating at $Re_\infty = 5.1 \times 10^6$/ft, α = 40-deg

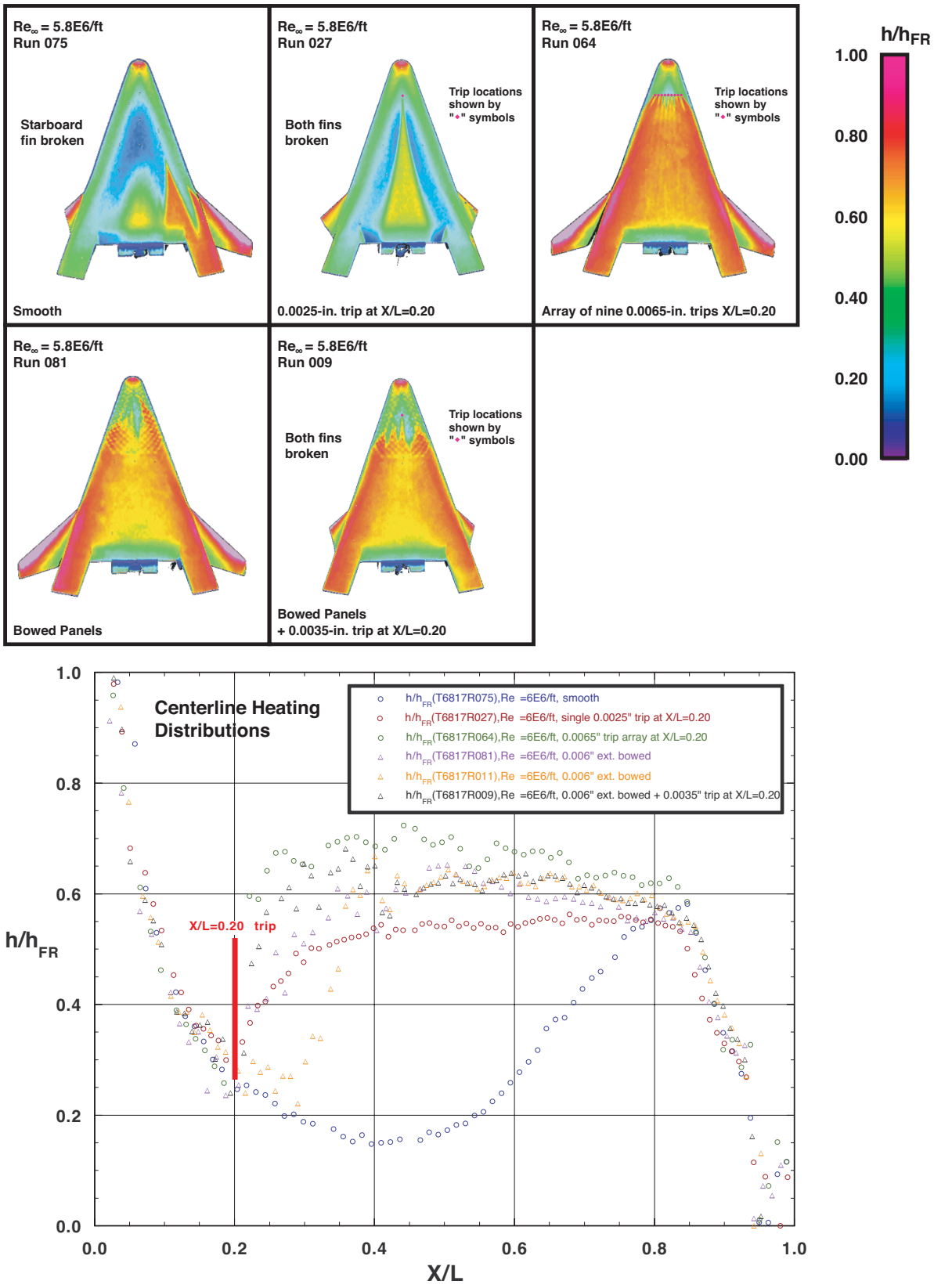

Figure 29: Effects of Trips and/or Panels on Heating at $Re_\infty = 5.8 \times 10^6$/ft, α = 40-deg

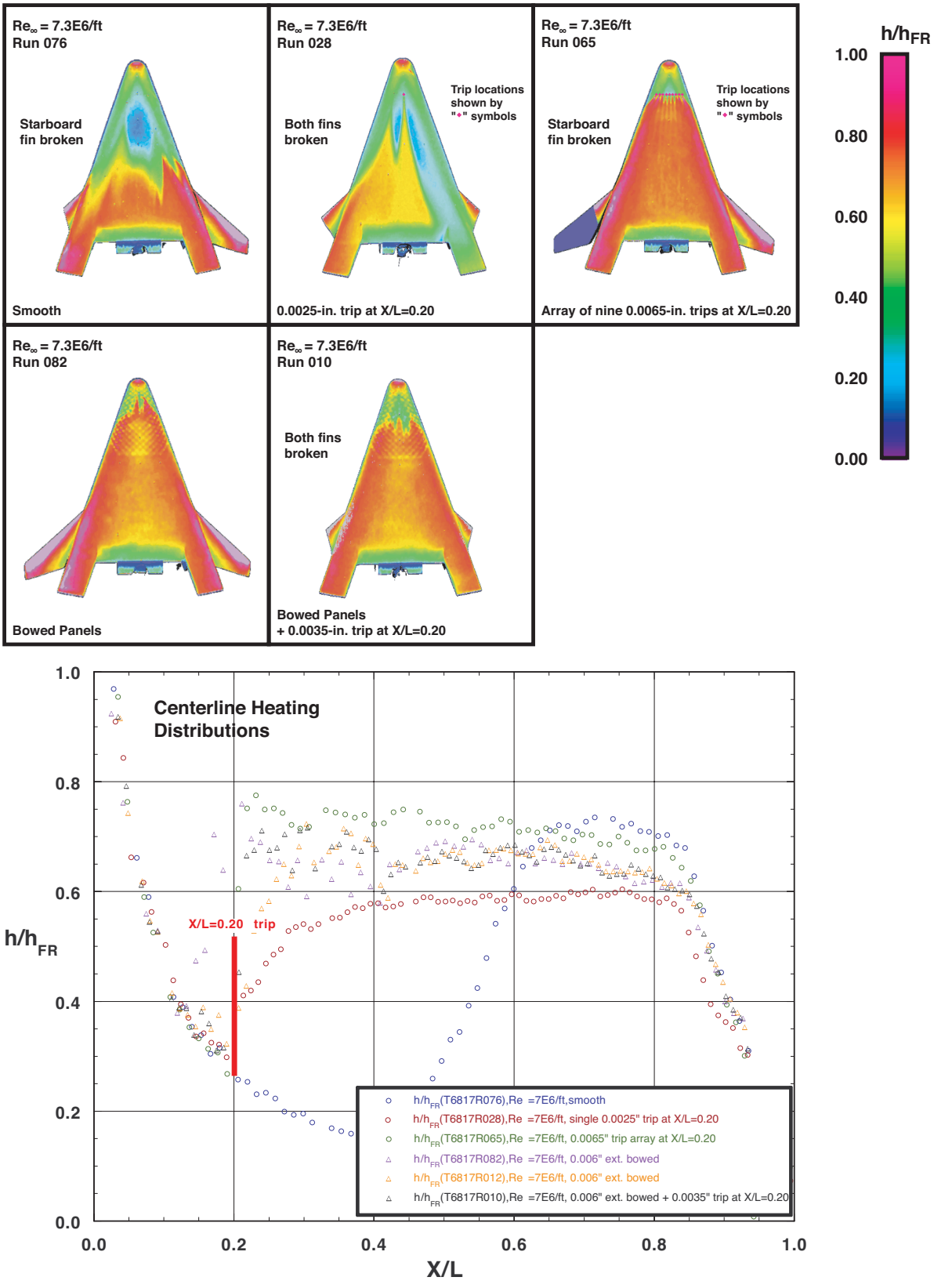

Figure 30: Effects of Trips and/or Panels on Heating at $Re_\infty = 7.3 \times 10^6$/ft, α = 40-deg

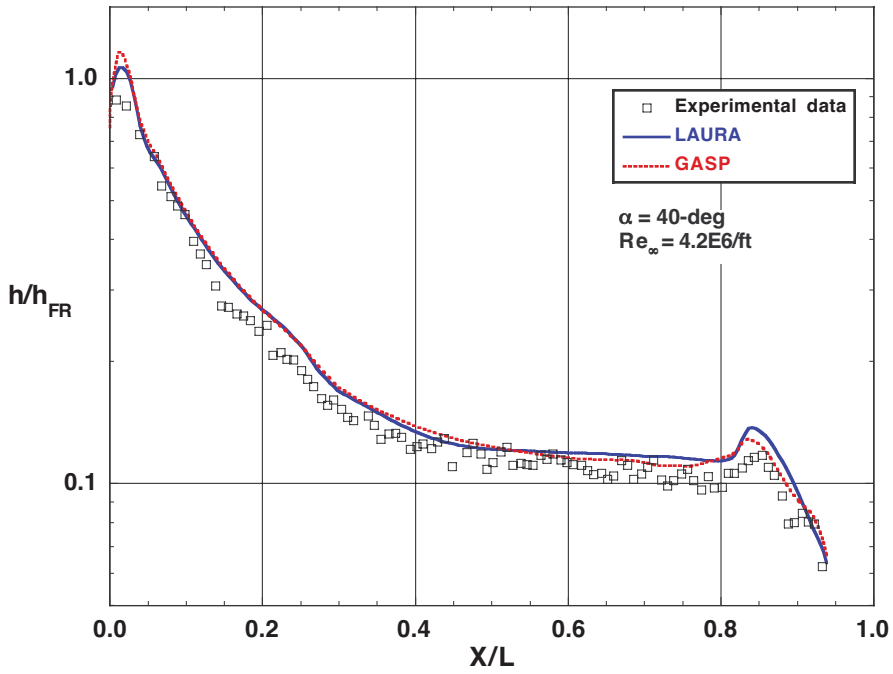

Figure 31: Comparison of Laminar Heating Data with Predictions at $Re_\infty = 4.2 \times 10^6$/ft, α = 40-deg

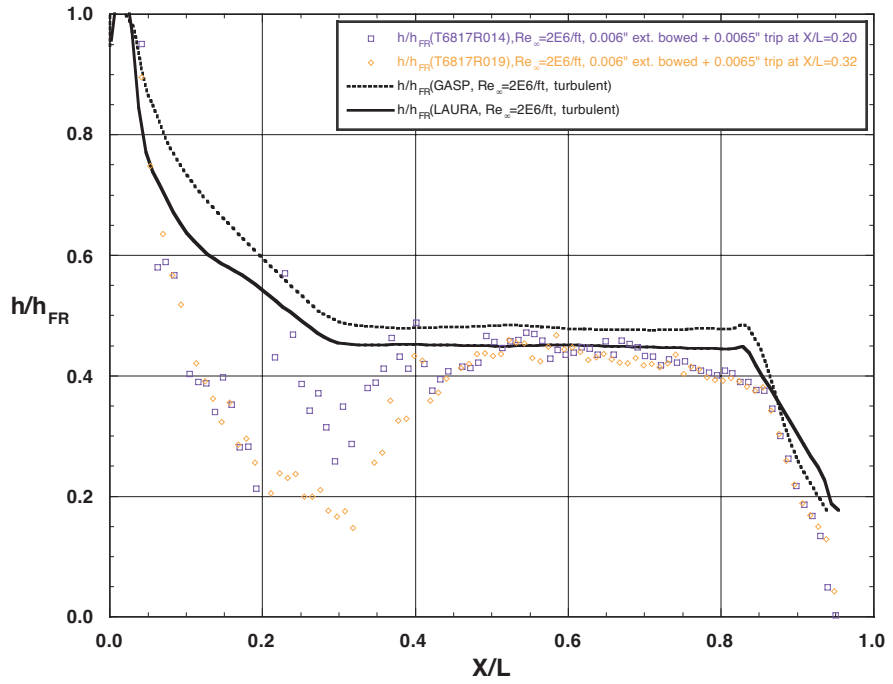

Figure 32: Comparison of Turbulent Heating Data with Predictions at $Re_\infty = 2.2 \times 10^6$/ft, α = 40-deg

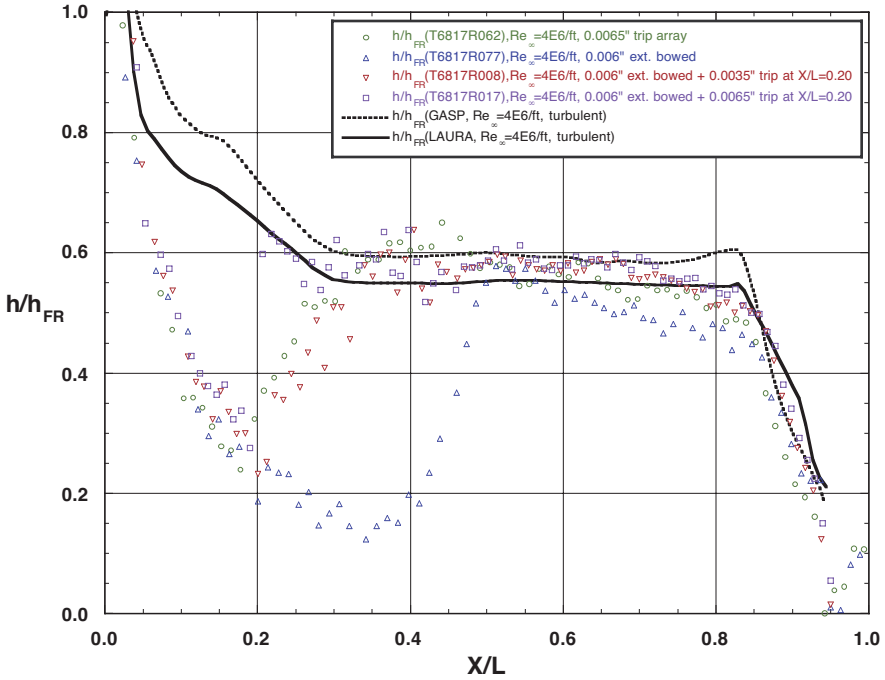

Figure 33: Comparison of Turbulent Heating Data with Predictions at $Re_\infty = 4.2 \times 10^6$/ft, α = 40-deg

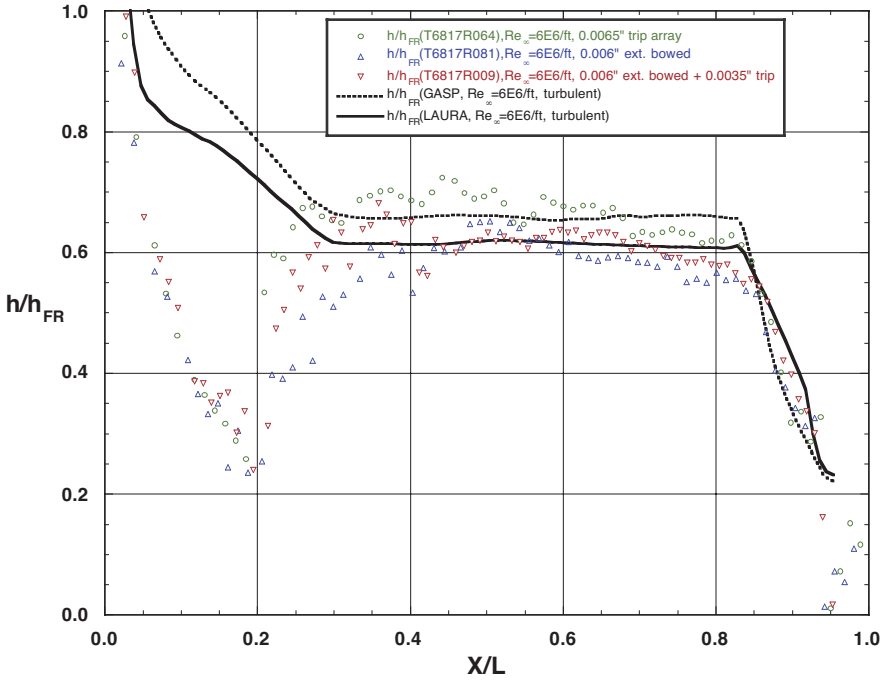

Figure 34: Comparison of Turbulent Heating Data with Predictions at $Re_\infty = 5.8 \times 10^6$/ft, α = 40-deg

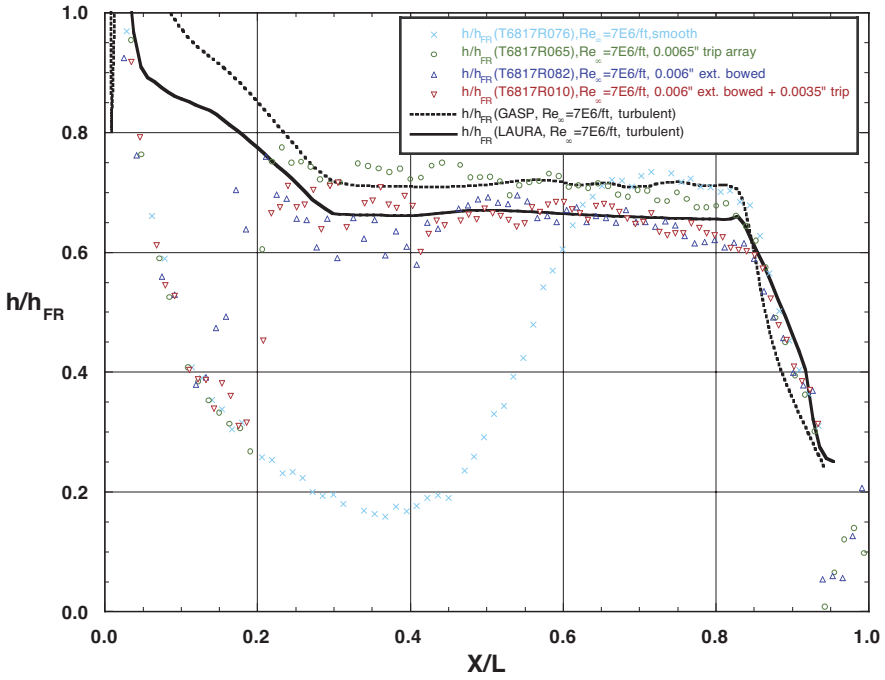

Figure 35: Comparison of Turbulent Heating Data with Predictions at $Re_\infty = 7.3 \times 10^6$/ft, α = 40-deg

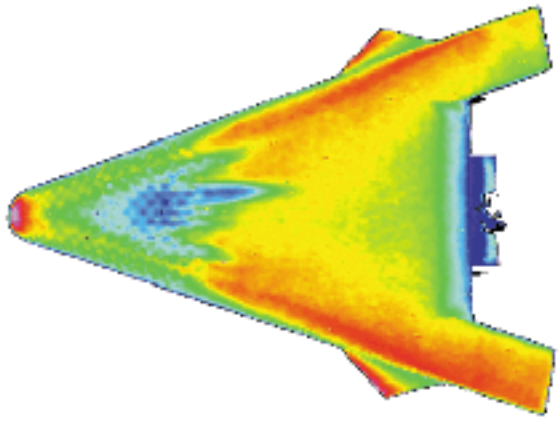

Figure A. 1: Extended Bowed Panel Model, Run 001, α = 40-deg, $Re_\infty = 4.2 \times 10^6$/ft

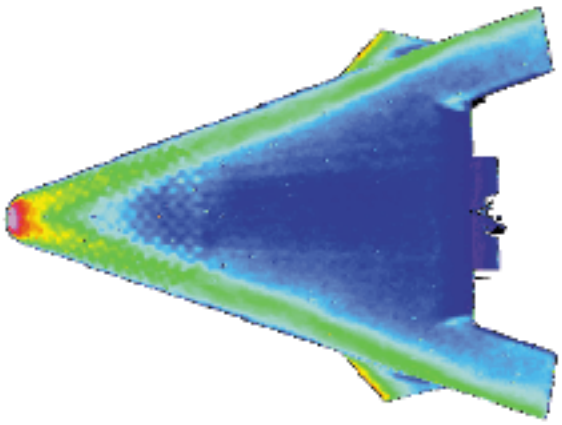

Figure A. 2: Extended Bowed Panel Model, Run 002, α = 40-deg, $Re_\infty = 2.2 \times 10^6$/ft

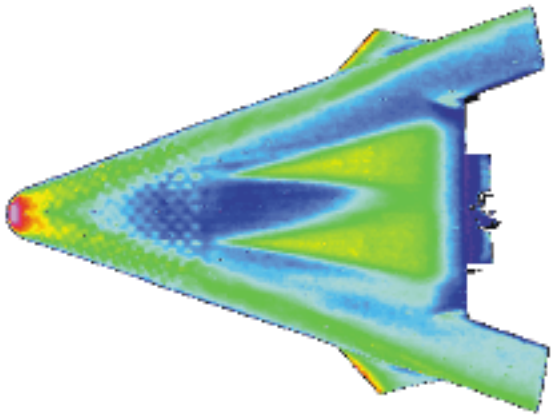

Figure A. 3: Extended Bowed Panel Model, Run 003, α = 40-deg, $Re_\infty = 3.0 \times 10^6$/ft

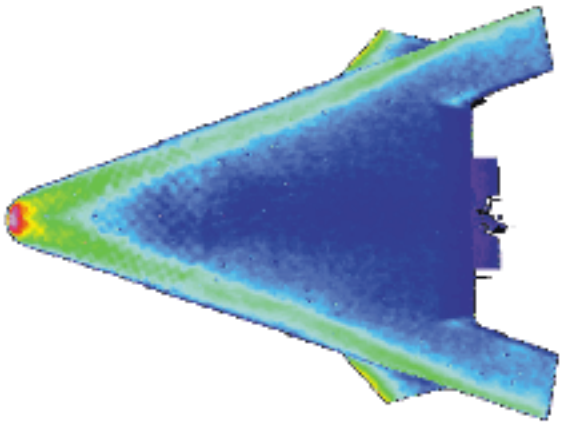

Figure A. 4: Extended Bowed Panel Model, Run 004, α = 40-deg, $Re_\infty = 1.1 \times 10^6$/ft

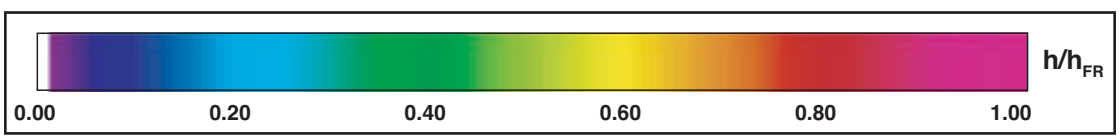

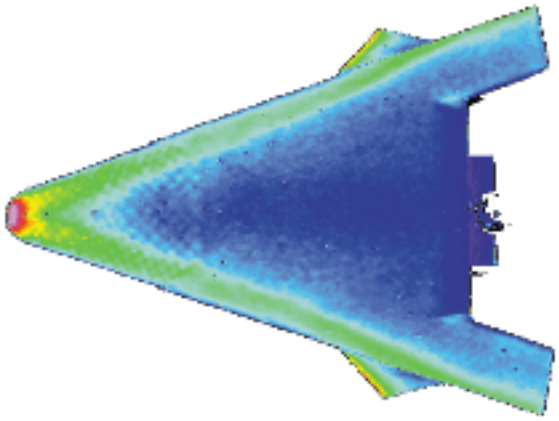

Figure A. 5: Extended Bowed Panel Model with 0.0035-in. Trip at X/L = 0.20, Run 005, α = 40-deg, $Re_\infty = 1.1 \times 10^6$/ft

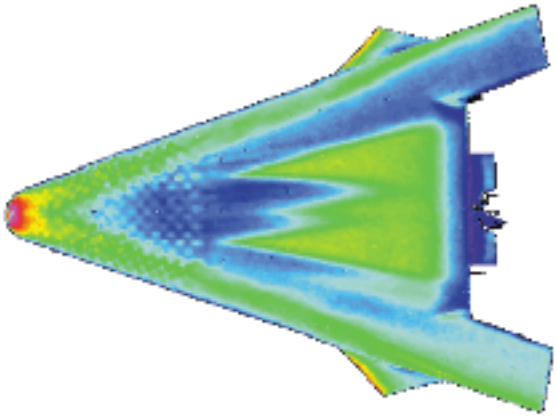

Figure A. 7: Extended Bowed Panel Model with 0.0035-in. Trip at X/L = 0.20, Run 007, α = 40-deg, $Re_\infty = 3.0 \times 10^6$/ft

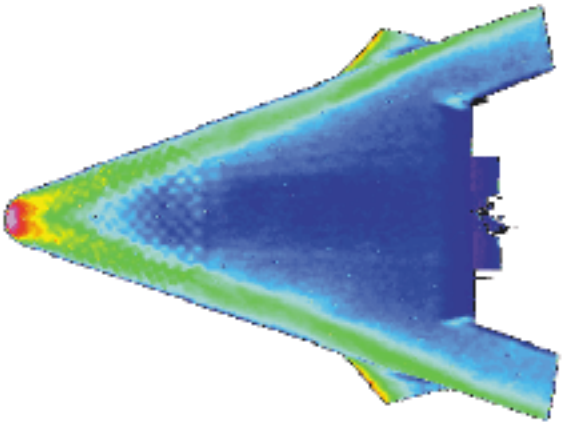

Figure A. 6: Extended Bowed Panel Model with 0.0035-in. Trip at X/L = 0.20, Run 006, α = 40-deg, $Re_\infty = 2.2 \times 10^6$/ft

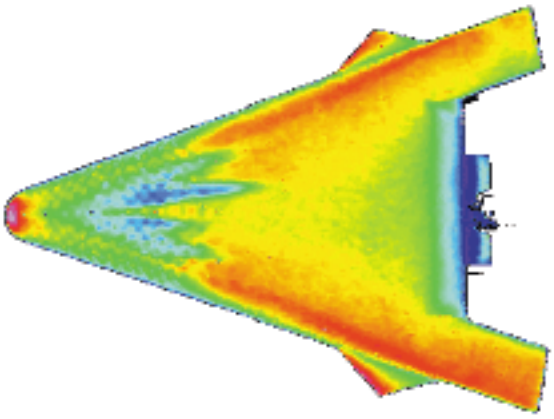

Figure A. 8: Extended Bowed Panel Model with 0.0035-in. Trip at X/L = 0.20, Run 008, α = 40-deg, $Re_\infty = 4.2 \times 10^6$/ft

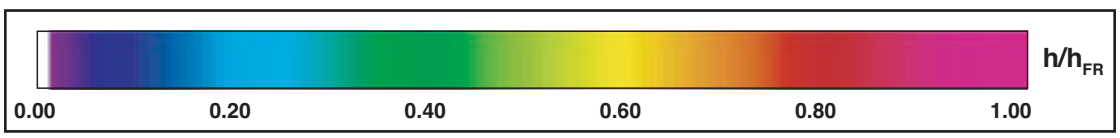

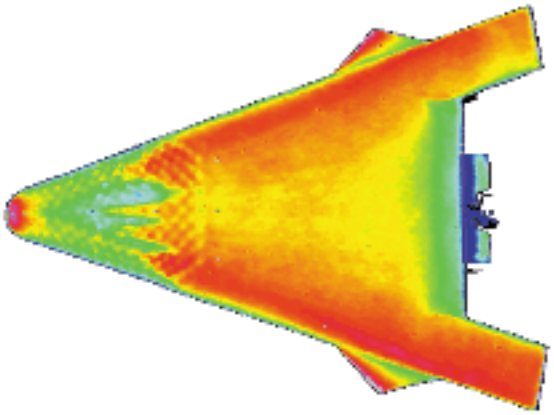

Figure A. 9: Extended Bowed Panel Model with 0.0035-in. Trip at X/L=0.20, Run 009, α = 40-deg, Re_∞=5.8 × 10^6/ft

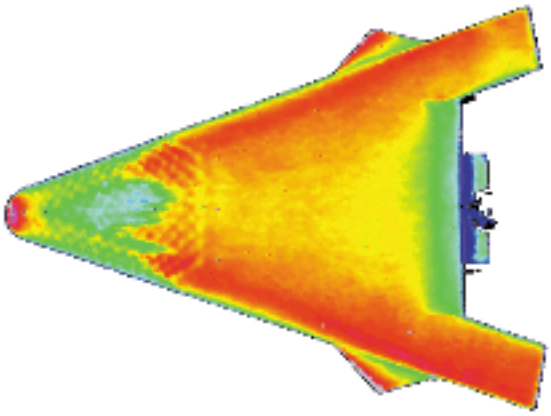

Figure A. 11: Extended Bowed Panel Model , Run 011, α = 40-deg, Re_∞ = 5.8 × 10^6/ft

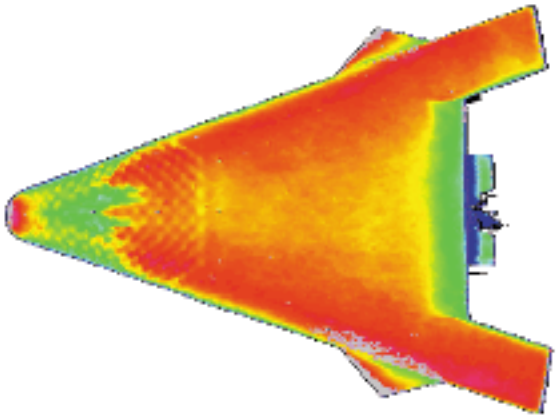

Figure A. 10: Extended Bowed Panel Model with 0.0035-in. Trip at X/L=0.20, Run 010, α = 40-deg, Re_∞ = 7.3 × 10^6/ft

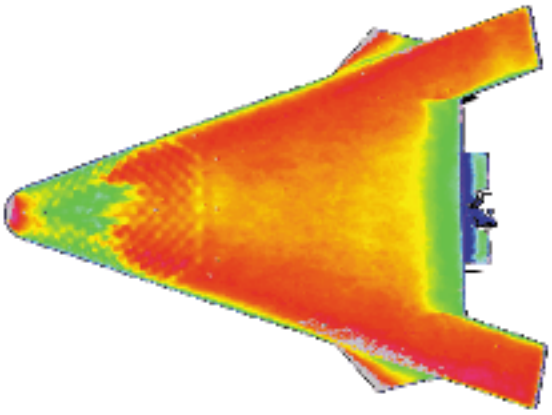

Figure A. 12: Extended Bowed Panel Model , Run 012, α = 40-deg, Re_∞ = 7.3 × 10^6/ft

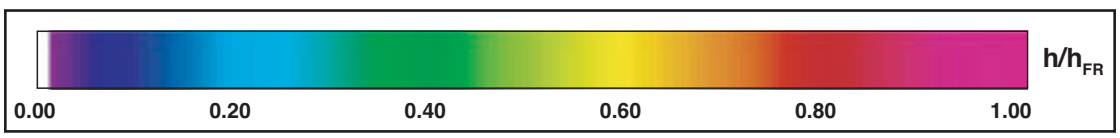

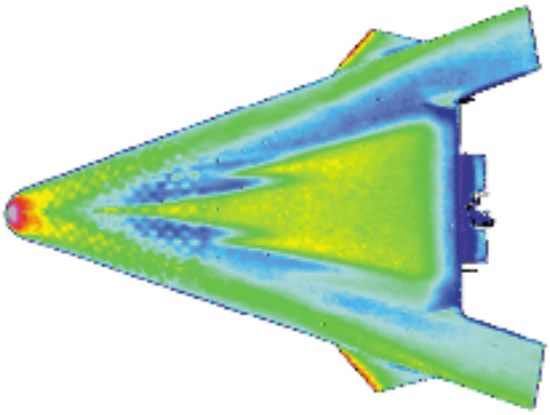

Figure A. 13: Extended Bowed Panel Model with 0.0065-in. Trip at X/L=0.20, Run 013, α = 40-deg, $Re_\infty = 3.0 \times 10^6$/ft

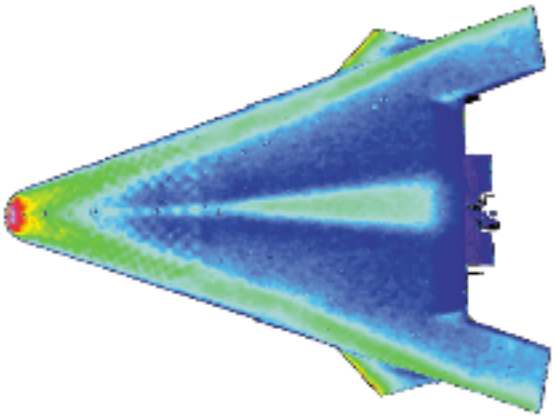

Figure A. 15: Extended Bowed Panel Model with 0.0065-in. Trip at X/L=0.20, Run 016, α = 40-deg, $Re_\infty = 1.1 \times 10^6$/ft

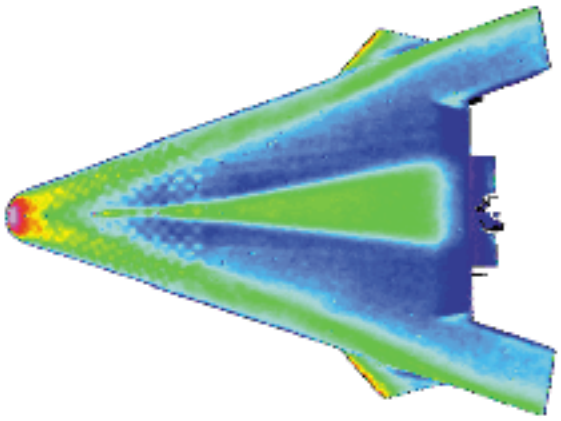

Figure A. 14: Extended Bowed Panel Model with 0.0065-in. Trip at X/L=0.20, Run 014, α = 40-deg, $Re_\infty = 2.2 \times 10^6$/ft

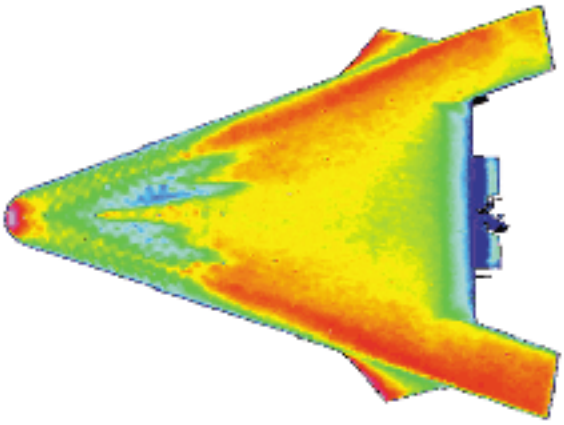

Figure A. 16: Extended Bowed Panel Model with 0.0065-in. Trip at X/L=0.20, Run 017, α = 40-deg, $Re_\infty = 4.2 \times 10^6$/ft

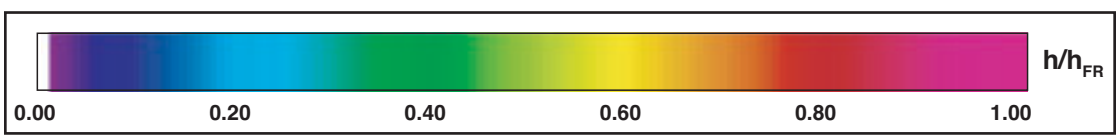

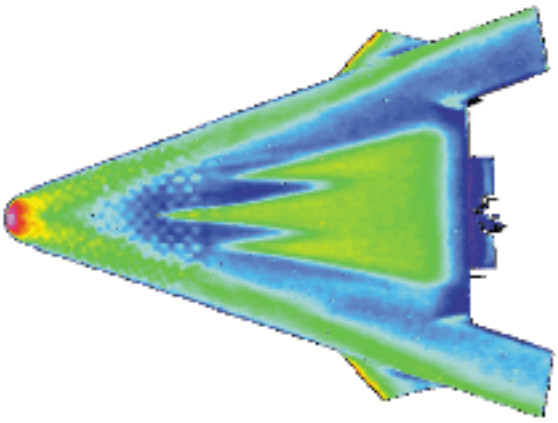

Figure A. 17: Extended Bowed Panel Model with 0.0065-in. Trip at X/L=0.32, Run 018, α = 40-deg, $Re_\infty = 3.0 \times 10^6$/ft

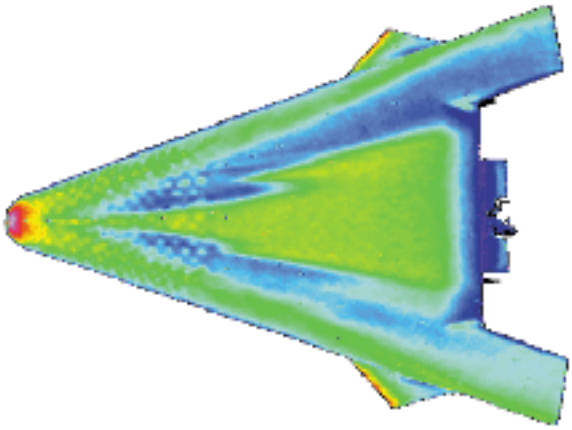

Figure A. 19: Extended Bowed Panel Model with 0.0065-in. Trip at X/L=0.10, Run 020, α = 40-deg, $Re_\infty = 3.0 \times 10^6$/ft

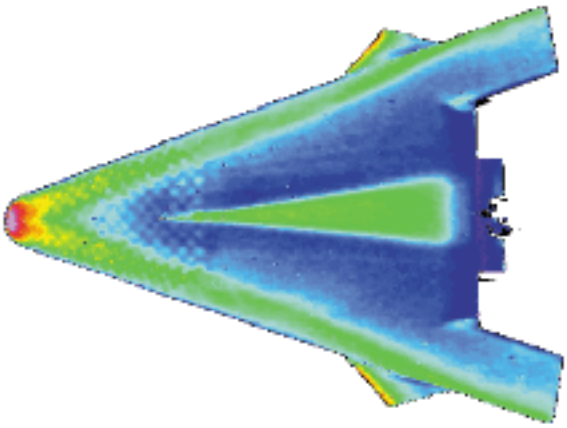

Figure A. 18: Extended Bowed Panel Model with 0.0065-in. Trip at X/L=0.32, Run 019, α = 40-deg, $Re_\infty = 2.2 \times 10^6$/ft

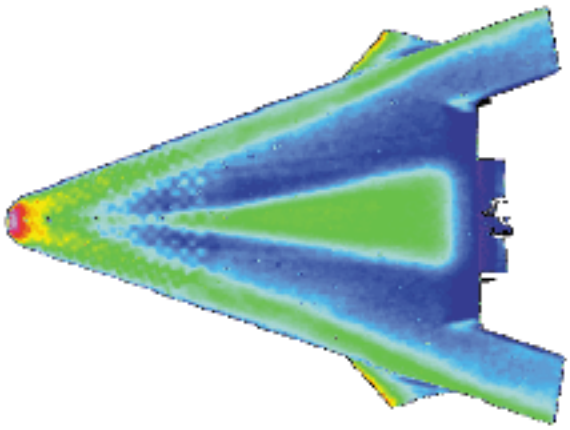

Figure A. 20: Extended Bowed Panel Model with 0.0065-in. Trip at X/L=0.10, Run 021, α = 40-deg, $Re_\infty = 2.2 \times 10^6$/ft

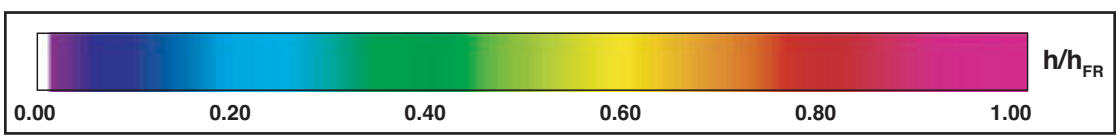

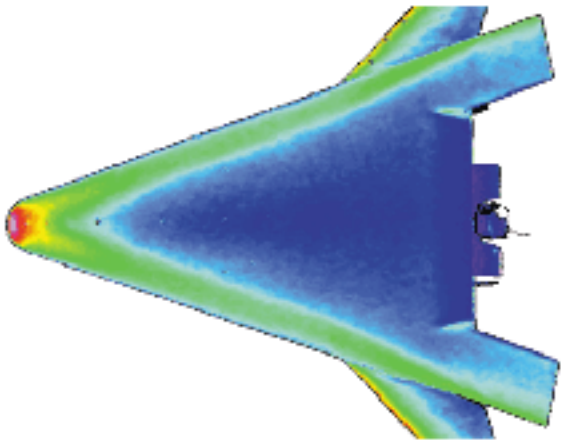

Figure A. 21: Smooth Model with 0.0025-in. Trip at X/L =0.20, Run 023, α = 40-deg, $Re_\infty = 2.2 \times 10^6$/ft

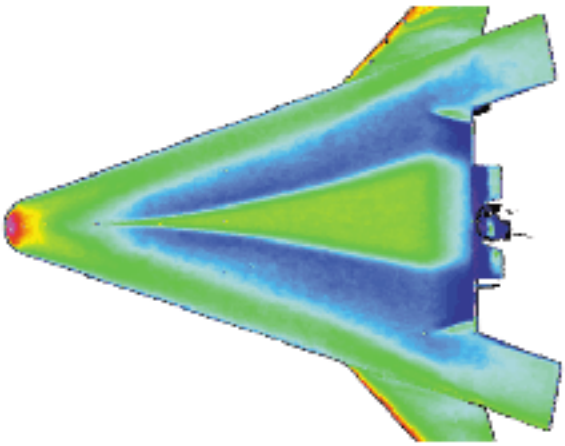

Figure A. 23: Smooth Model with 0.0025-in. Trip at X/L =0.20, Run 025, α = 40-deg, $Re_\infty = 4.2 \times 10^6$/ft

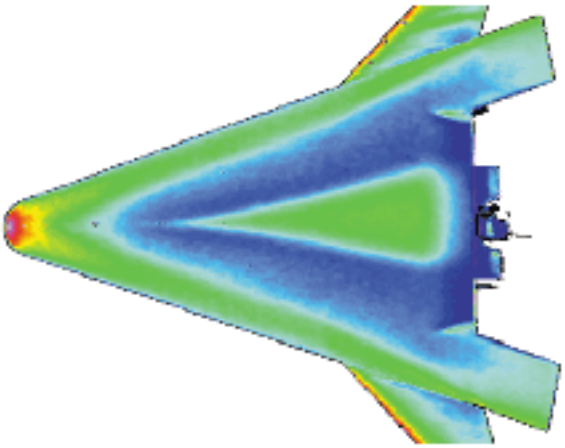

Figure A. 22: Smooth Model with 0.0025-in. Trip at X/L =0.20, Run 024, α = 40-deg, $Re_\infty = 3.0 \times 10^6$/ft

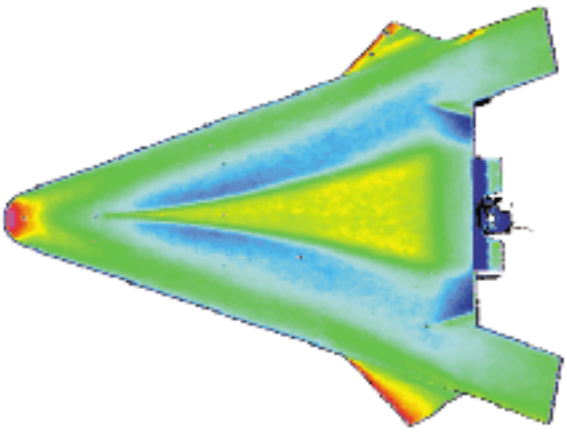

Figure A. 24: Smooth Model with 0.0025-in. Trip at X/L =0.20, Run 027, α = 40-deg, $Re_\infty = 5.8 \times 10^6$/ft

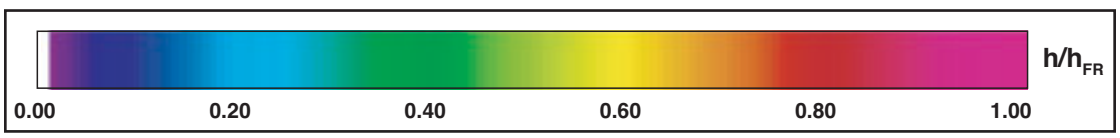

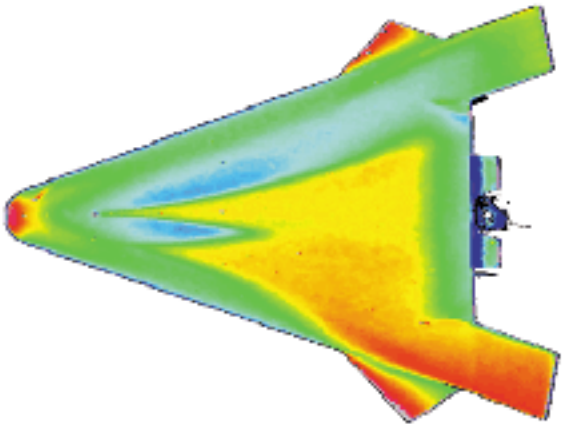

Figure A. 25: Smooth Model with 0.0025-in. Trip at X/L =0.20, Run 028, α = 40-deg, $Re_\infty = 7.3 \times 10^6$/ft

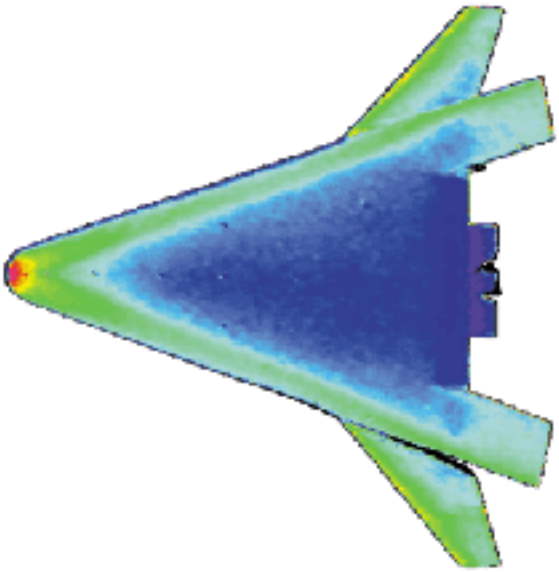

Figure A. 27: Smooth Model , Run 057, α = 40-deg, $Re_\infty = 3.0 \times 10^6$/ft

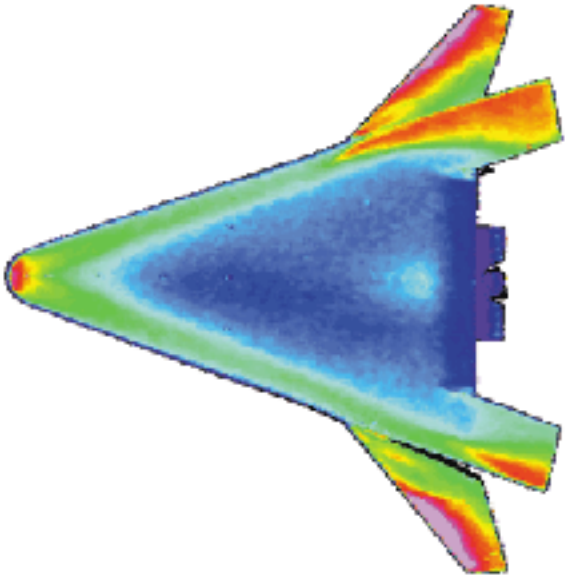

Figure A. 26: Smooth Model , Run 056, α = 40-deg, $Re_\infty = 4.2 \times 10^6$/ft

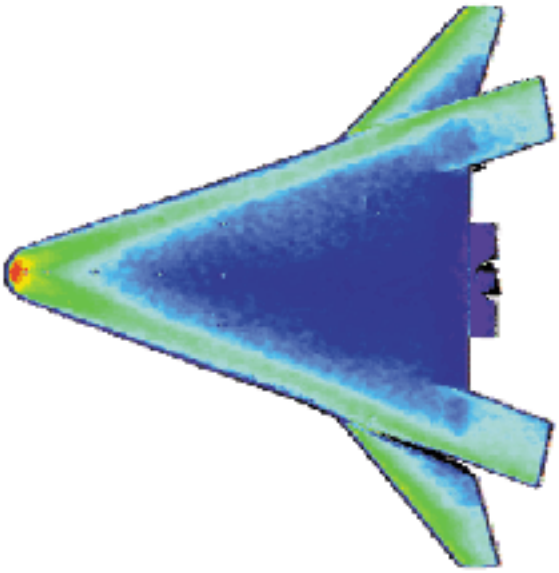

Figure A. 28: Smooth Model , Run 058, α = 40-deg, $Re_\infty = 2.2 \times 10^6$/ft

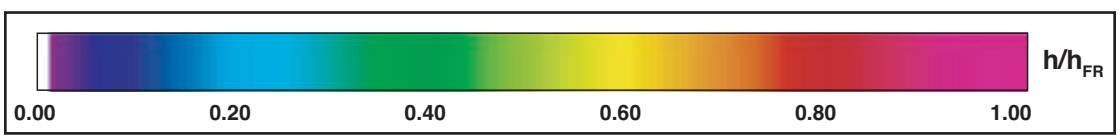

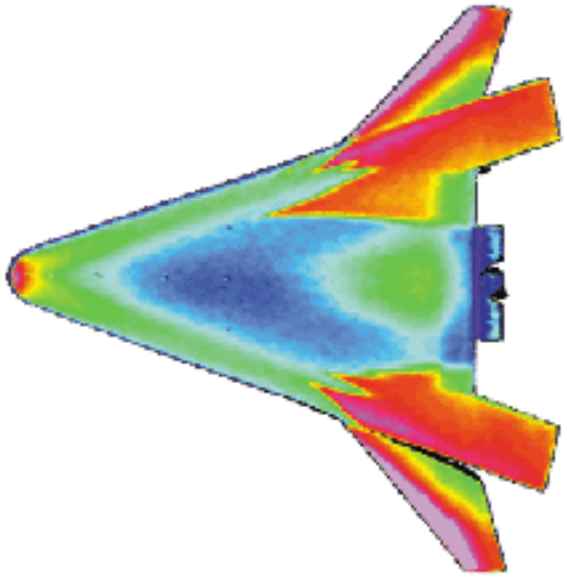

Figure A. 29: Smooth Model , Run 059, α = 40-deg, $Re_\infty = 5.1 \times 10^6$/ft

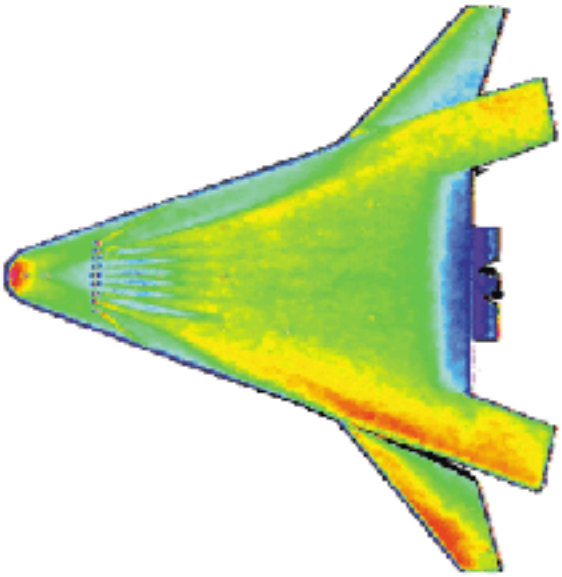

Figure A. 31: Smooth Model with 0.0065-in. Trip Array at X/L=0.20, Run 061, α = 40-deg, $Re_\infty = 3.0 \times 10^6$/ft

Figure A. 30: Smooth Model with 0.0065-in. Trip Array at X/L=0.20, Run 060, α = 40-deg, $Re_\infty = 2.2 \times 10^6$/ft

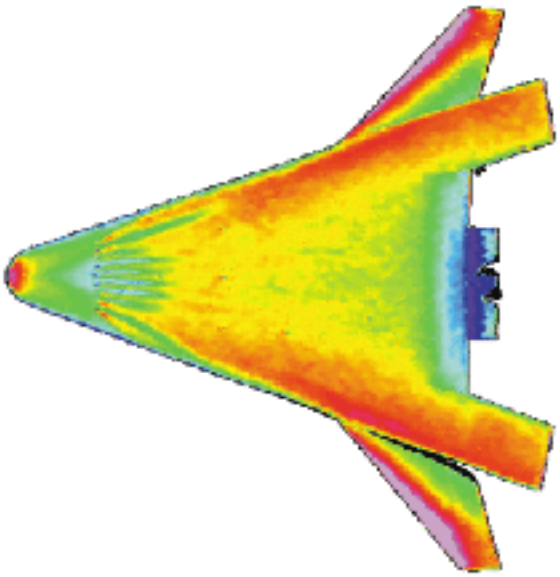

Figure A. 32: Smooth Model with 0.0065-in. Trip Array at X/L=0.20, Run 062, α = 40-deg, $Re_\infty = 4.2 \times 10^6$/ft

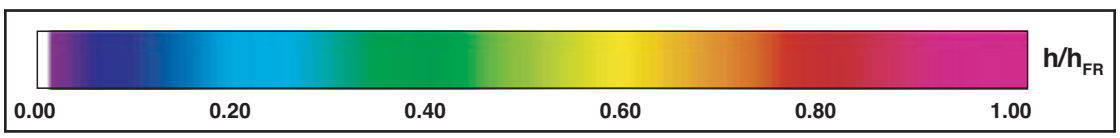

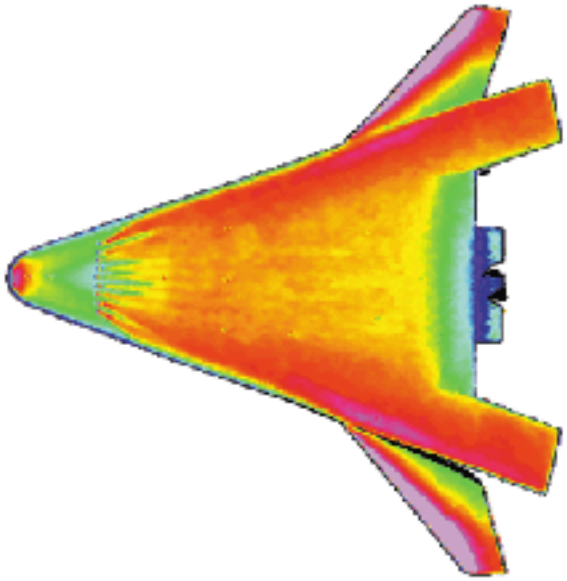

Figure A. 33: Smooth Model with 0.0065-in. Trip Array at X/L=0.20, Run 063, α = 40-deg, Re_∞ = 5.1 × 10^6/ft

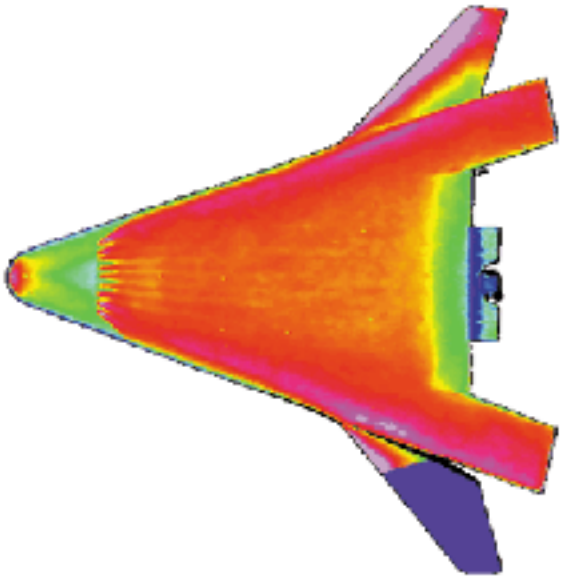

Figure A. 35: Smooth Model with 0.0065-in. Trip Array at X/L=0.20, Run 065, α = 40-deg, Re_∞ = 7.3 × 10^6/ft

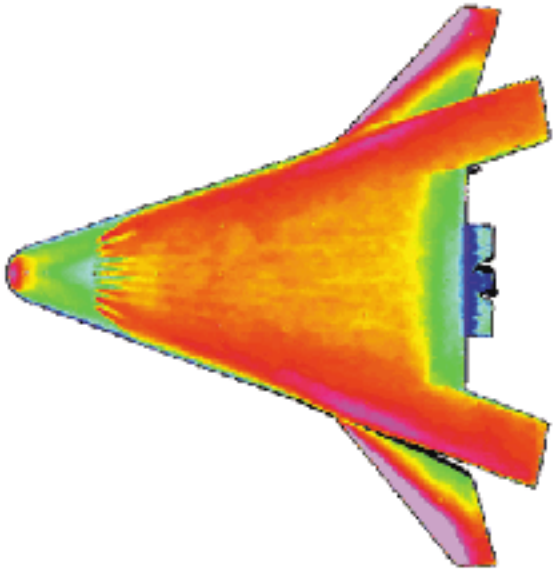

Figure A. 34: Smooth Model with 0.0065-in. Trip Array at X/L=0.20, Run 064, α = 40-deg, Re_∞ = 5.8 × 10^6/ft

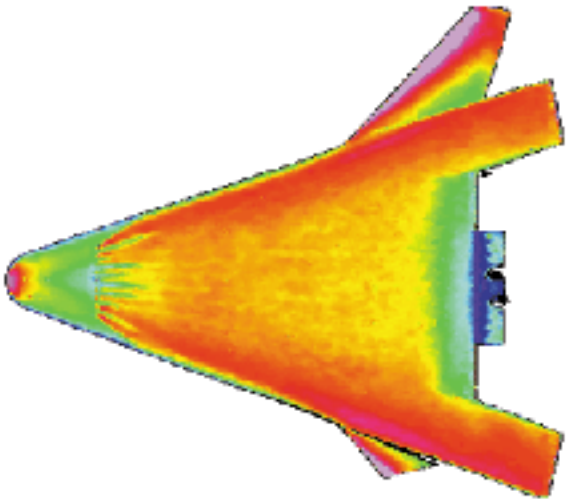

Figure A. 36: Smooth Model with 0.0065-in. Trip Array at X/L=0.20, Run 066, α = 40-deg, Re_∞ = 5.1 × 10^6/ft

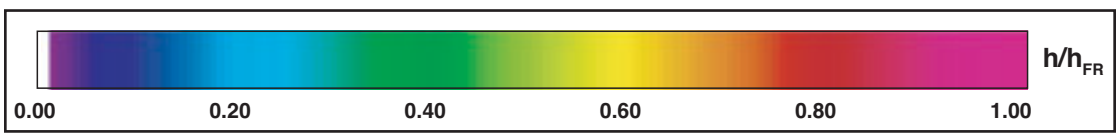

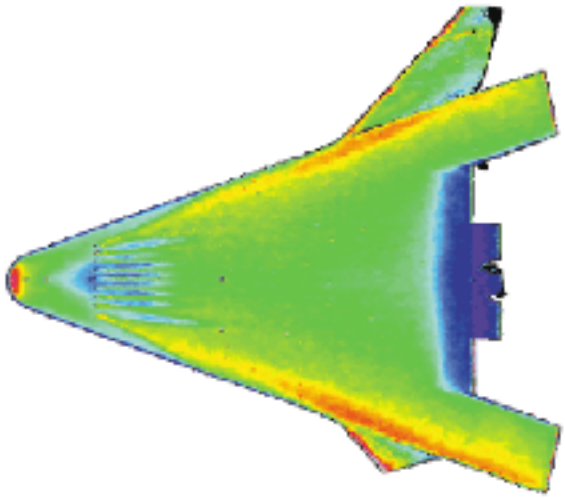

Figure A. 37: Smooth Model with 0.0065-in. Trip Array at X/L=0.20, Run 067, α =30-deg, $Re_\infty = 4.2 \times 10^6$/ft

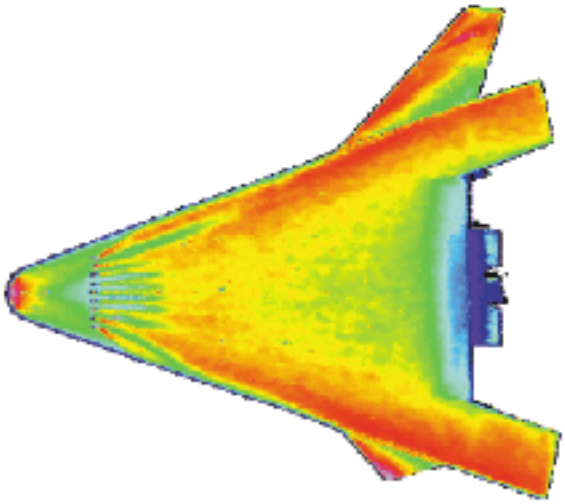

Figure A. 39: Smooth Model with 0.0065-in. Trip Array at X/L=0.20, Run 069, α = 40-deg, $Re_\infty = 4.2 \times 10^6$/ft

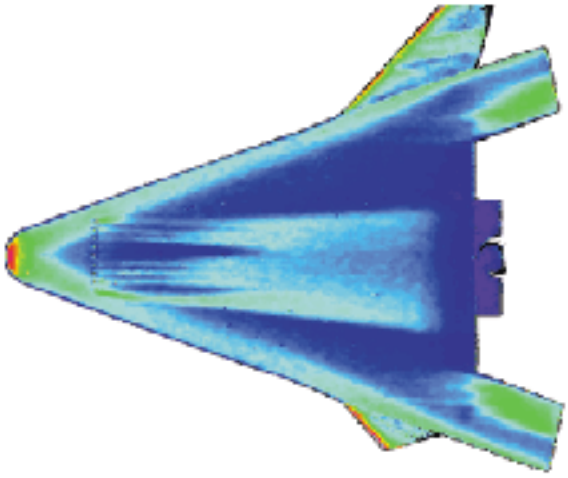

Figure A. 38: Smooth Model with 0.0065-in. Trip Array at X/L=0.20, Run 068, α =20-deg, $Re_\infty = 4.2 \times 10^6$/ft

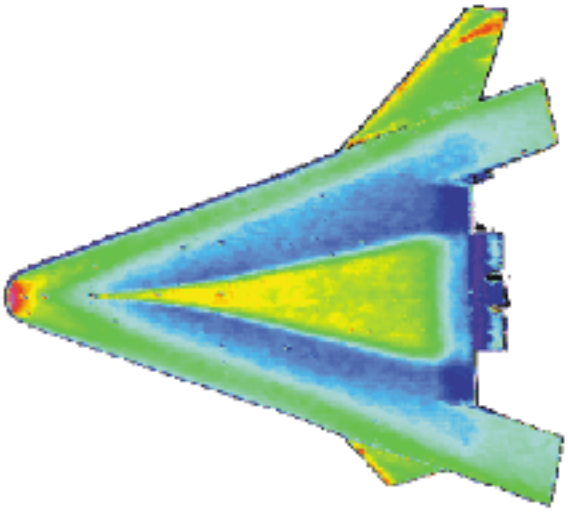

Figure A. 40: Smooth Model with 0.0065-in. Trip at X/L=0.20, Run 070, α = 40-deg, $Re_\infty = 4.2 \times 10^6$/ft

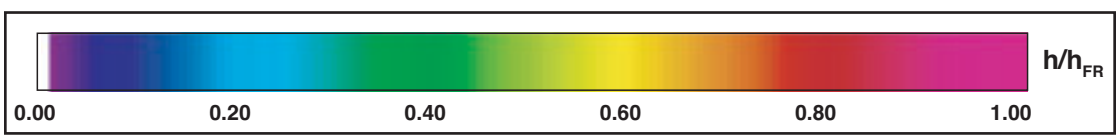

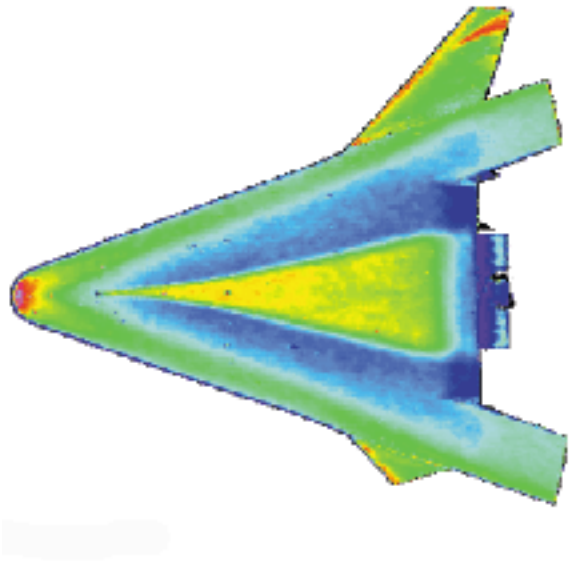

Figure A. 41: Smooth Model with 0.0035-in. Trip at X/L=0.20, Run 071, α = 40-deg, $Re_\infty = 4.2 \times 10^6$/ft

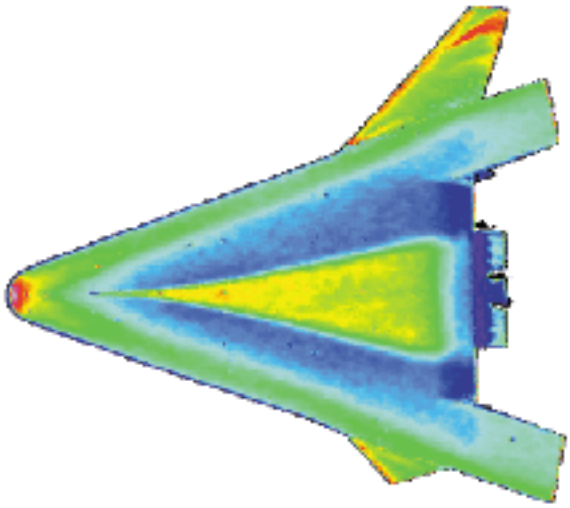

Figure A. 43: Smooth Model with 0.0035-in. Trip at X/L=0.20, Run 073, α = 40-deg, $Re_\infty = 4.2 \times 10^6$/ft

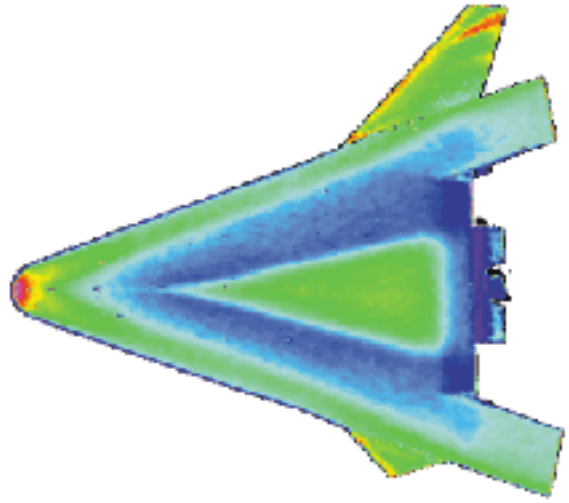

Figure A. 42: Smooth Model with 0.0025-in. Trip at X/L=0.20, Run 072, α = 40-deg, $Re_\infty = 4.2 \times 10^6$/ft

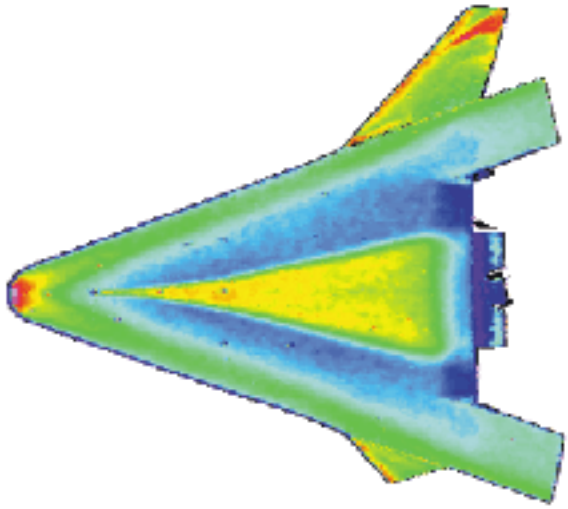

Figure A. 44: Smooth Model with 0.0050-in. Trip at X/L=0.20, Run 074, α = 40-deg, $Re_\infty = 4.2 \times 10^6$/ft

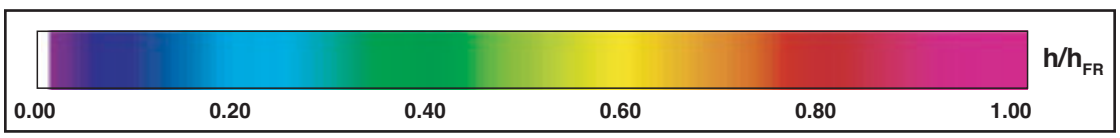

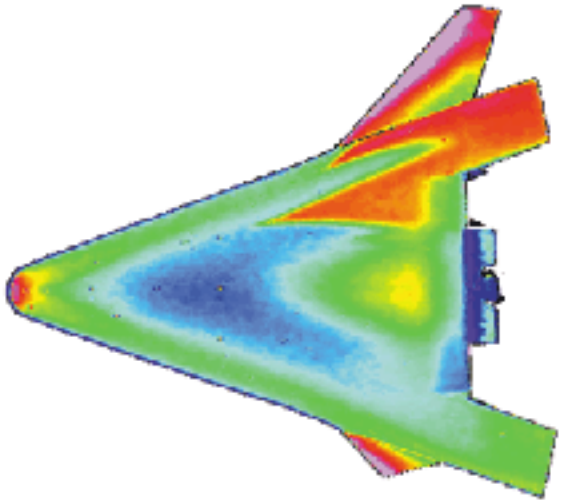

Figure A. 45: Smooth Model , Run 075, α = 40-deg, $Re_\infty = 5.8 \times 10^6$/ft

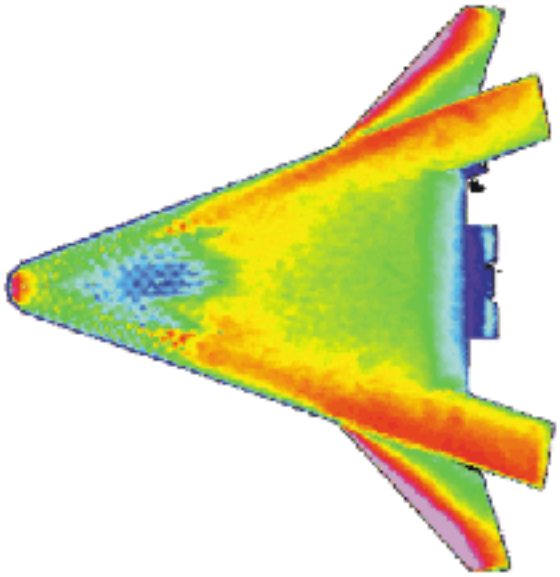

Figure A. 47: Extended Bowed Panel Model, Run 077, α = 40-deg, $Re_\infty = 4.2 \times 10^6$/ft

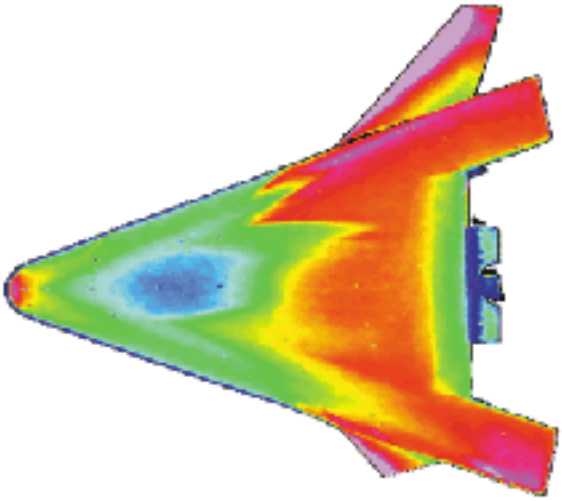

Figure A. 46: Smooth Model , Run 076, α = 40-deg, $Re_\infty = 7.3 \times 10^6$/ft

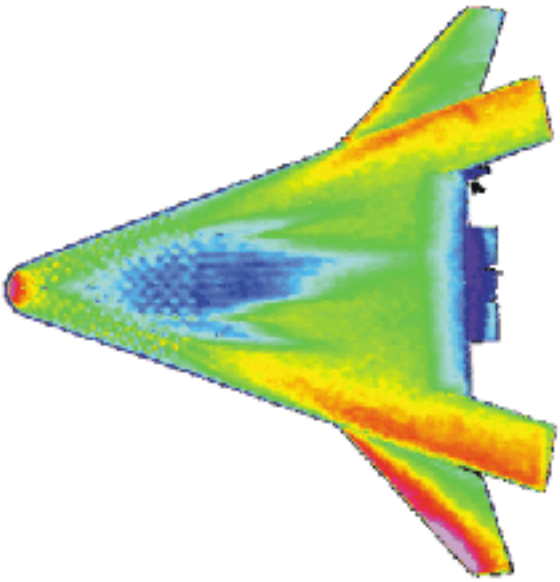

Figure A. 48: Extended Bowed Panel Model, Run 078, α = 40-deg, $Re_\infty = 3.0 \times 10^6$/ft

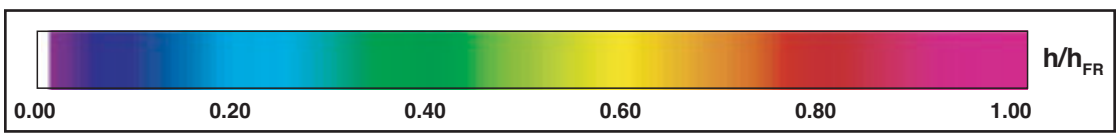

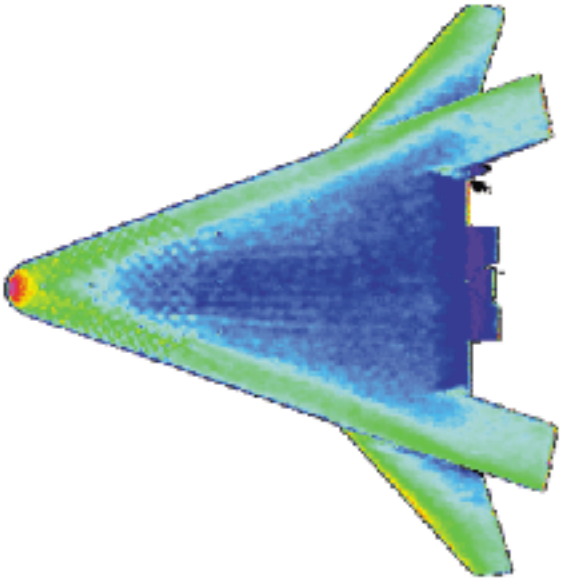

Figure A. 49: Extended Bowed Panel Model, Run 079, α = 40-deg, $Re_\infty = 2.2 \times 10^6$/ft

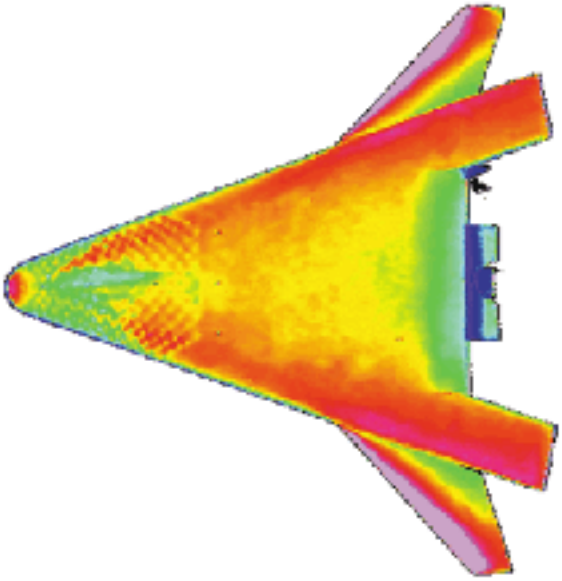

Figure A. 51: Extended Bowed Panel Model, Run 081, α = 40-deg, $Re_\infty = 5.8 \times 10^6$/ft

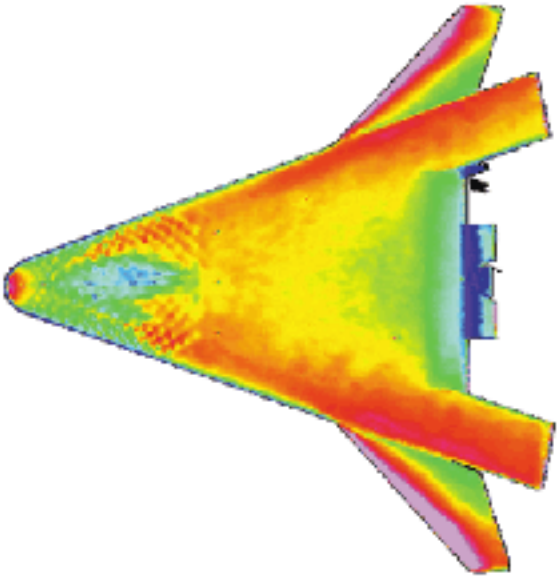

Figure A. 50: Extended Bowed Panel Model, Run 080, α = 40-deg, $Re_\infty = 5.1 \times 10^6$/ft

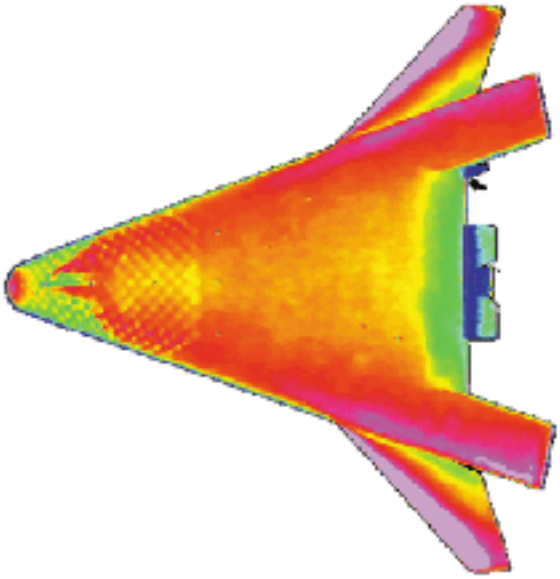

Figure A. 52: Extended Bowed Panel Model, Run 082, α = 40-deg, $Re_\infty = 7.3 \times 10^6$/ft

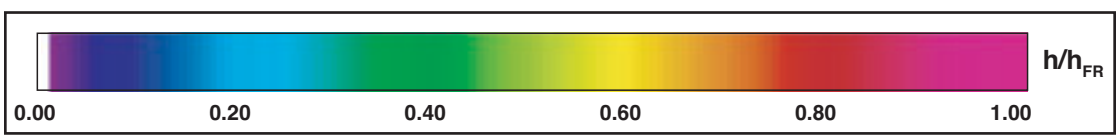

REPORT DOCUMENTATION PAGE

Form Approved
OMB No. 0704-0188

1. REPORT DATE *(DD-MM-YYYY)*	2. REPORT TYPE	3. DATES COVERED *(From - To)*
01- 06 - 2003	Technical Memorandum	

4. TITLE AND SUBTITLE

X-33 Rev-F Turbulent Aeroheating Results From Test 6817 in NASA Langley 20-Inch Mach 6 Air Tunnel and Comparisons With Computations

5a. CONTRACT NUMBER

5b. GRANT NUMBER

5c. PROGRAM ELEMENT NUMBER

6. AUTHOR(S)

Hollis, Brian R.; Horvath, Thomas J.; and Berry, Scott A.

5d. PROJECT NUMBER

5e. TASK NUMBER

5f. WORK UNIT NUMBER

721-28-00-05

7. PERFORMING ORGANIZATION NAME(S) AND ADDRESS(ES)

NASA Langley Research Center
Hampton, VA 23681-2199

8. PERFORMING ORGANIZATION REPORT NUMBER

L-18293

9. SPONSORING/MONITORING AGENCY NAME(S) AND ADDRESS(ES)

National Aeronautics and Space Administration
Washington, DC 20546-0001

10. SPONSOR/MONITOR'S ACRONYM(S)

NASA

11. SPONSOR/MONITOR'S REPORT NUMBER(S)

NASA/TM-2003-211962

12. DISTRIBUTION/AVAILABILITY STATEMENT

Unclassified - Unlimited
Subject Category 34
Availability: NASA CASI (301) 621-0390 Distribution: Standard

13. SUPPLEMENTARY NOTES

Hollis, Horvath and Berry: Langley Research Center
An electronic version can be found at http://techreports.larc.nasa.gov/ltrs/ or http://ntrs.nasa.gov

14. ABSTRACT

Measurements and predictions of the X-33 turbulent aeroheating environment have been performed at Mach 6, perfect-gas air conditions. The purpose of this investigation was to compare measured turbulent aeroheating levels on smooth models, models with discrete trips, and models with arrays of bowed panels (which simulate bowed thermal protections system tiles) with each other and with predictions from two Navier-Stokes codes, LAURA and GASP. The wind tunnel testing was conducted at free stream Reynolds numbers based on length of 1.8×10^6 to 6.1×10^6 on 0.0132 scale X-33 models at a = 40-deg. Turbulent flow was produced by the discrete trips and by the bowed panels at all but the lowest Reynolds number, but turbulent flow on the smooth model was produced only at the highest Reynolds number. Turbulent aeroheating levels on each of the three model types were measured using global phosphor thermography and were found to agree to within the estimated uncertainty (±15%) of the experiment. Computations were performed at the wind tunnel free stream conditions using both codes. Turbulent aeroheating levels predicted using the LAURA code were generally 5%-10% lower than those from GASP, although both sets of predictions fell within the experimental accuracy of the wind tunnel data.

15. SUBJECT TERMS

X-33; Aeroheating; Boundary-layer transition; Hypersonics

16. SECURITY CLASSIFICATION OF:			17. LIMITATION OF ABSTRACT	18. NUMBER OF PAGES	19a. NAME OF RESPONSIBLE PERSON
a. REPORT	b. ABSTRACT	c. THIS PAGE			STI Help Desk (email: help@sti.nasa.gov)
					19b. TELEPHONE NUMBER *(Include area code)*
U	U	U	UU	74	(301) 621-0390